Photometric characterization of the Earthshine Telescope

Henriette Schwarz

Lund Observatory
Lund University

2012-EXA68

Degree project of 60 higher education credits (for a degree of Master)
May 2012

Lund Observatory
Box 43
SE-221 00 Lund
Sweden

Photometric characterization of the Earthshine Telescope

Henriette Schwarz

Master Thesis
May 2012

Supervisors:
Torben Andersen (Lund University),
Peter Thejll (Danish Meteorological Institute),
Hans Gleisner (Danish Meteorological Institute)

Department of Astronomy and Theoretical Physics
Faculty of Science
Lund University

Contents

Summary

Uncertainties in determination of the Earth's albedo currently limit our understanding of climate and climate change. A new telescope has been designed and built in collaboration between Danish Meteorological Institute and Lund Observatory to study the ratio between the intensities of earthshine to moonlight. This ratio is proportional to the terrestrial albedo. The aim of the Earthshine Telescope is to acquire long-term albedo data with a precision of about 0.1%. In order to achieve this goal the precision of the intensity ratio must be of the same order of magnitude or less. Preferably the accuracy should be reduced to similar values.

The aim of this master thesis has been to photometrically characterize the Earthshine Telescope. I have set up an error budget for both the earthshine and moonlight intensities that is relevant for the operational mode of the telescope which is currently in use, the Co-add mode. In Co-add mode both the dark and the bright parts of the Moon are observed simultaneously in a long series of short exposures that are subsequently aligned and co-added. The stacking of many frames allows the signal-to-noise of the earthshine to build up without over-exposure of the bright side of the Moon.

The image reduction process has three different steps: Bias subtraction, flatfielding and removal of scattered light on the dark side of the Moon. The three steps have been analyzed separately in order to determine their individual contributions to the error on the intensities.

It is possible to reach the required level of precision in the intensity ratio of 0.1% at least for some lunar phases around $\pm 140^{\circ}$, close to New Moon. The main contributor to the error on the earthshine intensity is photon noise and the main contributor to the error on the moonlight intensity is the flatfield.

The accuracy in the intensity ratio is typically a few percent, although it should be noted that this is an upper limit. The dominant source of systematic uncertainty is the imperfect removal of scattered light.

* * *

Dansk Resume

Sommetider, når Månen er næsten ny, kan man se den del af Månen, der ikke er oplyst af Solen. Det svage lys fra denne mørke del af Månen kaldes jordskin, og er sollys, der er blevet reflekteret fra Jorden til Månen og tilbage igen. Forholdet imellem intensiteten af jordskinnet og måneskinnet er proportionalt med Jordens albedo - hvor stor en del af det indkomne

sollys, Jorden reflekterer bort. Jordens albedo er en vigtig brik i forståelsen af Jordens klima og især klima forandringer.

Dansk meteorologisk Institut og Lunds Observatorie har bygget et nyt teleskop, der er designet til at måle forholdet imellem intensiteten af jordskinnet og månelyset. Målet er, at teleskopet skal indsamle albedo data over en længere periode med en spredning på 0.1% eller mindre. Jeg har i denne afhandling opstillet fejlbudgetter for målingen af jordskinnets og måneskinnets intensitet, så at det bliver muligt at vurdere om teleskopet lever op til sit mål. Det er blandt andet gjort ved seperat at vurdere usikkerheder, der opstår i forbindelse med de forskellige trin af billede reduktionen: bias subtraktion og flatfielding samt fjernelse af spredt lys på den mørke del af Månen.

Teleskopet kan opnå den krævede maksimale spredning for nogle af Månens faser tæt ved Nymåne, når jordskinnet er kraftigst. Det største bidrag til spredningen på målte jorskins intensiteter kommer fra fotonstøj, hvorimod det er flatfielding som er dominerende for spredningen på måneskinnets intensiteter. Nøjagtigheden af intensitets målingerne er typisk på et par procent, hvilket skyldes at der er store systematiske usikkerheder i forbindelse med at fjerne det spredte lys.

Introduction

Astronomy and climate research are not ordinarily interlaced subjects, but in the case of determining changes in the Earth's albedo, the two subjects can benefit from each other. Uncertainties in determination of the Earth's albedo currently limit our understanding of climate and climate change. The terrestrial albedo can be determined from observations of the Moon, and such groundbased albedo measurements can be a valuable supplement to the direct albedo observations from satellites. A collaboration between Lund Observatory and Danish Meteorological Institute has built, and is currently testing, a telescope system designed to study the ratio of the earthshine to moonlight, and thus ultimately the Earth's albedo.

The aim of this master thesis is to photometrically characterize the Earthshine Telescope. I will estimate the typical errors we can expect on earthshine and moonlight intensities. An analysis of the different steps in the image reduction process will provide an understanding of the individual contributions to the error on the intensities, and thus provide information about the optimal use of the Earthshine Telescope.

* * *

The thesis is organized as follows: The three first chapters are descriptive and provide the necessary background information. The first chapter illuminates the importance of better albedo measurements for climatic research, and I explain how groundbased observations of the Moon can be used to determine the Earth's albedo. In chapter two I describe the telescope system, and the four different operational modes used for determining the relative intensities of the dark and bright sides of the Moon. Chapter three is an introduction to the concept of an error budget. I present the image reduction steps and the error equations.

Chapters four and five give an analysis of the two basic image reduction steps, bias subtraction and flatfielding. In chapter six I test a method for removing scattered light from the Moon images, and in chapter seven I compare various techniques of how to align Moon images precisely. Chapter eight is an error budget for one of the operational modes of the Earthshine Telescope. I employ the results from earlier chapters and estimate the errors on earthshine and moonlight intensities. In the last chapter I conclude on my results.

* * *

ACKNOWLEDGEMENTS
I would like to show my gratitude to my supervisors Peter Thejll, Torben Andersen and Hans Gleisner. Your support and guidance have enabled me to develop an understanding of the subject. I send my thanks to the entire earthshine team, both current and previous members, with a special thanks to Mette Owner-Petersen - your comments were much appreciated. I am thankful to the people who found time for me and my many questions, eventhough they were not my supervisors, nor teachers at my institute. Thank you, Preben Nørregård, Kalle Åstrøm and Claus Führer.
Finally, my gratitude goes to Lisbeth Jørgensen. You know why.

* * *

Enjoy reading!

Chapter 1

Earthbased Albedo Determination

Figure 1.1: **Left:** Da Vinci's sketch of a crescent Moon with earthshine [ca. 1510]. **Right**: Modern photograph of earthshine.

On a clear night, when the Moon is nearly new, the part of the Moon not bathed in sunlight, is seen to have a faint glow. The light reaching us from this darker part of the Moon is called ashenlight or earthshine. Leonardo da Vinci explained and drew the phenomenon nearly 500 years ago. The bright side of the Moon is sunlight reflected of the Moon's surface. The earthshine, on the other hand, is sunlight that has been reflected first by the Earth and then retroflected from the Moon.

The absorption of some of the light by Earth is the only difference between the light reaching an observer on Earth from the dark and the bright parts of the Moon. Therefore the terrestrial albedo can be determined from the ratio between the specific intensities of the earthshine and the moon-

light. This is done by observing two small patches of the Moon near the edges of the disc - one in the dark part and one in the bright part. It is assumed that two patches of Moon surface can be found with the same reflectivity.

$$A \propto \frac{I_{dark}}{I_{bright}}$$

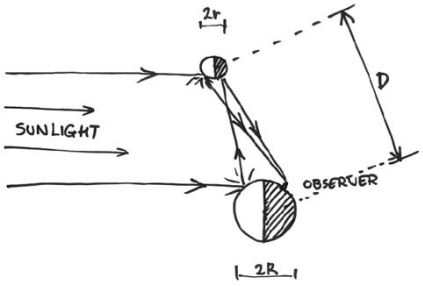

Figure 1.2: The geometry of earthshine. Earthshine is sunlight reflected from the day side of the Earth to the night side of the Moon and reflected from there down to the observer. The proportion of light from the dark side of the Moon to light from the bright side is proportional to the terrestrial albedo [Thejll and Gleisner, 2007] .

1.1 Albedo and Climate

The simplest way of describing the Earth's climate is with a global energy balance model. The Earth is considered to be a single point in space with a global mean effective temperature, T_{eff}, and this temperature is determined by the balance between the energy input and output.

The incoming energy is controlled by the solar constant and the terrestrial albedo. Electromagnetic radiation from the Sun (predominantly shortwave) reaches the Earth. The solar constant is the flux density of this solar radiation incident on a plane perpendicular to the rays at a distance of $1AU$ from the Sun (the average distance between the Earth and the Sun). In spite of the name it is not truly a constant but varies with about 0.1% during the 11-year solar cycle. During the last solar minimum period the albedo was measured to be $1360.8W\,m^{-2}$ [Kopp and Lean, 2011]. The atmoshpere, the clouds and the surface of the Earth reflect a fraction of the incident radiation back to space. This fraction is called the albedo, and its current value is about 0.3.

The other 70% of the incoming radiation is absorbed at the surface. Over time the heated surface emits the received energy as thermal radiation. Greenhouse gasses absorb a portion of the thermal radiation before reemitting it in all directions, so that part of the radiation contributes to heating the surface once more. The energy output of the Earth is thus determined both by the effective temperature and the transparency of the atmosphere to the outgoing thermal radiation.

To sum up the above, the global mean temperature is determined by only three parameters: The solar constant, the global albedo and the greenhouse effect. In order to make more advanced climate models and predict the climate of the future, it is crucial that these three parameters are well-known and understood.

1.1.1 A Simple Energy Balance Model of the Earth

The Earth receives energy in the form of electromagnetic radiation from the Sun on an area of Earth's projected disc on the sky. Per unit time, the incoming energy is

$$E_{in} = S\pi R_e^2(1-A), \tag{1.1}$$

where S is the solar constant (adjusted for the actual Earth-Sun distance), R_e is the Earth's radius and A is the planetary albedo. The paranthesis $(1-A)$ is the amount of the incident light absorbed by the Earth ($\approx 70\%$). Over time, this energy is reemitted as infrared radiation from the full surface-area of the Earth.

$$E_{out} = 4\pi R_e^2 \sigma T_{eff}^4, \tag{1.2}$$

where σ is the Stefan-Boltzmann constant and T_{eff} is the effective temperature of the Earth. The atmosphere is largely transparent to the longwave thermal radiation, but the presence of greenhouse gasses in the atmosphere causes the surface temperature, T_s, to be higher than the effective temperature. The temperature increment ΔT is known as the greenhouse increment, $T_s = T_{eff} + \Delta T$. Expressing equation (1.2) in terms of the surface temperature and the normalized greenhouse effect $g = \Delta T / T_s$ it becomes

$$E_{out} = 4\pi R_e^2 \sigma (1-g) T_s^4. \tag{1.3}$$

Assuming radiative equilibrium ($E_{in} = E_{out}$), we have [Qiu et al., 2003]

$$T_s^4 = \frac{S}{4\sigma(1-g)}(1-A). \tag{1.4}$$

This is the mathematical way of stating the conclusion from section 1.1 that the Earth's temperature is controlled by the solar constant, the planetary albedo and the greenhouse effect. Global warming can be a result of an increase in solar irradiance or greenhouse forcing, a decrease in albedo or a combination of the three. The same applies to global cooling, only opposite.

In the absence of feedbacks, the Earth's surface temperature would increase by roughly $1.5K$ for a decrease in albedo by 0.01. The science goal of the Earthshine Telescope is obtaining long-term albedo data with 0.1% precision. This corresponds to a temperature change of $0.045K$.

1.1.2 Albedo

The terrestrial albedo is a complex quantity. Our planet doesn't simply have one colour that reflects a certain amount of the incoming light. The oceans are darker than the continents, deserts are brighter than vegetation and snow and ice brighter still. The cloud-coverage is an important factor

since clouds are extremely efficient reflectors. All these components contribute to the global albedo and changes in their distribution will affect the albedo.

To illustrate the complexity of albedo changes, imagine desertification of a large rain forest. The desert sand is brighter than the trees, so the surface albedo increases, and we expect the surface temperature to cool. However, the lack of trees causes additional changes. The trees used to absorb large quantities of carbon dioxide that will now stay in the atmosphere strenghtening the greenhouse effect, warming the planet. The presence of trees also influences the cloud-formation of an area. Trees release hydrocarbons, a key-ingredient to formation of aerosols and by extension clouds [Paulot et al., 2009]. Desertification may therefore cause a decrease in planetary albedo due to less clouds and aerosols.

In the climate system there are multiple feedback mechanisms. Positive feedbacks enhance a perturbation, possibly leading to a runaway process, and negative feedbacks oppose a perturbation, restoring the balance. The most well-known feedback involving albedo is perhaps the ice-albedo feedback. If the global surface temperature on Earth were to decrease, this would lead to an increase in snow- and ice-coverage. Snow and ice have a high albedo, and additional areas covered in snow would cause an increase in surface albedo (probably also in planetary albedo, but this depends on other factors like cloud-coverage). The higher albedo will mean less incoming energy and a further decrease in temperature. This is an example of a positive feedback where the perturbation is reinforced. Right now, as a result of global warming, we can see this process in reverse. The higher temperatures melt snow and ice, so that the surface albedo decreases, potentially rising the temperature further. However, the exact relationship between surface albedo and planetary albedo is not fully understood (Chen and Ohring [1985] present a simple relationship for the case of clear-sky planetary albedo), and it is unclear how important such run-away processes are.

The albedo is sensitive to events like large vulcanic eruptions. Vulcanoes eject water vapour (H_2O), carbon dioxide (CO_2), sulfur dioxide (SO_2), hydrogen chloride (HCl), hydrogen fluoride (HF) and ash. If the erruption is big, these compounds will reach into the stratosphere at heights of $16 - 32km$. The sulfur dioxide is converted to sulfuric acid (H_2SO_4), and the acid condenses to form sulfate aerosols. These droplets are good reflectors themselves and they encourage cloud formation. The result is an increase in albedo, and the lower atmoshphere becomes colder. When Pinatubo in the Phillipines errupted in 1991, nearly 20 million tons of sulfur dioxide were injected to the stratosphere, and the global surface temperature dropped with about $0.5°C$ from 1991 to 1993 [Newhall et al., 1997]. It is worth noting that the presence of sulfate aerosols in the stratosphere actually heats the stratosphere itself, since they absorb heat radiated from the surface.

1.1.3 Clouds

Clouds generally have a very high albedo, and a cloud is thus likely to have a higher albedo than any surface it may cover. Therefore the planetary

albedo (the albedo as seen from outside of the atmoshphere) will be higher on a cloudy planet than on an identical planet with clear skies, and we must conclude that clouds have a cooling effect. This is a negative forcing of the Earth's climate called the cloud albedo forcing. On the other hand, clouds consist of water vapour, which is the predominant greenhouse gas in the atmoshpere, so they absorb infrared radiation emitted by the surface and radiate a portion of it back downward, warming the planet. This is a positive forcing of the Earth's climate called the cloud greenhouse forcing. Whether a given cloud will cool or warm the surface depends on the altitude, the structure and size of the cloud.

The basic different cloud types are illustrated in figure 1.3. In broad outline we can divide the different cloud types into high clouds, low clouds and deep convective clouds.

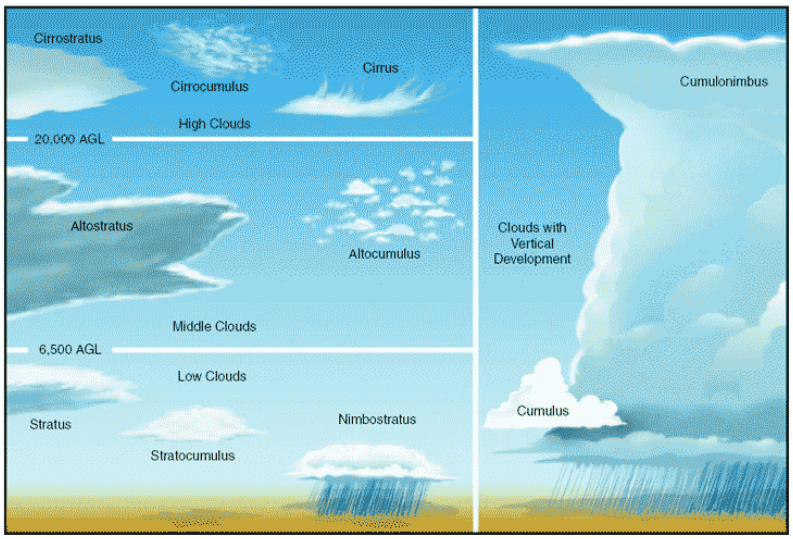

Figure 1.3: Basic cloud types. High clouds generally have a warming effect whereas low clouds generally have a cooling effect [Free Online Private Pilot Ground School].

High clouds, such as the thin feathery cirrus clouds, have a net warming effect. They are transparent to shortwave radiation from the Sun just like clear air, but their water vapour readily absorbs longwave radiation from the Earth. The absorbed radiation is reemitted in all directions. Because cirrus clouds are found at high altitudes, they are cold, and the energy radiated to outer space is lower than it would be without the cloud. The energy radiated back towards Earth from the cloud adds to the shortwave radiation from the Sun and the longwave radiation from the surrounding air, causing a warming of the atmosphere and surface.

Low clouds, such as the thick stratocumulus clouds, have a net cooling effect. Low clouds are generally much thicker than high clouds, and they are therefore less transparent to the incoming shortwave radiation. They have a high albedo. Stratocumulus clouds will of course also absorb and reemit infrared radiation, but their greenhouse forcing remains low. At the

low altitudes the clouds have nearly the same temperature as the surface, and therefore they radiate into space at nearly the same intensity as the surface. The downward radiation from the cloud will still have a warming effect, but the negative forcing from the high albedo predominates.

Deep convective clouds, such as the enormous cumulonimbus clouds, have a neutral effect. A cumulonimbus cloud is a towering vertical cloud with a base near the Earth's surface and a top reaching an altitude of more than $10km$. Since the top of the cloud is at a high altitude, it is cold, and the corresponding energy radiated to space is lower than would be the case without the presence of the cloud. The cloud greenhouse forcing is large. However, these clouds are both thick and dense, and therefore have a large cloud albedo forcing as well. The positive and negative forcings balance each other, leaving the cumulonimbus clouds neutral.

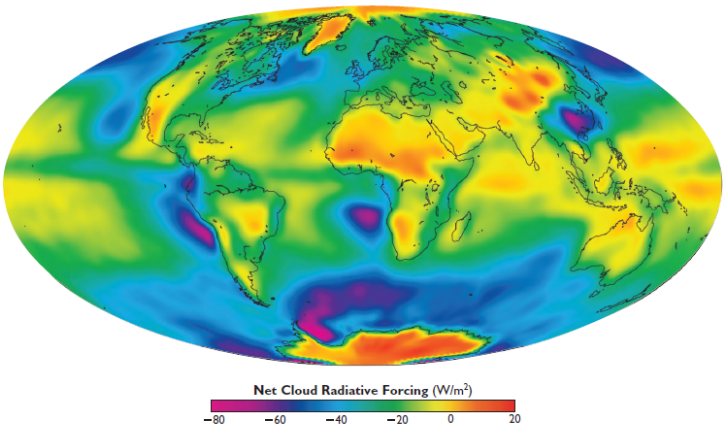

Figure 1.4: Annual mean net cloud radiative forcing for March 2000 through February 2001. Data from the CERES instrument on the Terra satellite. The negative forcing is predominant and hence clouds have a net cooling effect on the Earth [King et al., 2007].

The net cloud forcing from all the clouds on Earth is the result of two opposing effects. The positive forcing from the greenhouse effect of the clouds that tends to warm the Earth, and the negative forcing from the high albedo of the clouds that tends to cool the Earth. Figure 1.4 shows the annual mean net cloud forcing for March 2000 through February 2001. A few areas have net positive forcing but the negative forcing is clearly predominant over the course of the year. This is a general result: Clouds have a net cooling effect on the Earth [King et al., 2007].

An increase in temperature, such as the current global warming, causes more evaporation and the warmer air can hold more water vapour. This makes additional cloud formation likely, but the nature of any possible extra clouds is unknown. Will global warming mean an increase in cooling stratocumulus clouds, so that the climate system will stabilize itself? Or will we see an increase in the warming cirrus clouds instead? The re-

search is inconclusive so far, but there are indications that the total cloud frequency has been unchanged, whereas the high cloud frequency is increasing slightly [King et al., 2007]. Long-term global albedo measurements, collected in the future with a worldwide net of Earthshine Telescopes, could be compared with satellite data of cloud-coverage to investigate this missing link in our understanding of the climate system. It is also unknown how the radiative properties of clouds may change with temperature. The sizes of the cloud droplets directly influence the interaction with radiation, and it is reasonable to assume that these depend on both the composition of the atmosphere and the temperature.

1.2 Albedo Measurements

Of the three climate parameters the solar constant, the global albedo and the greenhouse effect, the albedo has received the least attention. In this section I describe the previous and current efforts to determine the global albedo. To date, there is no accurate, continuous, long-term albedo dataset available.

1.2.1 Historical Measurements

Perhaps the first to suggest a connection between earthshine and climate was Alexander von Humboldt (1769-1859). In a footnote in his work *Cosmos, a Sketch of a Physical Description of the Universe* [1852] he wrote:

> "It is not therefore impossible, notwithstanding the surprise which such a result may excite on first view, that one day meteorologists will derive valuable ideas as to the mean state of the diaphanity of our atmosphere in the hemispheres which successively contribute to the production of the ashy light."

Although sporadic earthshine measurements were recorded around the time of Humboldt (eg. selenograph Julius Schmidt (1825-1884) [Ashbrook, 1984]), it would be another fifty years before an attempt was made to determine the terrestrial albedo from earthshine observations.

Frank Very (1852-1927) determined Earth's albedo from visual photometric measurements of the earthshine and moonlight [1913], and from spectroscopic photography [1915]. Very realized that the earthshine measurements were in fact earthshine plus sky-background, and he therefore subtracted a measurement of the skylight outside the Moon's dark limb from the earthshine intensities. In both papers, Very found the albedo to have a value higher than 0.8, which we know today is much too high. Very noted in the summary of his 1915 paper that such a high albedo would mean the *"blanketing (...) due to aqueous vapor in the Earth's atmosphere"* must be much stronger than previously anticipated.

There are several reasons why Very arrived at a too high albedo. Russell [1916] (1877-1957) discussed some of these in a paper. First of all, one has to remember that there are many different definitions of albedo, and one must therefore state the albedo-type along with the result. It is unclear what kind of albedo Very himself used, but it was obviously not

the Bond albedo, which is perhaps the most common type of albedo in astronomy. Russell computed the Bond albedo from Very's observations (also using a different, much lower and more correct Moon albedo) and found $A_{\mathrm{E}} = 0.49$. This is still too high, but the phase functions and the geometric albedos were not known nor understood at the time, and Russell's albedo is similar to later values.

Very also, correctly, concluded from his spectroscopic observations that earthshine is more blue than moonlight. Today, spectroscopic observations of the earthshine is used to determine and understand the signatures of life in the spectrum of the Earth [Arnold, 2008, Briot, 2010, Montañés-Rodríguez and Pallé, 2010]. There exists several such signatures eg. the vegetation red edge, seasonal variations and chemical disequilibrium of the atmosphere. The aim of these investigations is to pave the way for interpreting, possibly detecting life in, future spectra from unresolved extrasolar planet images.

In 1924 Ernst Öpik (1893-1985) determined Earth's albedo from five photographic plates of the Earthshine. He found the value $A_{\mathrm{E}} = 0.63$ [1924]. The earthshine observations were all done very close to the New Moon, and there were no recordings of the moonlight intensity from the same nights. Instead Öpik compared the eartshine to Full Moon data. Öpik recognized the importance and difficulty of removing scattered light [1924]:

> "The chief difficulty in photographic measures of the earthshine is the great intensity of the background of the sky near the Moon and its variation with the distance from the bright limb."

In fact, Öpik discussed the distribution of brightness in the illuminated background near the Moon in some detail, and he proposed a solution to remove the scattered light from each individual plate. Removing scattered light is still one of the major challenges for accurate albedo measurements today. I have described in chapter 6, how we deal with this issue.

André-Louis Danjon (1890-1967) recorded earthshine measurements in the period from 1925 until the 1950s. Danjon invented a "cats-eye" photometer, a telescope with a prism that splits the image of the Moon into a double image. He made use of a diaphragm to adjust the brightness of one Moon image so that the bright side of the Moon in the dimmed image had the same apparent brightness as the dark side on the unadjusted image. Thus the diaphragm adjustment could be used to quantify the brightness of the Earthshine. The Danjon photometer has been used by several later astronomers. Figure 1.5 is a diagram of the Danjon photometer depicted by Bakos [1964].

Danjon [1954] made more than 200 measurements of the earthshine and converted them to an albedo of 0.4 with an estimated uncertainty of 5%. With the technology of that time, it was only possible to observe in the visible wavelengths, and Danjon had a large systematic error due to an incorrect lunar reflectivity. Unknown at the time, the Moon's reflectivity changes with the Sun-Earth-Moon alignment. Danjon found no long-term trend, but the daily mean values varied quite a bit. This could be due

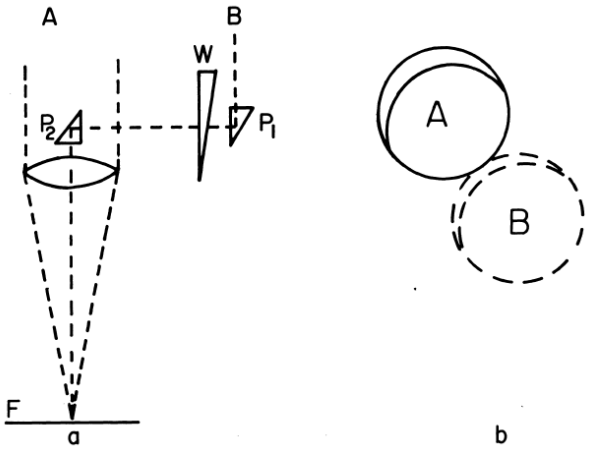

Figure 1.5: Diagram of Danjon-type photometer [Bakos, 1964].

to a combination of daily changes in cloud cover, changes in the Sun-Earth-Moon alignment and that the area of the Earth contributing to the earthshine changes from night to night.

Even though the Earth-area covered does indeed change from one night to the next, there will always be a geographical bias whenever you only make use of a single telescope located at one place on the Earth. In Danjon's case, his telescope was situated in France, and he therefore saw the earthshine reflected from the eastern hemisphere which is dominated by the landmasses of Asia. Since this part of the world has a higher than average fraction of land compared to ocean, he would tend to get a higher albedo than the global one.

Danjon's method was based on relative photometry. He compared the bright and dark sides of the Moon simultaneously. This is still the case in groundbased albedo determinations today. The relative approach has the advantage that fast atmospheric variations and instrumental effects are eliminated.

Dubois, another French astronomer, continued the work of Danjon with a similar photometric setup from about 1940 to 1960. He saw the same kind of daily variations as Danjon, but also found a considerable annual variability. His own speculations were that the annual variations were due to solar activity [1947]. Perhaps seasonal changes in snow- and cloud-coverage as well as vegetation may be a more reasonable explanation.

Gustav Bakos (1918-1991) was the first to collect earthshine measurements from a network of telescopes [1964]. He had access to six Danjon-type photometers (see figure 1.5) located on four different continents. Bakos' goal was to correlate albedo fluctuations with cloud cover information. Unfortunately no relation was found due to insufficient weather data. Bakos determined the yearly mean albedo value from 219 observations in 1958 to be $A_{\mathrm{E}} = 0.41$. Although Bakos did not have a geographical

bias, he still had the same issues as Danjon and Dubois when it came to the Moon's reflectivity and its variations.

After the time of Danjon and Dubois, the interest for earthshine seems to have dwindled. Additional observations of earthshine were made by Franklin [1967], Kennedy [1969] and Huffman et al. [1990].

1.2.2 Satellite Measurements of Albedo

The albedo can be determined from satellite measurements of the top-of-the-atmosphere (TOA) shortwave radiation. Geostationary satellites provide wide coverage and good temporal resolution, whereas satellites in polar orbits provide uniform coverage of the planet.

The satellites measure the TOA shortwave radiation for a particular spot on Earth, for a particular solar zenith angle, as seen from a particular satellite elevation and azimuth. Complex reflectance models are then used to convert this to a total outgoing shortwave flux. This includes the use of bi-directional reflectance distribution functions (BRDF) that correct for viewing and illumination angle effects. Further modelling is applied to combine measurements from several satellites to a global albedo.

The Earth Radiation Budget Experiment (ERBE) [Barkstrom, 1984] issued monthly mean albedos from the mid eighties to 1990, and its successor the Clouds and the Earth's Radiant Energy System (CERES) [Smith et al., 2004] continued this work from 2000. There are some time-gaps in the data. The instruments for these two projects have been placed on a total of five different satellites, all in semi-polar low-earth orbits. From low-earth orbits it is only possible to view a small fraction of the Earth's surface at once, but global coverage can be achieved by combining the data. This is difficult in practice, because the albedo must be derived from different instruments with different orbits, resolutions and sampling modes.

The Geostationary Earth Radiation Budget experiment (GERB) [Harries et al., 2005] has been in operation since December 2002 flying aboard the Meteosat Second Generation (MSG) satellites. This is a series of four low-earth orbit geostationary satellites with a minimum of two operating simultaneously for wider coverage (Europe, Africa, Middle East, South America). GERB is expected to continue till 2020, and the instruments are calibrated to a 1% accuracy in shortwave radiation [Mossavati et al., 1998].

The International Satellite Cloud Climatology Project (ISCCP) [Zhang et al., 2004] combines the TOA radiative fluxes from two polar orbiting and five geostationary satellites. Again, the combination of several satellites gives global coverage, but it has been argued that ISCCP data may not be appropriate for studying long-term global trends. Evan, Heidinger, and Vimont [2007] contended how trends can be a result of the geometry of the satellite system rather than true physical trends.

The optimal satellite albedo experiment would observe the whole sunlit Earth at once. NASA's Deep Space Climate Observatory (DSCVR - formerly known as Triana) was built for this purpose, but it has never been launched as a result of funding issues. DSCVR was supposed to be positioned in Earth's L1 Langrangian point, at a distance of 1.5 million kilometers from Earth. This position would allow a continuous view of

the sunlit Earth, getting close to directly observing a global albedo. Of course for a true global albedo, all angles need to be covered as well.

Satellite observations of the TOA shortwave radiation are irreplaceable as the most direct way to measure albedo. But it is complicated to combine the separate low-earth orbit data to a global albedo, and it is even more complicated to combine different projects into a long-term albedo dataset. Another obstacle is the difficulty in testing if the instruments lose their calibration over time.

Groundbased albedo derived from earthshine measurements can supplement the satellite data. The earthshine telescopes are inexpensive, and cover large regions of the Earth instantaneously. Furthermore, the groundbased telescopes are easy to repair and recalibrate compared to satellites, so that it is possible to obtain continuous long-term datasets. Both satellite and groundbased albedo determinations depend on assumptions and models. Intercomparisons between the two could be used for constraining the assumptions and test calibration stability of satellites.

1.2.3 Big Bear Solar Observatory

The Big Bear Solar Observatory (BBSO) has observed earthshine for just over a decade. The project has three earthshine telescopes. One located in Big Bear Valley in California, one located on Tenerife and finally one at the Crimea Observatory in Ukraine [Goode et al., 2010].

The BBSO group has modernized Danjon's technique for obtaining albedo data from Moon observations. First an image of the Moon is obtained with a short exposure time (tens of milliseconds) to avoid overexposure of the CCD. Generally the earthshine will be completely invisible in this bright side (BS) image. Then a blocking filter is inserted just before the prime focus in such a way that the BS is completely covered, permitting long exposures (60-150 seconds) of the dark side (DS). The intensity is measured in fiducial patches covering about 100 pixels each in both the BS image (moonlight) and the DS image (earthshine). Details of the BBSO observations and data reduction can be found in Qiu et al. [2003].

The ratio of the intensities of earthshine to moonlight is inverted to determine the albedo. This requires knowledge of the geometry of the Sun-Earth-Moon system and the reflectivity of the fiducial patches on the Moon as a function of lunar phase. I describe this method of obtaining albedo from earthshine measurements in section 1.3. Qiu et al. [2003] estimate that a single BBSO earthshine telescope can determine a nightly value for the Earth's large-scale reflectance to an accuracy of 1%. Further, they estimate that their albedo estimates have a 1% precision over a year[1].

Early BBSO earthshine measurements from the period 1999 to 2003 showed an increasing albedo trend [Pallé et al., 2004] conflicting with satellite data from CERES showing a decreasing albedo trend in the period 2000 to 2003 [Wielicki et al., 2005]. Since then, the BBSO earthshine

[1]Note here that large-scale reflectance and albedo are two different things. The albedo is a well-defined, but hard to determine quantity that requires knowledge of the phase-functions etc.

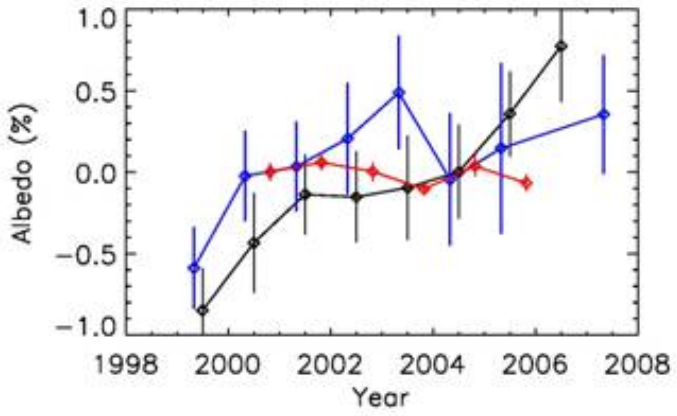

Figure 1.6: Average yearly albedo anomalies derived from BBSO earthshine *(blue)*, CERES *(red)* and ISCCP-FD *(black)*. All three estimates show no statistically significant trend in the 2000-2006 period. Both Earthshine and ISCCP-FD data have an increasing trend in albedo for 1999-2000, where there are no CERES data available. The picture is more muddy in 2006-2007, possibly due to calibration issues with the ISCCP data [Pallé et al., 2009].

data has been reanalyzed[2], the CERES data has been recalibrated, and ISCCP has released their flux data (FD) product with estimates of the TOA albedo. Pallé et al. [2009] compared BBSO earthshine albedo estimates from the period 1999 to 2007 with those from CERES and ISCCP-FD. Figure 1.6 shows the annual mean albedo anomalies derived from the three datasets. The three are in reasonable agreement.

1.3 From Earthshine to Albedo

From the surface of the Earth we can observe the earthshine of the Moon and get an instantaneous measurement of the Earth's large-scale reflectance. During a given night, roughly a third of the Earth contributes to the Earthshine as seen from a single observatory site. Near New Moon when the Earth is nearly full, a larger part of the Earth contributes to the instantaneous earthshine, but the observation time is short since the Moon is close to the horizon. For smaller lunar phases when the Earth is nearly new, a much smaller part of the Earth contributes to the instantaneous earthshine, but the observation time is relatively longer allowing different parts of the Earth's surface to contribute to the earthshine during the night.

[2]BBSO introduced a new systematic method for rejecting poor nights. This resulted in a less extreme increasing albedo trend for 1999-2003 [Pallé et al., 2009].

Bond albedo

For climate research purposes, the quantity of interest is the planetary albedo, also known as the Bond albedo. The Bond albedo is the fraction of total electromagnetic radiation incident on the Earth that is scattered back to space. All wavelengths and phase angles are taken into account. The Bond albedo is often expressed as the geometric albedo times a phase integral.

$$A_{\text{Bond}} = p_{\text{e}} \int_{-\pi}^{\pi} f_{\text{e}}(\beta)\, |sin(\beta)|\, d\beta. \tag{1.5}$$

Since it is the Bond albedo of the Earth, p_{e} is the geometric albedo of the Earth, and $f_{\text{e}}(\beta)$ is the phase-function of the Earth.

In practice the albedo is rarely measured across the entire spectrum. 99% of the Sun's radiation is shortwave in the range 0.15 to 4.0μm. This covers ultra-violet to infra-red. We measure the earthshine intensity in five broad bands covering visual to infra-red (information about our colour filters can be found in subsection 2.1.4).

Any one measurement of reflected light from Earth, whether it is obtained from a satellite or with an earthshine telescope, only covers one scattering angle. One must extrapolate over all scattering angles to obtain the entire phase-function of the integral. The measurements from satellites can be extrapolated using complex scene models. With Earthshine many different scattering angles are covered by measuring the earthshine at different lunar phases. A remaining difficulty is that measurements are necessarily restricted to light scattered from the Earth to the lunar orbit.

Geometric albedo

The geometric albedo of an astronomical body is the ratio of its brightness at zero phase angle to that of a Lambertian (perfectly diffusing) disc with the same cross-section. Zero phase angle means normally incident radiation. In the case of the Sun-Earth-Moon system, we can observe the geometric albedo of the Moon from Earth during a lunar eclipse. Alternatively, the lunar / terrestrial geometric albedo can be observed by satellites orbiting the Moon / Earth.

Phase-functions and the Lambert assumption

A phase-function is the reflected intensity as a function of angle normalized by the intensity at normal incidence, so that f(0) = 1. We must know how the reflectance of the Earth and the Moon changes with the geometry of the Sun-Earth-Moon-observer system.

The Earth's sunlight reflectance is anisotropic in a non-trivial manner. The global reflectance is built up by a large variety of individual surface types (and changing cloud cover) each with their own reflective properties. Earthshine observations measure the large-scale reflectance and therefore average over a wide range of different surface types. The anisotropic properties of the individual elements are thus subdued, and the reflectance of the Earth as a whole can be assumed to be isotropic [Flatte et al., 1992, Qiu et al., 2003].

We will assume the Earth is a perfect Lambert sphere: an ideal diffusely reflecting surface. This is of course the same as saying the reflectance is isotropic. For a Lambert sphere, the geometric albedo has a simple linear relationship with the Bond albedo [Qiu et al., 2003]

$$p_{\mathrm{L}} = \frac{2}{3} A_{Bond,\mathrm{L}}, \tag{1.6}$$

and the Lambert phase-function is [Qiu et al., 2003]

$$f_{\mathrm{L}}(\beta) = \frac{(\pi - |\beta|)\cos\beta + \sin|\beta|}{\pi}. \tag{1.7}$$

A Lambert sphere is a good approximation when the exact characteristics of the surface are unknown. However, the approximation doesn't always hold. An example is sunglints: A calm cloud-free ocean reflects much like a mirror (specular reflection), where light from a single incoming direction is reflected to a single outgoing direction.

Effective albedo

I will define Earth's effective albedo as the albedo of a Lambert sphere with the same instantaneous reflectivity as the true Earth for the same phase angle. In the observations, we compare the intensity of pairs of opposing patches on the Moon: one patch on the dark side that gives us the earthshine intensity and one on the bright side that gives us the moonlight intensity. Simple geometric considerations [Flatte et al., 1992, Goode et al., 2001, Qiu et al., 2003] show that the effective albedo is given by

$$A_{\mathrm{eff}} = \frac{3}{2}\frac{1}{f_{\mathrm{L}}(\beta)}\left(\frac{R_{\mathrm{em}}}{R_{\mathrm{e}}}\right)^2\left(\frac{R_{\mathrm{oa}}}{R_{\mathrm{ob}}}\right)^2\left(\frac{R_{\mathrm{es}}}{R_{\mathrm{ms}}}\right)^2\frac{p_{\mathrm{b}} f_{\mathrm{b}}(\theta)}{p_{\mathrm{a}} f_{\mathrm{a}}(\theta_0)}\frac{I_{\mathrm{a}}}{I_{\mathrm{b}}}. \tag{1.8}$$

The quantities of the equation are summarized below, and the geometric angles are illustrated in the schematic drawing of figure 1.7. The ratio $R_{\mathrm{oa}}/R_{\mathrm{ob}}$ is very close to unity and could be left out of the equation.

$f_{\mathrm{x}}()$	phase-function of x at relevant angle
p_{x}	geometric albedo of patch x
R_{xy} or R_{x}	distance between x and y or radius of x
a	earthshine patch
b	moonlight patch
e	Earth
m	Moon
o	observer
θ	lunar phase angle, $\theta \in [-\pi, \pi]$ with $\theta = 0$ being a Full Moon
β	Earth's phase angle, $\beta \in [-\pi, \pi]$ with $\beta = 0$ being a full Earth
θ_0	the angle between the earthshine that is incident and reflected from the lunar patch of interest as seen by the observer

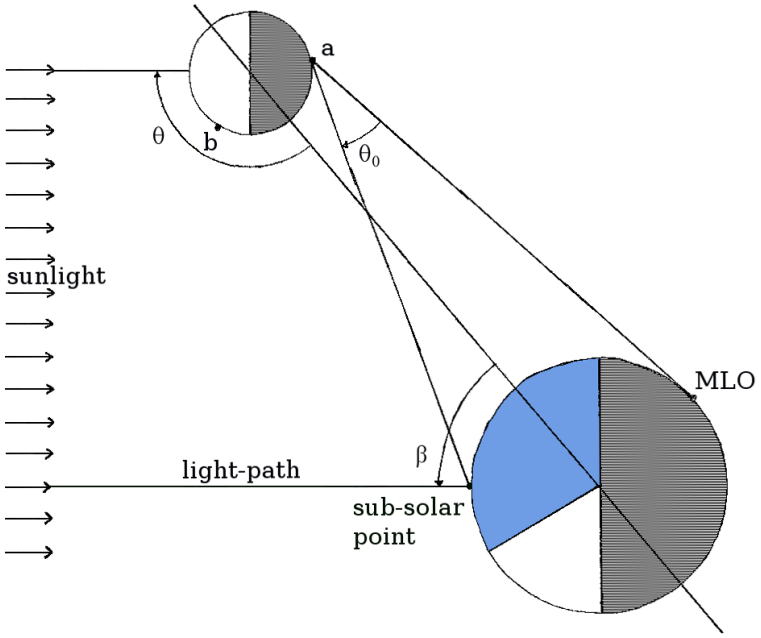

Figure 1.7: Sketch of the Sun-Earth-Moon system for a waning Moon. The blue area on the Earth shows the approximate longitudes that contribute to the earthshine. θ is the lunar phase angle, and β is Earth's phase angle. θ_0 is the angle between the earthshine that is incident and reflected from the Moon, and it is always a very small angle of order 1° or less.

Equation 1.8 shows that deriving albedo from earthshine and moonlight intensities requires knowledge of the geometry of the system and the reflective properties of the regions of interest on the lunar surface. The phase-function of the Moon is of special importance.

The lunar phase-function

It is possible to determine the phase-function of the Moon from observations over many Moon cycles. The BBSO group has done this, and their result is shown in figure 1.8. Their phase-function is not well determined for small angles and only extend to about $\pm 150^\circ$. Qiu et al. [2003] have made observations in the lunar phase range $\pm 40^\circ$ to $\pm 150^\circ$. However, the lunar phase-angle is only the relevant angle for the bright side observations. The earthshine is incident from the Earth and reflected to the Earth (the angle θ_0), and is therefore always observed at angles below 1°.

At small phase angles the phase-function increases dramatically as the reflected light is almost exactly backscattered. The sharp peak around full Moon is called the opposition effect. The enhancement is a reflective property of the porous nature of the lunar surface. It is thought to be a combination of shadow hiding and coherent backscatter. Hapke et al. [2012] have recently published the lunar phase-function with data from

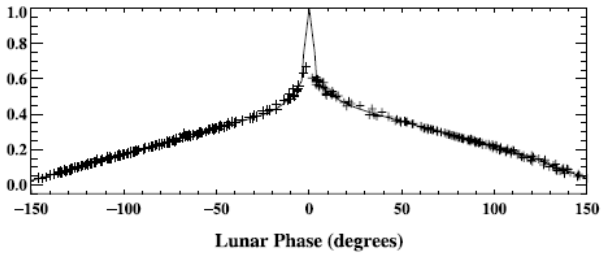

Figure 1.8: The phase-function of the Moon as measured by BBSO. It has been normalized and corrected for local atmospheric effects, relative declination as well as the libration of the Moon [Qiu et al., 2003].

the Lunar Reconnaissance Orbiter, giving special care to the opposition effect. This is the first time that reliable data exist for the smallest phase-angles, and this will improve the accuracy of albedo determinations from earthshine measurements. In appendix A.1 I list important contributions to the understanding and knowledge of the lunar phase-function.

Exact knowledge of the lunar geometric albedo and phase-function is only necessary if the interest is absolute values of the albedo. For climatic research, the changes in albedo are more interesting, and then it is less important if their is a constant bias due to incorrect knowledge of the reflective properties of the Moon.

1.3.1 Full Forward Modelling

There is an alternative route to determine the terrestrial albedo from Moon observations. Thejll et al. [2012, submitted to A&A] have developed novel methods based on forward modelling. One of them, the full forward model (FFM) method distinguishes itself from other methods by providing terrestrial albedo values directly, rather than earthshine and moonlight intensities.

The core in the FFM method is synthetic Moon images. These images simulate the appearance of the Moon in a CCD image, except they are ideal images of the Moon, unaffected by stray light. They are produced with a lunar radiance model that contains a photometric description of both the Earth and the Moon, and that uses the Earth model to illuminate the Moon with earthshine. The geometry of the Sun-Earth-Moon-observer system is taken into account, and light rays are traced from the surface of the Moon to individual CCD pixels. The lunar radiance model incorporates all the quantities in the expression for the effective albedo (1.8).

Realistic, simulated "observed" images of the Moon are generated from the synthetic images. This is done by convolving the synthetic images with an empirically determined halo profile representing the scattered light and adjusted for nightly conditions. This model is fitted to the real Moon observations on both the sky and the lunar disc. The terrestrial albedo is a parameter in the model, and can be determined from the best fit.

Chapter 2

The Earthshine Telescope

Development and construction of the Lund-DMI Earthshine Telescope was done in collaboration between Lund Observatory and the Danish Meteorological Institute (DMI). The telescope is designed to obtain long-term albedo data sets through observation of the ratio between intensities of the bright and dark sides of the Moon. The design was initiated in 2006 and the first prototype was installed at the Mauna Loa Observatory on Hawaii in spring 2011 and is currently being tested. It is this telescope that is the subject of my thesis.

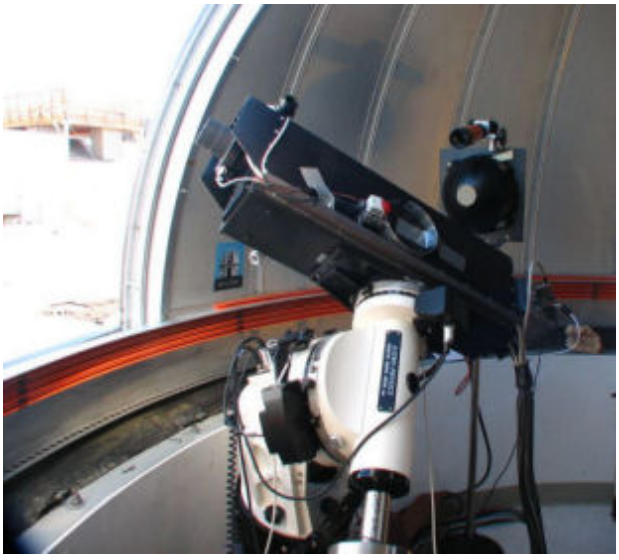

Figure 2.1: The Earthshine Telescope in its dome on Mauna Loa at an altitude of 3397m. The telescope is mounted on an Astro-Physics 1200GTO German equatorial mount.

The Earthshine Telescope is designed to be remotely operated, and in time be completely automatic. The science objective is long-term monitoring of the Earth's albedo with a precision of 0.1%. If the telescope is

successful, the plan is to build more telescopes and position them at different longitudes for global coverage.

The high precision requirement has posed strict demands on the design of the telescope. The earthshine intensity is up to 10,000 times fainter than the moonlight intensity with the exact ratio depending on the phase of the Moon (and the albedo). This poses a challenge, since CCD detectors have a limited dynamical range. The Earthshine Telescope has four modes of operation that all allow measurements of the intensity ratio. Because the earthshine is so faint, stray light at the dark side arising from the bright side is a major concern, and the telescope has been designed to minimize scattering.

2.1 Layout of the Telescope

The Earthshine Telescope is a small refractor with an aperture stop of just $40mm$. The aperture has been kept small to lengthen the possible exposure times when observing the bright part of the Moon. The system has three lenses that produce two image planes. The first image plane holds a wheel with knife-edges used in three of the four operational modes. The CCD camera is situated in the second image plane. Figure 2.2 is a photograph of the telescope without its protective cover. In the following, I will describe the different components of the telescope.

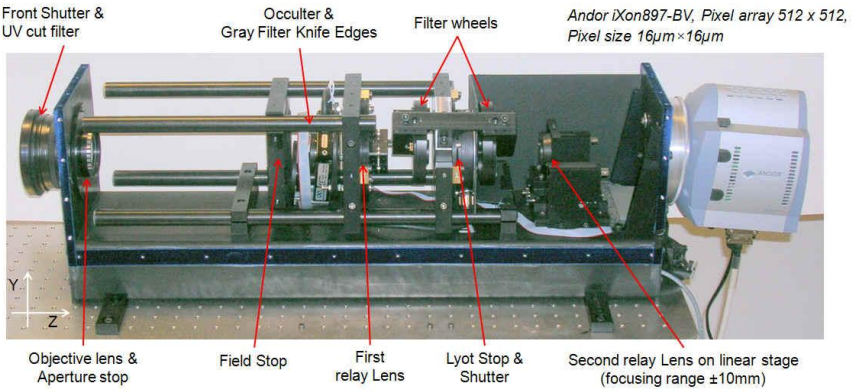

Figure 2.2: The Earthshine Telescope's interior. Some of the components are tilted slightly to minimize ghost images [Darudi et al., 2010].

2.1.1 Optical Layout of the Telescope

The optical layout of the Earthshine Telescope is shown in figure 2.3. The objective is a $50mm$ lens with a focal length of $250mm$. This is followed by two afocal relay lenses that have the function to extend the optical tube. The first relay lens has a diameter of $25mm$ and a focal length of $75mm$, and the second relay lens is a $30mm$ lens with a focal length of $150mm$. The purpose of the relay optics is both to provide two times magnification and

to form a real image of the aperture stop between the two relay lenses. A Lyot stop placed here can then block the difraction rings of the bright side of the Moon created by the aperture stop.

All three lenses are achromatic doublets. The objective and the first relay lens has a VIS-NIR AR coating optimized for the visible and near infrared range, and the second relay lens has a VIS-0° AR coating optimized for visible light and an angle of incidence of 0°. The AR stands for anti-reflex coating.

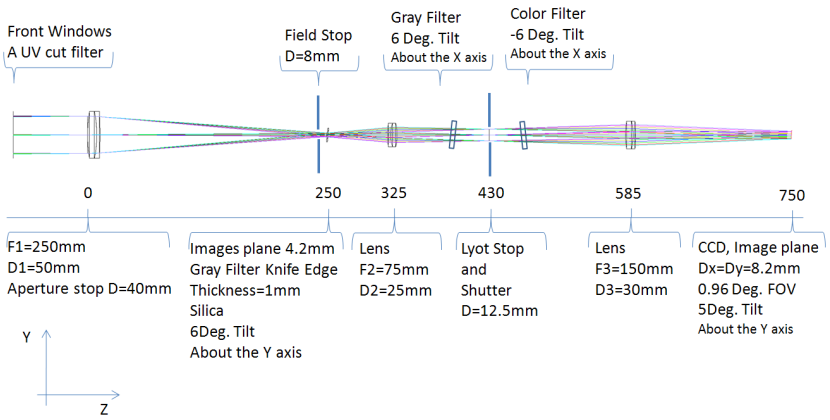

Figure 2.3: The optical layout of the telescope [Darudi et al., 2010].

The image that is formed in the first focal plane, is magnified by the ratio of the focal lengths of the relay lenses. Therefore, the total focal length of the three-lens system is

$$f = f1 \cdot \frac{f3}{f2} = 250mm \cdot \frac{150mm}{75mm} = 500mm. \tag{2.1}$$

It is the aperture stop that limits the incident beam, so the f-ratio of the system is $500mm/40mm = f/12.5$. This is a relatively slow f-ratio, limiting the brightness of the lunar image in the focal plane, allowing for longer exposure times without over-exposure.

Under the paraxial approximation[1] the image scale in arcsec per mm can be determined as

$$\text{image scale} = \frac{206265}{f} = 412.5'' \, mm^{-1}, \tag{2.2}$$

and the field of view of the telescope is

$$\text{FOV} = \text{image scale} \cdot \text{length of CCD} \approx 0.94°. \tag{2.3}$$

The lunar angular diameter is 0.5°, so a FOV of 0.9° is perfect for our purpose. It allows us to observe the whole Moon and some of the surrounding sky in a single image.

[1]The paraxial approximation is the assumption that all incident rays are nearly parallel to the optical axis.

2.1.2 Stray Light

Stray light is any light that does not come from the object of interest[2], but still illuminates the detector thus lowering the sensitivity and washing out contrasts. Earthshine observations are an extreme case, where the object of interest, the dark side of the Moon, is right next to an extremely bright source. Light from the bright side of the Moon scatters in the atmosphere, creating a halo around the Moon that adds unwanted intensity to the earthshine. Furthermore, light is scattered in the lenses, again adding intensity to the earthshine, generally lowering the sensitivity of the detector, and creating ghost images. Dust on lenses is common source of scatter.

The amount of stray light inside the telescope can be reduced through an appropriate telescope design. The scattered light in the sky and any remaining scattered light inside the instrument must be removed from the images with special data reduction steps.

A UV cut-off filter is mounted in front of the aperture stop. This is important, since UV radiation will increase chromatic aberrations. The aperture stop has a diameter of $40mm$ and thus limits the light gathering power of the telescope. A field stop is located just before the first image plane, where it blocks diffracted light from the front aperture. Between the relay lenses a Lyot stop blocks additional diffracted light and prevents the detector from seeing any non-optics surface preceding the Lyot stop. The mechanical components of the instrument are made of aluminium and have been black anodized or black chromated, so that they only reflect about 0.5%.

Ghost images

Ghost images are created by light being reflected from surfaces that are supposed to be transmitting, and ending up on the CCD. The transmitting components are the doublet lenses with three surfaces each, the dewar window and the CCD itself, as well as the filters. The coating on the lenses as well as on the CCD is chosen to minimize reflection, but there will always be some reflection. If light is reflected an even number of times it may reach the CCD and create a ghost image. Some of the components, such as the filter wheels, have been tilted slightly with the effect that the ghost images are moved away from the CCD (see figures 2.2 and 2.3).

2.1.3 Knife Edges

Three of the operational modes depend on inserting a knife edge in the optical path that covers the bright part of the Moon, either occulting or dimming it. There is one solid knife edge, similar to the blocking filter that the BBSO group uses, and the rest are knife edge density filters (KEDF) with optical densities 3.5, 3.75 and 4.0. The optical density, OD, is the negative logarithm of the ratio of measured intensity, I, to incident

[2]The dark and bright side is here considered two different objects.

intensity, I_0

$$OD = -\log\left(\frac{I}{I_0}\right). \tag{2.4}$$

If the filter has $OD = 4$, then it will dim the intensity with a factor 10^{-4}.

Figure 2.4 shows a diagram of the specially designed system for positioning the knife edges. The small off-axis rotary stage is used to select the knife edge, and both the off-axis stage and the larger on-axis rotary stage are used to adjust the angle and location of the knife edge so that it covers the brigt side completely.

The KEDFs were custom-made (by Peder Steiner at Ferroperm) by evaporating aluminium on a glass plate. Each glass plate is $1mm$ thick, has a diameter of $20mm$, and is anti-reflex coated. The glass plate covers the whole optical path, but the aluminium coating only covers part of the glass plate. The solid knife edge has a physical edge and is black coated metal.

The placement of a knife edge (especially true for the solid knife edge) in front of the bright Moon, reduces the scattered light inside the telescope from bright side to dark side dramatically. On the other hand, an additional filter/clear glass plate introduces more surfaces on which light may scatter.

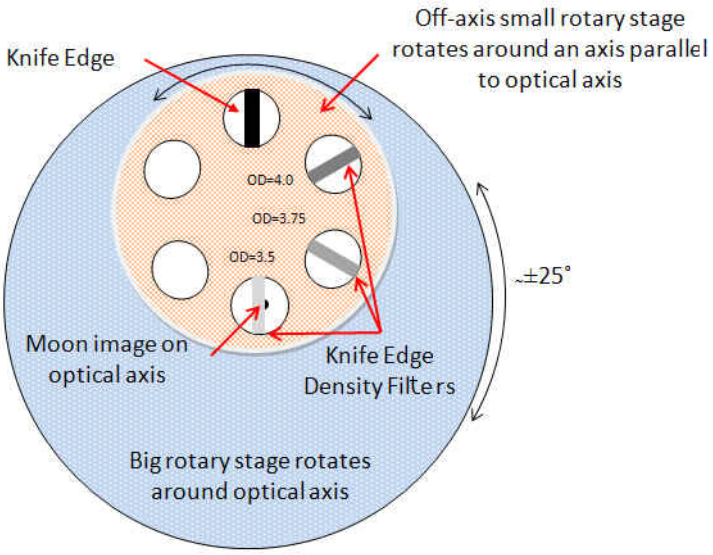

Figure 2.4: The mechanism for selecting and positioning the knife edges using two rotary stages [Darudi et al., 2010].

2.1.4 Filters

Two filter wheels are placed before and after the Lyot stop - one with colour filters and one with neutral density filters. The filters are intention-

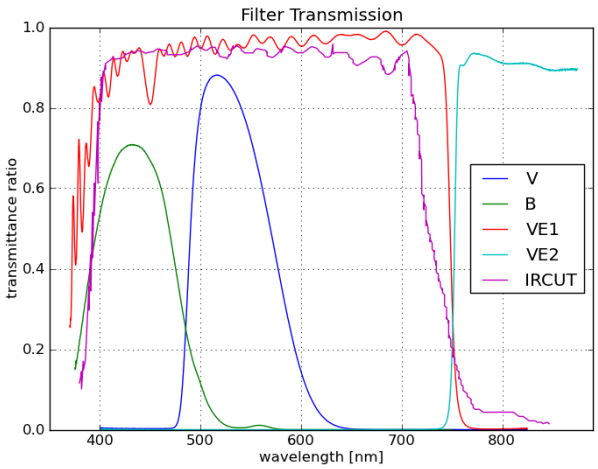

Figure 2.5: Filter transmission curves for the five colour filters constructed on the basis of data by Badínez [2010].

ally placed far away from focus to avoid dust on filters and other inhomogeneities being an issue.

Colour filters

The Earthshine Telescope has five different colour filters for broadband photometry in the range from blue to near infra-red: In the visual range we have a Johnson B with a central wavelength of 435.30nm and a Johnson V with a central wavelength of 533.67nm. We also have a lowpass and a highpass filter that have a sharp cut in transmittance at 750nm, allowing observation of the red edge vegetation index. These two filters named VE1 and VE2 respectively, can be used to look for variations in the albedo contribution from vegetation and plankton. The final filter is an infra-red cut (IRCUT) filter that is very similar to the VE1 shortpass filter, only with a less sharp cut. The BBSO group uses this exact same filter, making comparison of results easier. Badínez [2010] has measured the filter transmission as function of wavelength for the colour filters, and the transmission curves are shown in figure 2.5.

Neutral density filters

A neutral density (ND) filter is a grey filter. That is, the filter reduces intensity equally for all wavelengths. The purpose of inserting an ND filter is to allow longer exposure times, with corresponding lower relative uncertainties. We have filters with $OD = 1.0, 1.3, 2.0$. Observations of the bright side of the Moon through an ND filter must be corrected for the effect of the filter. Therefore it is important to have knowledge of the transmittance curves of the ND-filters, and the calibration must have an accuracy of 0.1%. This is also true for the knife edge density filters. Calibration routines should be performed regularly. Some calibration data

for the ND filters have been collected, but they have yet to be analysed. The ND filters are not currently in use (they are not needed before all modes are in operation, see section 2.4).

2.2 The CCD

CCD cameras (Charged-Coupled Devices) are used as photon detectors in optical astronomy. A CCD is an array of light sensitive metal-oxide-semiconductor (MOS) capacitors[3], with one capacitor per pixel. The semiconductor is typically doped silicon. Photoelectrons are generated when the CCD is exposed to light at a rate proportional to the rate of photon arrival. The photoelectrons are stored in the depletion region of the MOS capacitor. After end of exposure, manipulation of voltages transfers the charge from one capacitor to the next, and the collected charge is read out and converted to a digital number, one pixel at a time.

The camera in the Earthshine Telescope is an ANDOR iXon897-BV. The CCD is a thinned ($15\mu m$) back-illuminated CCD, which means incoming photons are absorbed directly in the silicon on the "back-side" of the CCD. This type has higher quantum efficiency than typical front-sided CCD's. The size of the CCD is 512x512 pixels, with each pixel being 16x16μm. The CCD is optimized for visual light, and both the CCD and the dewar window protecting it have an anti-reflective coating. The thermoelectric cooling system keeps the CCD temperature at $-80^{\circ}F = -62.2^{\circ}C$.

In single image mode the camera can read out about 3 frames per second. We usually obtain blocks of a 100 frames that take a couple of minutes to read out and store on a computer. The CCD is operated in standard amplification mode.

2.2.1 Readout Noise, Dark Current & Gain

Readout noise (RON) is added into every pixel every time the array is read out. RON consists of two components: Statistics in the analog-to-digital (A/D) converter and spurious electrons introduced by the electronics. Ten electrons or less per pixel is considered good. Our CCD has low RON, but it might still be a significant contributor to the error budget in Co-add mode (Co-add mode is described in section 2.3.3).

Dark current is a small electrical current in a CCD generated by thermal electrons. Thermal energy can excite electrons across the bandgap in the semiconductor. The CCD is cooled to keep the dark current small. The signal from the dark current is proportional to the exposure time.

The gain of a CCD determines how a digital number is assigned to each pixel location in the output image. It is the number of electrons needed to produce 1 ADU (analog-to-digital unit). It can therefore be thought of as a measure of the ability to increase the amplitude of the signal from input to output.

[3]If the insulator is not an oxide-insulator, then the capacitor is called a metal-insulator-semiconductor (MIS) capacitor.

gain	RON	dark current
$3.8e^-$/ADU	$8.3e^-$	$0.0002e^-/s$

Table 2.1: Gain, readout noise and dark current values provided by ANDOR [McVarnock, 2010].

2.2.2 FWC & Dynamic Range

The full-well capacity (FWC) of the CCD is the amount of charge a pixel can hold in routine operation before pixel saturation will occur. The dynamic range of the CCD is the total range for which the CCD is sensitive, and it can be determined as FWC/RON. A high dynamic range is extremely important in our case, since the earthshine is so much fainter than the moonlight.

FWC	dynamic range = FWC/RON
$153,590e^-$	18,500 or $85.3dB$

Table 2.2: Full-well capacity and dynamic range values provided by ANDOR [McVarnock, 2010].

The CCD we use has a 16-bit A/D converter, which means the largest possible count is $2^{16} - 1 = 65,535$ADU. This is called the A/D saturation level. With a gain of $3.8e^-$/ADU, the FWC is $\sim 40,500ADU$, which is lower than the A/D saturation level, and is therefore what limits the exposure time for a well-exposed image. Above the FWC saturation level we cannot expect the CCD to be linear.

2.2.3 Quantum Efficiency

The quantum efficiency (QE) of the CCD is the percentage of the incoming photons that produce a photoelectron in the silicon and that is subsequently counted. This is of course a highly wavelength dependant quantity. When observing something as faint as earthshine every photon counts, and therefore the CCD has been chosen to have a high QE.

As mentioned above, our CCD has been physically thinned to only $15\mu m$, and is illuminated from the back-side. The incoming photons can therefore be absorbed directly in the silicon[4], thus raising the QE. The disadvantage of a thinned CCD is a lower FWC, and the possibility of non-uniform thinning resulting in a non-uniform flatfield (This does indeed seem to be the case. See section 5.2.1).

Silicon is a good reflector of optical light, and therefore the CCD is coated with anti-reflective coating to increase the QE of the CCD.

[4]In a front-sided CCD the photons must pass the "gate-structure" that is responsible for charge transfer during read-out before reaching the silicon.

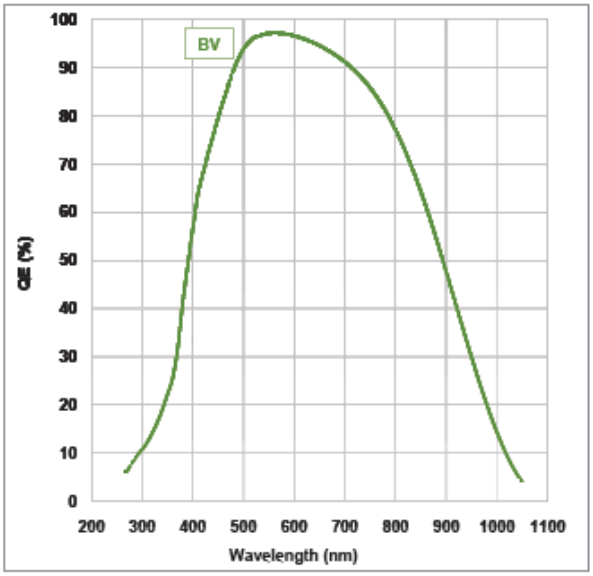

Figure 2.6: Quantum efficiency curve for the CCD. The peak QE is 92.5% at 575nm [ANDOR website].

2.3 The operational modes

2.3.1 BBSO Mode

The first operational mode has been named after the Big Bear Solar Observatory since it is the method used in their earthshine program [Goode et al., 2001, Pallé et al., 2009, Qiu et al., 2003]. In the BBSO mode the bright and dark sides of the Moon are observed one at a time. When observing the dark side, the bright side is covered with an occulter (a solid knife edge) in order to prevent saturation of the bright side. The exposure times are up to 10,000 times longer for the dark side than for the bright side.

As the two images are non-simultaneous, there might be differences in the images due to fast variations in instrumental sensitivities and sky transmission. Also, the short exposure times of the moonshine observations have large relative uncertainties.

2.3.2 Modified BBSO Mode

As in BBSO mode the bright and dark sides of the Moon are observed sequentially, and the bright side is shielded by an occulter during observations of the dark side. However, when observing the bright side, the whole Moon image is dimmed using a neutral density filter, thereby prolonging the possible exposure times. Thus the relative precision is improved. As for BBSO mode, there might be issues with fast variations, since the two Moon images are not simultaneous.

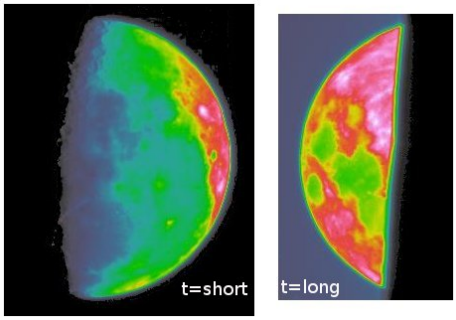

Figure 2.7: BBSO mode. The left image is the bright side of the Moon observed with a short exposure time, and the right image is the earthshine observed with a long exposure time. The solid knife edge is clearly visible as a cut-off in the earthshine image.

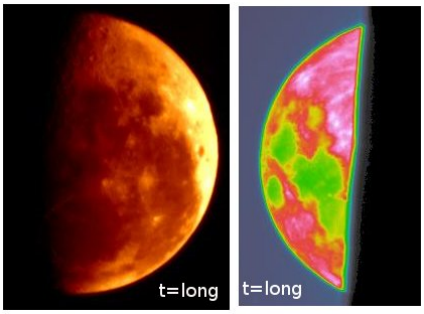

Figure 2.8: Modified BBSO mode. The left image is the bright side observed through a neutral density filter (illustrated here with a different colour) to allow for a longer exposure time. The right image is the earthshine observed with a solid knife edge covering the bright side.

2.3.3 Co-add Mode

In Co-add mode both the dark and the bright parts of the Moon are observed simultaneously in a long series of short exposures that are subsequently aligned and co-added. Each exposure is close to the saturation level of the bright side. The stacking of many frames allows the signal-to-noise of the dark side to build up, without over-exposure of the bright side. We expect this method to be well-suited for the conditions near New Moon, where the earthshine intensity is close to its maximum and the straylight from the moonshine is close to minimum.

Fast variations in instrumental sensitivities and sky transmission cancel out as well as the exposure times, since the two parts of the Moon are observed simultaneosly in the same CCD frame.

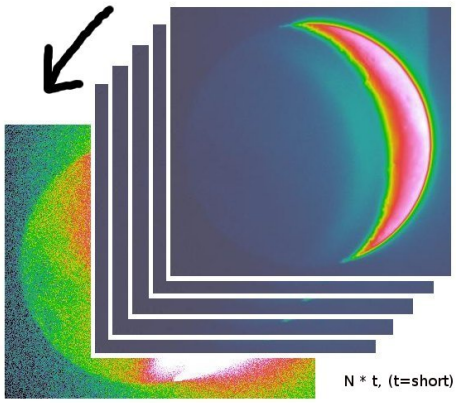

Figure 2.9: Co-add mode. Many Moon images observed close to the Full Moon are aligned and co-added. The exposure time of each individual image is short.

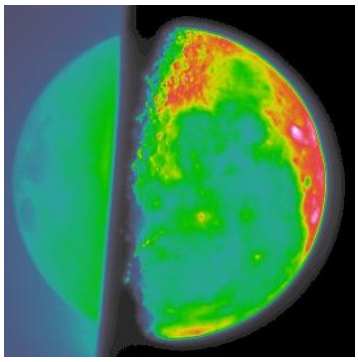

Figure 2.10: Lund mode. A knife edge density filter covers the bright side of the Moon (right part of the figure), allowing longer exposure times. That way the earthshine can be seen in the (left) part of the image, not covered by the knife edge.

2.3.4 Lund Mode

In Lund mode a knife edge density filter is placed in front of the bright side so that the intensity of the moonshine and the intensity of the earthshine are of the same order of magnitude. This allows for simultaneous observations at longer exposure times. Due to the longer exposure times, the earthshine can be observed for a larger variety of lunar phases than the Co-add mode. As for Co-add mode fast variations, both instrumental and atmospheric cancel out.

For the Lund mode, it is important with analysis of the spatial uniformity of the KEDFs, since they are located in the first focus, and any non-uniformity will show up in the acquired images.

2.4 State of Affairs

I am finishing this thesis in May 2012, almost a year into the test-period of the Earthshine Telescope. It is an appropriate time to take stock of the telecope system. Here, I will briefly mention a few issues that will have to be fixed in the nearest future.

- The telescope is planned to be fully automatic. Before this can become reality, we must have an integrated weather monitoring system. A weather station is already attached to the roof of the control building, but it has never been tested, and we need software that connects the weather data to the telescope control.
- The mechanism for selecting and positioning the knife edges is not working. Therefore we are currently limited to the Co-add mode. The problem is believed to be a software problem.
- The mechanical shutter from Uniblitz occasionally sticks when the dome temperature is below 4 degrees. A possible solution for the sticking problem could be a heating system for the shutter.
- Re-calibration of the mount is necessary now and then. It is possible that the polar alignment is not precise enough.
- We share the dome with another telescope that is placed in the center of the dome. This limits the directions where we can point the telescope to about half of the hemisphere. Although this does not affect the Moon observations it is still high on the wish list.

Chapter 3

Error Budget Introduction

The telescope is currently in its test-phase, and much of the work being done by the group in general and by me in particular has to do with evaluating the performance of the telescope. We need to check if the project requirements are met. As a quick reminder: The Earthshine Project aims to acquire long-term albedo data-sets with a precision of around 0.1%.

An error budget is an essential tool for this work. The quantity of interest is calculated by algebraic operations on measured quantities, each with an associated uncertainty. It is important to understand all the contributions to the final uncertainty, and to combine them correctly.

The error budget for the Earthshine Telescope has two categories: Instrumental design and data reduction. I will concentrate solely on errors arising from the data reduction part. Errors related to the instrumental design is covered in Darudi et al. [2010].

3.1 Precision and Accuracy

Measurement errors comprise random errors and systematic errors. Random errors find expression in a scatter in the measured quantity, and therefore the random error can be estimated as the standard deviation of the distribution of measured quantities. The uncertainty associated with random errors is referred to as the precision of the measurement.

Systematic errors are a bias, an error component that persists from measurement to measurement within an observation session. The bias may in part be a result of systematic long-term variations or random changes to the optical system or the environment that happen during observation, calibration or storage. Systematic errors are more difficult to estimate than random errors, and it is possible there are systematic errors we are unaware of. The uncertainty associated with systematic errors is referred to as the accuracy of the measurement. For the purpose of climate research, a constant but unknown bias is acceptable. The absolute value of the albedo is of little interest as opposed to how the albedo changes over time and how this affects the climate. A changing bias could be related to the lunar phases or it could be a parameter drift in the optical system.

Such errors are a problem since they can potentially hide the signal we are looking for - a change in the terrestrial albedo.

The error budget for the intensity ratio (chapter 8) is divided into two parts - one for the precision of the measurements and one for the accuracy.

3.2 Determining the Error on Albedo

As described in section 1.3, the terrestrial albedo can be determined from measured moonlight and earthshine intensities as

$$A_{\text{eff}} = \frac{2}{3}\frac{1}{f_{\text{L}}(\beta)}\left(\frac{R_{\text{em}}}{R_{\text{e}}}\right)^2\left(\frac{R_{\text{oa}}}{R_{\text{ob}}}\right)^2\left(\frac{R_{\text{es}}}{R_{\text{ms}}}\right)^2\frac{p_{\text{b}}f_{\text{b}}(\theta)}{p_{\text{a}}f_{\text{a}}(\theta_0)}\frac{I_{\text{a}}}{I_{\text{b}}} \tag{3.1}$$

The distance ratios $R_{\text{x}}/R_{\text{y}}$ are well determined and have negligible uncertainties. Even if this was not the case, incorrect knowledge of the geometry of the Sun-Earth-Moon system will result in systematic errors that are relatively unproblematic in the context of climate research.

The relevant uncertainties are thus connected to the last two parts of equation (3.1). The phase-function and the geometric albedo of the two areas of interest are not that well known, but if standard values are used, different albedo measurements can be compared.

Assuming all errors are independent, the relative errors can be added quadratically.

$$\left(\frac{\Delta A_{\text{B,L}}}{A_{\text{B,L}}}\right)^2 = \left(\frac{\Delta(p_{\text{b}}/p_{\text{a}})}{p_{\text{b}}/p_{\text{a}}}\right)^2 + \left(\frac{\Delta f_{\text{b}}(\theta)}{f_{\text{b}}(\theta)}\right)^2 + \left(\frac{\Delta f_{\text{a}}(\theta_0)}{f_{\text{a}}(\theta_0)}\right)^2 + \left(\frac{\Delta I_{\text{a}}}{I_{\text{a}}}\right)^2 + \left(\frac{\Delta I_{\text{b}}}{I_{\text{b}}}\right)^2 \tag{3.2}$$

The last two terms are the relative uncertainties (squared) on the intensity of an earthshine area and a moonlight area. We have little to no influence on the other terms, but the intensity ratio is the quantity that we determine from our observations through appropriate data-reduction. The quality of the telescope, the CCD and our data-reduction are contained in the relative uncertainties on intensity. I will therefore make an error budget for the intensity of such earthshine and moonlight areas.

3.3 Error on Intensity

The data from a CCD take the form of a digital image. This is extremely useful since we can manipulate the image mathematically to improve it or extract information. The perfect digital image has pixel values (in units of ADU) that are directly proportional to the number of photons arriving from the source by the most direct path of light. This perfect image is influenced by nothing but the intensity of the source. In reality the digital image (the raw object image) is subject to imperfections that are either additive, multiplicative or non-linear.

Additive contributions

There is no way to distinguish one electron from another. We cannot tell if the number of electrons counted in a pixel is a photoelectron from the

source, a photoelectron produced by stray light, a cosmic ray or even a thermal electron produced by the pixel itself. Background radiation is emitted by background objects (stars and galaxies) and the Earth's atmosphere. The effect from all of the examples is to add ADUs to one or more pixels.

Multiplicative contributions

The Earth's atmosphere absorbs some of the incident radiation. Inside the telescope, radiation is absorbed and reflected and possibly cause interference. Furthermore there may be temporal or spatial variations in the quantum efficiency or in the gain of the CCD. The effect is to change the pixel values to another value proportional to the source-photoelectron number of the pixel.

Non-linear contributions

Modern CCD cameras generally have a linear response, that is the gain is independent on the number of photoelectrons produced in a pixel. However, the detector sensitivity decreases above a certain treshold in signal level - pixels saturate. The linearity range of our CCD is limited by its full-well capacity - the amount of electrons a pixel can hold. Above this level electrons will spill into the surrounding pixels. It is possible to automatically discard saturated images with an appropriate computational filter.

Data reduction

The raw object image contains information about all of the above effects, and the imperfections (unwanted information) must be removed as well as possible before it can be used for scientific purposes. Data reduction is the process of discarding and combining data to reduce their information content and their volume.

In the earthshine case, we are typically interested in extracting the intensity of a patch on the Moon as represented by perhaps the average of 10x10 pixel values (or a larger area), after removing the imperfections. An alternative approach is to compare the earthshine intensity to the flux of the whole image after scattered light has been removed. Often we will reduce the data further by averaging over many images of the Moon. Sections 3.3.1 and 3.3.2 describe how an image representing the intensity is obtained from the raw object image. Each of the steps taken to improve the image involuntarily adds uncertainty. Section 3.3.3 combines the error contributions from the individual reduction steps into a final expression for the uncertainty in the measured intensity.

3.3.1 Basic Image Reduction

The basic image reduction steps are bias- or dark subtraction and flatfield correction. These steps remove some instrumental effects and are necessary for all observations performed with a CCD camera.

Bias

If the CCD is read out unexposed, the digital image will contain positive pixel values even though no photons were absorbed. Typically the pixel values will have a small Gaussian distribution around a value of $300 - 500$ADU, called the bias level. Upon readout of a frame, the on-chip electronics and the A/D converter produce count values with a small Gaussian distribution about zero. A positive offset value - the bias level - is added to all frames in order to avoid negative values. The bias level must be subtracted from the object images. In practice, a bias frame is obtained as an image with closed shutter and minimal exposure time, a small fraction of a millisecond. Bias frames allow us to measure the bias offset level and determine the uncertainty of the level.

Dark

Thermal electrons are generated in the CCD from the energy in the lattice vibrations. The dark current is strongly temperature dependent and accumulates charge in a pixel at a rate [Chromey, 2010, p. 252]

$$D = A_0 T^{3/2} \cdot \exp\left(\frac{-E_g}{2k_B T}\right). \tag{3.3}$$

Here A_0 is a pixel dependent constant, T is the temperature in Kelvin, $E_g = 1.12eV$ is the silicon band-gap energy and k_B is Boltzmann's constant. This is why CCDs are cooled. At room temperature a typical CCD would saturate from dark current in a matter of seconds.

The signal generated from the dark current is removed from an object image by subtracting a dark frame. A dark frame is obtained as an image with closed shutter and the same exposure time as the object frame. The bias level is contained within the dark frame, which means that no bias correction is needed if the image is dark corrected. The CCD we use have negligible dark current (see 4.4) and therefore we can simply subtract a bias frame.

Flatfield

In the perfect world a source of uniform radiation illuminating the CCD would result in a uniform output. However, CCDs are far from perfect. Each pixel has a slightly different light sensitivity and there may be distortions of the optical path (eg. dust, fingerprints, insects etc. on lenses or filters), leading to non-uniform illumination of the detector. The correction is done by dividing the object image with a flatfield. A flatfield is essentially a two-dimensional map of the CCD sensitivity. It is obtained as an image of a perfectly uniform (flat) source, observed with the entire telescope system.

Corrected image

The arithmetic operations representing bias and flatfield corrections are carried out pixel by pixel over the entire object image. The corrected in-

tensity image for the exposure time t is given by

$$I = \frac{O - B}{F - B}\frac{1}{t}, \tag{3.4}$$

where O is the object image, B is the bias frame and F is the flatfield. $1/t$ cancels out in Co-add mode and Lund mode, because two intensities with the same exposure time is divided with each other.

In practice, the flatfield is normalized after bias subtraction, and the error on the normalized flatfield is determined experimentally. I can therefore write equation (3.4) as

$$I = \frac{O - B}{tF'}, \tag{3.5}$$

where F' is a master flatfield (see section 5.2).

3.3.2 Scattered Light

As mentioned in section 2.1.2, an important data reduction step is removal of scattered light that originates on the bright side - the halo. Both the atmosphere and the telescope contribute to the scatter, and the result is that unwanted intensity is added to the earthshine. In principle, the bright side is also affected by the scattering, but the effect is negligible. The scattering will cause neighbouring bright side pixels to both lose and receive additional photons.

The scattered light can be represented as an image that is subtracted from the object frame O. In this case, the scattered light introduces another term in the intensity equation (3.4), so that it becomes

$$I = \frac{O - S - B}{tF'}. \tag{3.6}$$

3.3.3 Error Propagation

Assuming random and independent errors, the general rule for error propagation states that

$$\Delta I = \sqrt{\left(\frac{\partial I}{\partial O}\right)^2(\Delta O)^2 + \left(\frac{\partial I}{\partial S}\right)^2(\Delta S)^2 + \left(\frac{\partial I}{\partial B}\right)^2(\Delta B)^2 + \left(\frac{\partial I}{\partial F'}\right)^2(\Delta F')^2 + \left(\frac{\partial I}{\partial t}\right)^2(\Delta t)^2} \tag{3.7}$$

with the partial derivatives

$$\frac{\partial I}{\partial O} = \frac{1}{tF'} \tag{3.8}$$

$$\frac{\partial I}{\partial S} = -\frac{1}{tF'} \tag{3.9}$$

$$\frac{\partial I}{\partial B} = -\frac{1}{tF'} \tag{3.10}$$

$$\frac{\partial I}{\partial F} = \frac{S + B - O}{tF'^2} \tag{3.11}$$

$$\frac{\partial I}{\partial t} = \frac{S + B - O}{t^2F'}. \tag{3.12}$$

The square of the relative error is then

$$\left(\frac{\Delta I}{I}\right)^2=\left(\frac{\Delta O}{O-S-B}\right)^2+\left(\frac{\Delta S}{O-S-B}\right)^2+\left(\frac{\Delta B}{O-S-B}\right)^2+\left(\frac{\Delta F'}{F'}\right)^2+\left(\frac{\Delta t}{t}\right)^2. \tag{3.13}$$

It can be seen from equation (3.2) that equation (3.13) is an important term in the full error budget for the albedo. This form also has the advantage that it is easily transformed to a signal to noise ratio, $S/N = I/\Delta I$.

3.4 Co-add Mode & its Errors

In this thesis I have focused on Co-add mode, because at the time of writing (May 2012) it is the only fully operational mode (see section 2.4). Co-add mode is by far the most simple mode. First of all, it has no additional optical elements such as neutral density filters or knife edges that give rise to additional uncertainties. Secondly, it is one of the simultaneous modes, the other being the Lund mode. The simultaneous modes have the strong advantage that fast atmospheric and instrumental variations cancel out in the ratio of the intensities. In the simultaneous modes, the exposure times likewise cancel out in equation (3.6), which is a big advantage at the moment where we are experiencing problems with shutter reliability.

The disadvantage of Co-add mode is that we can only observe in a certain phase range around new-moon ($\pm 90^\circ - 150^\circ$ with 0° being a Full Moon), when the earthshine is close to its maximal intensity. Since Co-add is a simultaneous mode, the relative error equation (3.13) becomes

$$\left(\frac{\Delta I}{I}\right)^2=\left(\frac{\Delta O}{O-S-B}\right)^2+\left(\frac{\Delta S}{O-S-B}\right)^2+\left(\frac{\Delta B}{O-S-B}\right)^2+\left(\frac{\Delta F'}{F'}\right)^2. \tag{3.14}$$

Equation 3.14 lists the quantities that I will need in an error budget for the earthshine (or moonlight) intensity measured with the Co-add mode on the Earthshine Telescope. The error equation has a term for the raw object frame O, the bias frame B, the flatfield F and the scattered light S. In the following chapters 4, 5 and 6, I have estimated the errors, ΔB, ΔF and ΔS. The error related to the object frame, ΔO is treated in section 8.1.1. I will estimate the relative magnitudes of the four terms of equation (3.14) in chapter 8.

Equation (3.14) is appropriate both for a single pixel as well as for an entire 512x512 pixels frame, where the arithmetic operations are again performed pixel by pixel.

Chapter 4

Bias, Dark & RON

4.1 Bias & Superbias

I introduced the concept of bias subtraction in section 3.3.1. A bias frame is an image taken with closed shutter and minimal exposure time, and it contains noise and the bias level that has been added to avoid negative numbers. It is always necessary to subtract a bias frame from a science image obtained with a CCD camera.

In this and the following sections (4.1-4.3), I will examine the bias of the CCD in the Earthshine Telescope. I construct a superbias that we presently use in the data reduction of earthshine data, determine the bias level and estimate its uncertainty. The bias level has both spatial structure and is periodic, properties that are important to know if the bias level is to be subtracted correctly.

4.1.1 Superbias

The bias level can be estimated as the average pixel value of a bias frame, and its uncertainty as the standard deviation of the pixel values. However, in any single bias frame there are random fluctuations, readout noise variations and possibly cosmic ray hits. Therefore, the bias frame used in the image reduction should be an average or median frame of many individual bias frames. I have chosen to use a combination, the mean-half-median method, described in section 4.1.2 below. Furthermore, because bias frames have two-dimensional structure (see section 4.1.3), it is necessary to subtract the whole bias frame from the science frame, pixel by pixel.

Both the 2D structure and the general bias level are stable from night to night[1], allowing us to construct a single superbias to be used in the reduction of all future images. The stability should be checked from time to time. There may be a slow drift over the course of many months, so that a new superbias should be constructed 2-3 times a year.

[1] The bias level is stable, apart from the 20 minutes period described in section 4.3

4.1.2 Constructing the Superbias

I have written an IDL program "superbias.pro" (see appendix B.1) where I construct a superbias from 1104 bias frames obtained in the period October 11 2010 to June 18 2011. The earliest of these were obtained while the telescope was beeing tested in Lund, but the majority of the frames are from Hawaii. Prior to running the program, I made sure the bias level and 2D structure were unchanged from Lund to Hawaii.

The program constructs a datacube of all the bias frames and rejects those with a mean value too different from a "best bias". I ran the code several times, each time inserting the previous superbias as the current best bias. After a few runs, it was the same frames that were rejected each time. In total 8 frames out of 1112 were rejected leaving me with 1104 bias frames. The rejection condition was

$$-10 < \text{mean(bias - best bias)} < 10$$

From this datacube I construct the superbias by applying the mean-half-median method. The resulting superbias is displayed in figure 4.1.

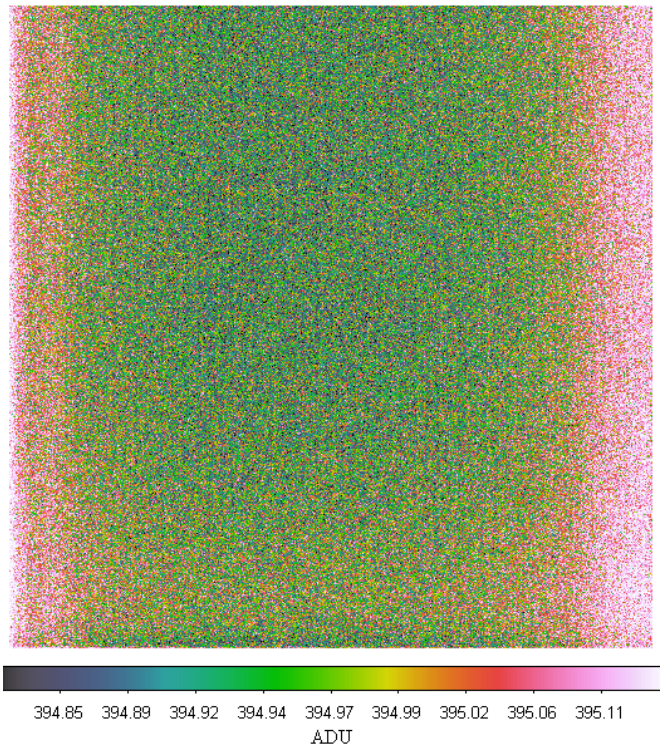

Figure 4.1: The superbias we use in image reduction. It is constructed from 1104 bias frames using the mean-half-median method. The bias level is 394.975 ± 0.088ADU. The image is histogram equalized and coloured to emphasize the structure in the bias.

Mean-half-median Method

The mean-half-median is the mean of the values in the interquartile range of the dataset. That is, the dataset is subjected to a median filter removing the 25% lowest values and the 25% highest values, and the mean-half-median is then the arithmetic mean of the remaining central 50%.

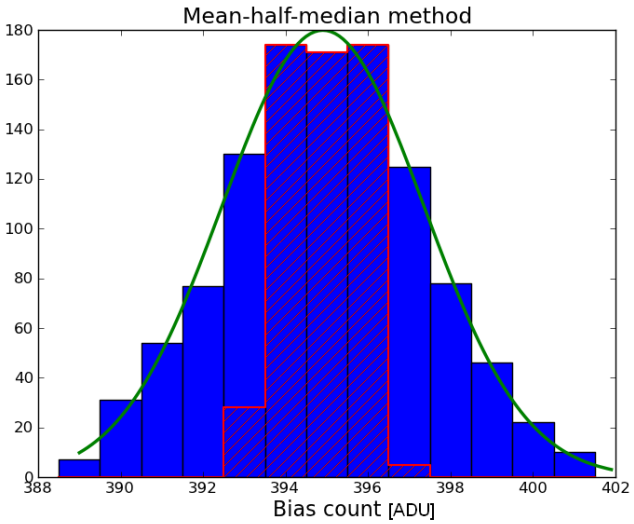

Figure 4.2: The blue histogram is the distribution of bias values in a single pixel in the 1104 bias images used in the construction of the superbias. The 25% lowest and highest values are removed leaving the central 50% shown in the red hatched histogram. The mean of these half-median values is assigned to that particular pixel position in the superbias. The green curve is a Gaussian function, and it is clear that the bias distribution of a single pixel is well fitted by a Gaussian function.

When creating the superbias from a datacube of bias frames, the mean-half-median method is applied pixel-by-pixel. For each pixel-column in the datacube, the mean-half-median is found and assigned as the superbias value of that particular pixel. Figure 4.2 illustrates the method for a randomly chosen pixel in the superbias. The count values in the 1104 different bias frames for this one pixel (the blue histogram) are roughly a Gaussian distribution (the green curve). After the median filtering, the count values form the red histogram, and the mean of this is the superbias count value.

The advantage of applying a median filter prior to determining the mean, is that the method is robust in the presence of outliers. There are no extreme outliers in the example given above, and therefore the mean-half-median is very close to the mean of the full dataset.

This method is not only used in the construction of the superbias, but also in constructing the master flatfields and when co-adding a large number of object frames.

4.1.3 Fixed 2D-Pattern

The superbias (fig 4.1) has a discernible two-dimensional structure. This is a pattern inflicted on the CCD during the manufacturing process, and it is not uncommon. The presence of a two-dimensional pattern means it is necessary that the bias subtraction is done pixel-by-pixel rather than simply subtracting the mean bias level. Fortunately, the 2D structure is stable with time.

The structure becomes more evident with a smoothing of the superbias. I have smoothed the bias by compressing the image array to the size of 64x64 pixels and then reexpanding it to the original 512x512 pixels. A surface plot of the smoothed bias is shown in figure 4.3. The shape is something similar to a skate ramp and the high level edges are seen in the actual superbias frame as well (fig 4.1) where the left and right edges are much brighter than the rest of the bias frame.

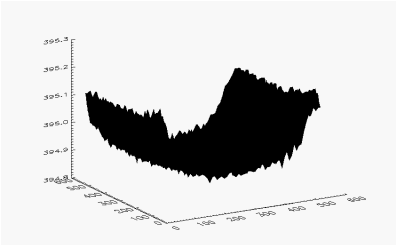

Figure 4.3: Smoothed superbias by compression to 64x64 pixels and reexpansion. This is an approximation of the fixed two-dimensional pattern of the bias.

4.2 Error on Superbias

It is important to have a good estimate of the uncertainty in the bias level. Subtracting a bias frame from the object frame is one of the basic image reduction steps, and in the process the error on the bias adds to the error on the intensity we are trying to measure. When observing low intensities such as earthshine, the error on bias becomes increasingly important. This is especially true in Co-add mode, where the exposure times are short, and the intensity of the earthshine corresponds to only a few counts per pixel after subtraction of bias.

If the bias was perfectly smooth with negligible 2D-structure then a histogram of the values would have a Gaussian shape, and the standard deviation would be a good estimate of the uncertainty in the bias level. The mean of the Gaussian distribution is of course the bias offset level, and the standard deviation is related to the readout noise as

$$\sigma = \frac{\text{readout noise}}{\text{gain}}. \tag{4.1}$$

Inserting the readout noise and gain values from section 2.2.1, we would expect a standard deviation in bias values of 2.18ADU from a single bias

frame. If the bias is an average of N independent bias frames, then the uncertainty is the standard error of the mean,

$$SEM = \frac{\sigma}{\sqrt{N}}. \tag{4.2}$$

The CCD in the Earthshine Telescope has a non-negligible 2D-structure in its bias, and this influences the distribution of bias values. The blue histogram in figure 4.4 shows the distribution of bias values in the average bias from 120 bias frames obtained on JD 2455481, and it is definitely not a perfect bell-shape. By subtracting a (third degree) surface fit (in an attempt to remove the fixed pattern), the situation improves much, and the resulting red histogram is a near-Gaussian shape. Because the spatial standard deviation is composed of both random fluctuations and the 2D-structure, it is not a good indicator of the uncertainty in bias level.

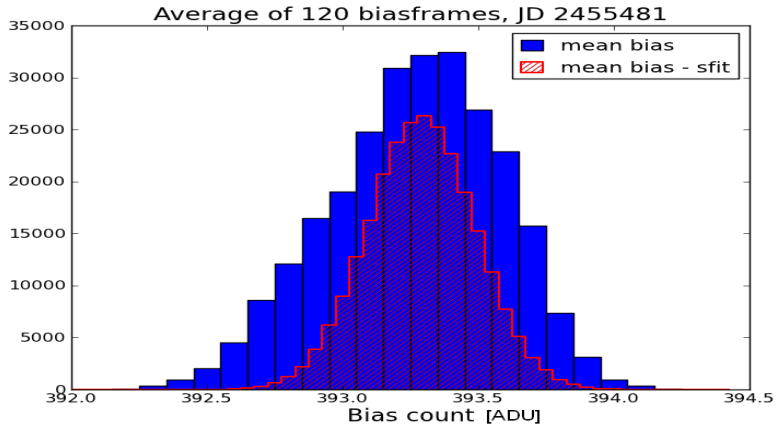

Figure 4.4: A histogram of an average bias frame is not a perfect Gaussian shape since the spread in values is due to 2D-structure as well as random fluctuations. This means the spatial standard deviation of an average bias frame is not a good estimate of the uncertainty in bias level.

4.2.1 Temporal standard deviation

Another approach is to look at the standard deviation of the distribution of bias values of a specific pixel in many different bias frames. I will call this the temporal standard deviation, σ_{time}. The temporal standard deviation can only be dependent on readout noise. Therefore, σ_{time} is an estimate of the uncertainty in the bias value of the pixel in question. Figure 4.2 is an example of exactly such a distribution, and the histogram of the bias values has the expected Gaussian shape. In order to estimate the error on the superbias, I created an array with the standard deviation of the half-median bias values, pixel-by-pixel (see superbias.pro in appendix B.1).

Figure 4.5 is a surface plot of the temporal standard deviation array described above. I have applied a 3x3 pixels median filter in order to

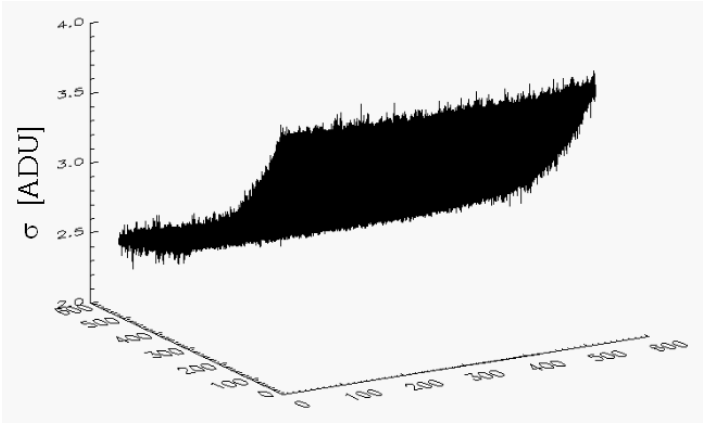

Figure 4.5: Surface plot of σ_{time}, the pixel-by-pixel standard deviation of the half-median bias values used in the super-bias. The array has been smoothed with a 3x3 pixels median filter.

remove a few extreme outliers. The mean of this σ_{time} array is 2.94ADU and this is an estimate of the uncertainty in bias per pixel. The relative error in bias is thus 0.74% for a single pixel. The uncertainty in bias, ΔB is the standard error of the mean from eq. (4.2),

$$\Delta B = \frac{2.94\text{ADU}}{\sqrt{1104}} = 0.088\text{ADU}. \tag{4.3}$$

4.2.2 Accumulated Readout Noise

An interesting feature of the σ_{time} array in figure 4.5 is that the standard deviations have an obvious gradient across the CCD. This gradient is due to accumulated readout noise. When a CCD is read out, all rows are shifted simultaneously so that a single row enters the output register, where each pixel is shifted within the register allowing one pixel at a time to be read out by A/D-converting the pixels' stored charge to produce a digital number. This process is repeated until the entire pixel frame has been read out. The charge collected in the last pixel to be read out has to be transferred $512 \cdot 512 = 262,144$ times. It is therefore not surprising that readout noise can accumulate. The profiles of the σ_{time} array are shown in figure 4.6. The dimension with the largest gradient corresponds to the rows being shifted, and the dimension with the smaller but still noticable gradient corresponds to the pixels being shifted.

4.3 Periodic Bias Level

Bias frames are expected to be stable from night to night and image to image. If not, then the readout electronics have a major flaw. I have tested the bias stability with long series of bias (and dark) exposures and plotted the mean bias level as function of time since first frame. There is no large

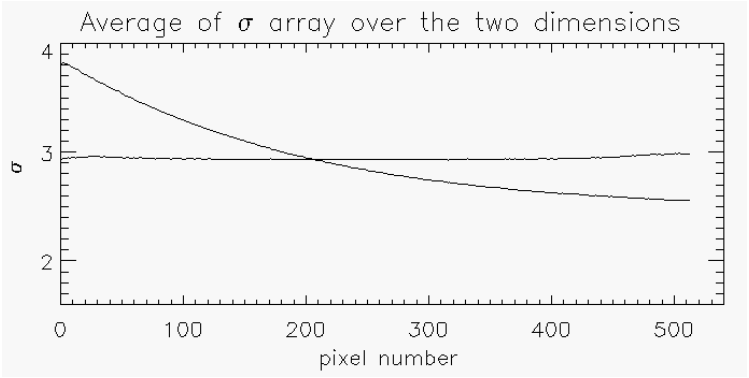

Figure 4.6: The profiles of the σ_{time} array from figure 4.5. The gradients are due to accumulated readout noise.

variability in the bias level, but it has a periodic behaviour. The period is just above 20 minutes and the peak-to-peak amplitude is about 0.5ADU.

The periodic behaviour of the mean bias level is stable once the camera has been on for about 10 minutes. The bias level has the same period and amplitude for bias frames and for dark frames with different exposure times. The relatively long period means it is unlikely the behaviour has anything to do with the electronics in the readout process. Instead we believe, the reason for the periodicity is the cooling system of the camera. The camera is equipped with a thermoelectric cooling system keeping the sensor temperature at a specified low value of $-80°F = -62.2°C$. In practice it is of course not possible to keep the temperature at the exact same temperature at all times. The temperature is slowly oscillating between the allowed maximum and minimum values, and this directly influences the bias level.

We have no way of splitting the camera apart to insert a thermometer to check the theory of an oscillating CCD temperature, but there are indications that it is the correct explanation. First of all, when we turn on the camera and the cooler and start shooting bias frames, we see how the bias level starts with high values and subsequently decreases and stabilises in its periodic behaviour within 0.5ADU of the superbias level. It takes about 10 minutes for the bias level to stabilize which corresponds well with the expected time for the cooling of the camera.

If the temperature of the CCD is indeed responsible for the periodic behaviour, then you would expect the gradual changes in the bias level to happen simultaneously over the whole area of the CCD. I have investigated this in some detail, not only to strengthen the temperature theory, but also because it means we can easily compensate for the periodicity in the image reduction.

I have checked the behaviour of the mean bias value in five different areas of the CCD for a set of dark frames lasting a total of 90 minutes. Each dark frame was exposed for 60 seconds, but as mentioned earlier, the exposure time doesn't affect the period. The mean bias value of each of the five small areas of the CCD was plotted together with the mean bias

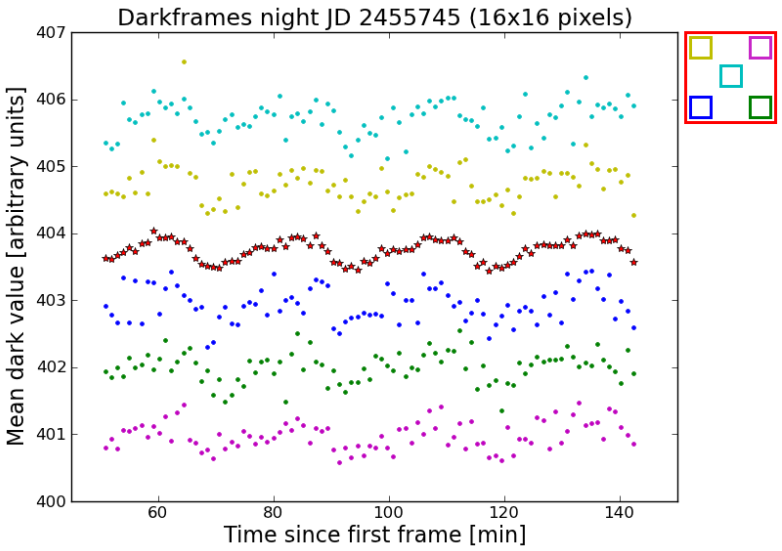

Figure 4.7: The bias level has a period of a bit more than 20 minutes and a peak-to-peak amplitude of 0.5ADU. Different areas of the CCD exhibit the same periodic behavior as the whole CCD frame (red stars). The smaller areas investigated are 16x16 pixels and their locations on the CCD are indicated by the coloured rectangles in the top right corner.

level, obtained from the full area of the CCD. The selected areas represent the four corners of the CCD (1 pixel away from the edge) and the center of the CCD.

I found that each area has its own mean level, but the same period and amplitude as the mean bias of the whole CCD. From this I conclude it is safe to assume the periodic behaviour is a shift in the bias level of the whole CCD area, and that it very likely has to do with the temperature of the CCD.

I have tried this procedure for two different area sizes, 8x8 pixels and 16x16 pixels. The periodic behaviour can be seen in both cases, but it is easier discernible for the larger area size. Figure 4.7 shows the mean bias values for all five areas in the case of 16x16 pixels as well as the bias level of the whole CCD. I have added different offset values to each of the datasets to separate them from each other.

The consequence of the periodic bias level is that we risk introducing an error of 0.5ADU, when we subtract the superbias from a science frame as the first step in data reduction. The solution is to scale the superbias with the average bias level from a couple of bias frames taken before and after the science frame.

Typically we observe a stack of images with a bias frame on either side, within less than a minute. The maximal error we can introduce with

a difference of one minute between the two bias frames is

$$\text{Max Error} = 1\text{min} \cdot \frac{0.5\text{ADU}}{20\text{min}} = 0.025\text{ADU}, \tag{4.4}$$

corresponding to about 0.006% of the bias level.

No correction for the periodicity of the bias was made in the construction of the superbias. As a result, the scatter in the distribution of bias values in a single pixel is expected to be larger than simply the readout noise. This is exactly what I have found. In section 4.2.1 I experimentally determined the uncertainty in bias level in a single pixel to be 2.94ADU, which is indeed larger than the 2.18ADU I predicted on page 38 from the readout noise provided by McVarnock [2010].

4.4 Dark Current

According to the camera performance sheet [McVarnock, 2010] the dark current is

$$0.0002\, e^- / \text{pixel}/s$$

when the camera cooling is in use and has stabilized. This is a very low value, and for the relevant exposure times the dark current is expected to be negligible. I have checked this for a series of dark frames that I obtained on JD 2455883 with exposure times in the range 10 to 200 seconds. The average count of the dark frames (closed shutter exposures) as function of the exposure time can be seen in the left part of figure 4.8.

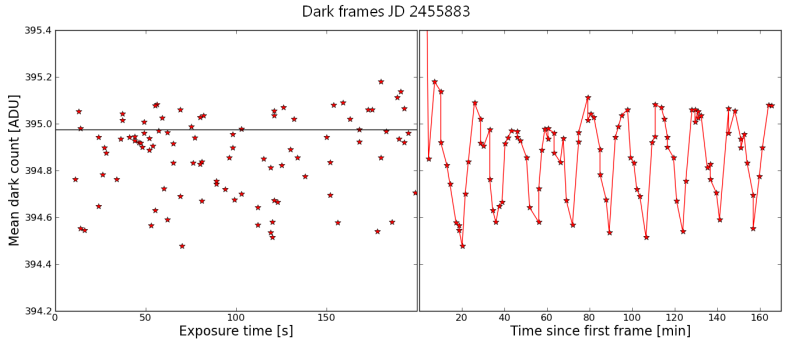

Figure 4.8: **Left:** Mean dark count as function of exposure times chosen randomly in the interval 10-200 seconds. No dark current is seen for these exposure times. The white horizontal line is the mean bias level in the superbias. **Right:** Mean dark count as function of time since first frame. It can be seen that the scatter in the left image is due to the usual 20 minutes period in bias level.

No dark current can be seen. A simple linear regression of the mean dark count as function of exposure time, yielded a coefficient of determination of $r^2 = 0.01$. In other words, there is no statistically significant

linear relationship between the dark level and exposure times up till at least 200 seconds.

The dark level remains constant at values within ± 0.5 counts from the mean level of the superbias. The scatter is due to the periodicity in the bias level described in section 4.3. The right part of figure 4.8 shows the same dark frames plotted with their average count plotted as function of time. The twenty minutes period is clearly seen.

The confirmation that dark current is negligible for the exposure times of interest is valuable information. It means that we can make use of bias frames instead of dark frames. The periodic behaviour of the bias level still forces us to obtain bias frames on each side of a flatfield or science frame, but at least it is only necessary to do a bias frame (that has minimal exposure time), rather than a dark frame with the same exposure time as the science frame. Thus, we are saving valuable time for observations.

4.5 Readout Noise & Gain

The readout noise (RON) and the gain of a camera can be determined experimentally from a photon transfer curve. The photon transfer curve gives the relation between signal strength, S, and the variance, σ^2, in the pixel values. It is assumed that the only sources of noise are photon noise and readout noise. Photon noise (a consequence of the quantum nature of light) is the square root of the number of electrons, so using the gain, g, as a conversion factor, the photon noise in ADU is

$$\text{Photon noise} = \frac{\sqrt{S * g}}{g} = \sqrt{\frac{S}{g}}. \tag{4.5}$$

The total noise and the variance is then

$$\sigma = \sqrt{\frac{S}{g}} + \frac{\text{RON}}{g} \quad \Rightarrow \quad \sigma^2 = \frac{S}{g} + \left(\frac{\text{RON}}{g}\right)^2. \tag{4.6}$$

Given the photon transfer curve, the gain and the readout noise can thus be determined from a linear regression, $\sigma^2 = aS + b$.

$$g = \frac{1}{a} \quad , \quad \text{RON} = \frac{\sqrt{b}}{a}. \tag{4.7}$$

The photon transfer curve can be measured with a series of exposures, where the CCD is illuminated uniformly, with increasing exposure times ranging between no exposure and saturation of the CCD. Essentially you need flatfields at many different exposure levels, and bias frames for the zero exposure. The presence of a fixed pattern in bias and flatfield will add to the noise. A quick way to get rid of the fixed pattern is to obtain pairs of images at each exposure level and subtract one from the other, keeping in mind that the subtraction doubles the variance. For a given exposure level, we therefore have

$$\sigma_{F_1 - F_2} = \sqrt{2\sigma_F^2}. \tag{4.8}$$

Here, I will only make a quick estimate using a couple of flatfields and a couple of bias frames. In order to achieve the full yield of the photon transfer curve, you want the camera to be calibrated so that the FWC and the A/D-saturation level are identical, and then make careful measurements of a stable, monochromatic light source[2] with small increments of the full A/D-scale.

I found in section 4.3 that the uncertainty in bias per pixel estimated as the temporal standard deviation was larger than the value given in the camera manual for the readout noise. I explained this as a consequence of the periodic bias level, but it is of course also possible that the manual value is wrong. I can make an independent check from sets of bias frames obtained close to each other in time, so that the only noise in the bias frame is readout noise. As we have seen, our bias has a fixed pattern, and therefore the readout noise is estimated from the standard deviation of the difference of the two bias frames

$$\mathrm{RON} = \frac{g * \sigma_{B_1 - B_2}}{\sqrt{2}}. \tag{4.9}$$

The gain is estimated as the inverse of the average signal of a pair of flatfields divided with the variance in flatfield at this exposure level. The flatfields are of course corrected for bias, and the equation becomes

$$g = \frac{(|F_1| + |F_2|) - (|B_1| + |B_2|)}{\sigma^2_{F_1 - F_2} - \sigma^2_{B_1 - B_2}}. \tag{4.10}$$

I have calculated both the gain and the RON for a number of different flatfield sessions. Some examples are listed in table 4.1. The two flatfields used in any given example were chosen to be of the same type, have the same filter combination and exposure time. All bias frames and flatfields were checked visually and discarded if they looked different from what I have come to expect.

In general the experimental values for the gain and the RON are very close to those stated by the manufacturer [McVarnock, 2010]

$$g = 3.8\frac{e^-}{\mathrm{ADU}} \quad , \quad \mathrm{RON} = 8.3\frac{e^-}{s}, \tag{4.11}$$

and it seems likely that repeating the experiment for many more examples would lead to similar average values. If the temporal standard deviation was a good estimate of the readout noise, then the readout noise would be $2.94\mathrm{ADU} \cdot 3.8e^-/\mathrm{ADU} \approx 11e^-$, which is not only inconsistent with the manual, but also with the experimental values in table 4.1.

The B domeflat example has a slightly higher RON than the others. This set of bias frames were really dark frames with an exposure time of $150s$. Since our camera has very low dark current, the mean level is the same as is expected for a bias frame (~ 395). However, visual inspection of the two dark frames in question showed a few bright pixels located at different positions in the two frames - cosmic ray hits. The chance of

[2]It is preferable with a monochromatic light source, since you are not interested in the wavelength dependence of the quantum efficiency of the pixels.

JD	colour filter	density filter	flatfield type	gain	RON
2455767	IRCUT		dome	4.00	8.54
2455825	B		dusk	3.59	7.69
2455827	VE1		dusk	3.86	8.28
2455832	B		dome	3.79	9.64
2455863	B	ND0.9	lamp	3.68	7.91
2455865	V		lamp	3.96	8.45

Table 4.1: Experimental values of the gain and the readout noise for examples from different flatfield sessions.

cosmic ray hits increases with exposure time. Since the bright pixels have different positions in the two frames, they will also show up in the difference frame. Therefore $\sigma_{B_1-B_2}$ is larger in this example, and the calculated RON becomes larger as a result. The gain is less affected because $\sigma^2_{F_1-F_2}$ dominates over $\sigma^2_{B_1-B_2}$.

Experimental determination of RON and gain should be done a few times a year to test stability and performance of the camera. Precise values are furthermore necessary if you need to compare your science results with those obtained from other telescopes.

4.6 Summary

The dark current of the camera is negligible for the relevant exposure times, and therefore we do not have to obtain dark frames, but can settle for the less time-consuming bias frames. The details of the 2D-structure in the bias are captured with pixel by pixel subtraction of a superbias, constructed as a mean-half-median of 1104 bias frames. The superbias has a bias level of

$$B \pm \Delta B = 394.975 \pm 0.088\text{ADU}.$$

I have estimated the uncertainty of the bias in a single pixel as the average temporal standard deviation of a pixel. I found this to be 2.94ADU.

The discovery of a twenty minute period in the bias level has led to the decision to scale the superbias with a pair of bias frames taken before and after the science frame. Sets of observations, sandwiched between bias frames, are obtained within less than a minute. Thereby the possible systematic error from the periodic behaviour is a maximal 0.006% of the bias level. The period is believed to be related to small temperature oscillations within the CCD.

Observations of sets of bias frames and flatfields can be used to obtain crude estimates of the readout noise and gain of the camera. I found values that are consistent with the values provided by the manufacturer.

Chapter 5

Flatfields

A flatfield is an image obtained with the entire telescope system of a uniform light source. Any deviations from uniformity in the flatfield image (after bias subtraction) maps the combined effect of variations in quantum efficiency of individual pixels and irregularities across the telescope's field of view that are intrinsic to the telescope. Therefore you can correct for these effects by dividing an object frame with a flatfield. The flatfield should be normalized, because the pixel-to-pixel variations in sensitivity depend on exposure level. Also, both the object frame and the flatfield must be bias subtracted prior to the flatfield correction. The flatfield may change over time due to eg. accumulating dust and bad pixels, and the norm is to obtain flatfields every day.

The principle in flatfielding is simple enough, but it is challenging to achieve uniform illumination of the CCD with a sufficiently high precision. A complicating factor is that the flatfield is wavelength dependent because quantum efficiency is wavelength dependent. It is therefore important to make flatfields in all relevant colour filters. Also, there may be dust on the colour filters. The perfect flatfield target is not only a uniform light source, but also has the same spectral distribution as the astronomical object of interest - in our case the Moon.

In section 5.1, I introduce the different types of flatfields that have been tested on the Earthshine Telescope. In section 5.2, I explain the construction of the master flatfields that are used in the image reduction and I describe the master flatfields and their structure, and in section 5.3, I look at how the flatfields change over time, as this will allow me to estimate the error introduced from flatfield division to the intensity of earthshine and moonlight. Section 5.4 is a discussion of the performance of the different types, and how different they are from each other.

5.1 Different Types of Flatfields

5.1.1 Twilight Flatfields

At dusk and dawn the sky is approximately uniform near zenith, and the twilight sky is therefore often used as a flatfield target. The twilight sky

has a high illumination level, allowing for high S/N in the flatfields.

The surface brightness of the twilight sky changes rapidly, and the time interval where the sky is uniform and is neither too bright nor too dark is in the order of minutes. Tyson and Gal [1993] provide a method for efficiently computing an appropriate sequence of exposure times during a twilight flatfield session[1]. You want at least three good flatfields in each filter, so that star trails can be removed by median combining the flatfields.

The biggest disadvantage of twilight flatfields is that they need to be obtained at very specific times in a very short time-interval. The Earthshine Telescope is still in its test-phase, and for example the future-planned automatic weather station is not in operation yet. This rules out the possibility of automatic twilight flatfield sessions at the current time.

5.1.2 Dome Flatfields

Dome flatfields are generally obtained by imaging a screen inside the dome. The illumination level can in principle be controlled and the light source chosen to have an appropriate spectral range. However, in practice it is very difficult to achieve uniform illumination of the screen. In our case, we have no special flatfield screen in the dome, but we have imaged the inside of the dome with the dome light on. These dome-flats have large gradients, and very long exposure times were necessary for the B-filter and the VE2-filter, a result of the combination of the colour of the lamp and the absorbing properties of the paint on the dome. Dome flatfields were used as back-up to the twilight flatfields before the hohlraum sphere (lamp flatfields) was in operation.

5.1.3 Lamp Flatfields

Inside the dome there is a hohlraum sphere (sometimes called an integrating sphere) that functions as a near-uniform light source. It is a hollow sphere with an internal lamp and walls that are in radiative equilibrium with the radiant energy within it. The telescope can be positioned so that it points to an opening in the sphere (the hohlraum sphere can be seen in figure 5.1). I will call flatfields obtained with the hohlraum sphere for lamp flatfields. The advantage of lamp flatfields is that they can be obtained at any time, and that they have high signal to noise.

5.1.4 Moon Flatfields

Images of the sunlit Moon can be used to determine the flatfield. The idea is to take many images of eg. the full Moon in such a way that the entire CCD is covered and that two Moon images are never exactly on top of each other. This is called dither observations. Each pixel of the CCD is covered by a different portion of the Moon in each image. On the other hand, the images all have the flatfield in common. It is therefore possible to calculate

[1] Flatfields must be obtained for all optical configurations that are to be used in the given night's observations. With the limited time during "astronomical twilight", this is a special challenge with five colour filters and potentially four different operational modes.

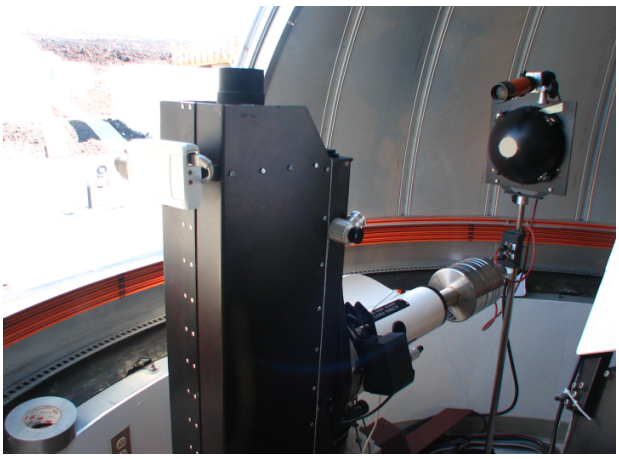

Figure 5.1: The Earthshine Telescope in zenith position. The hohlraum-sphere is the black sphere in the top right corner. The telescope can be positioned to look through the hole in the sphere. When the sphere is turned on it, is filled with a diffuse light.

the flatfield from the images (the technique has been developed for solar observations [Chae, 2004, Kuhn et al., 1991]).

When the flatfields are calculated from observations of the object of interest, the spectral distribution is automatically the appropriate one. It is worth mentioning that the earthshine has a different spectral distribution than moonlight [Very, 1913], but this difference is small compared to the spectral difference from the twilight sky. Another advantage is that since the flatfield is calculated, we are no longer concerned with the uniformity of the light source.

The signal to noise of Moon flatfields is often excellent, but this kind of flatfield is time-consuming to generate. Time is not an issue, when the Earthshine is too faint for Co-add mode, that is from half Moon to full Moon, so these phases could be used to obtain flatfields. Unfortunately, it will not be possible to use the earthshine relevant phases to calculate flatfields. At phases around the new Moon, the Moon is close to the horizon, and the observation time is limited. All Moon observations are therefore used to extract earthshine intensities, and for this purpose we need the Moon to be centered in the images, rendering them useless for flatfield calculation.

It would be interesting to investigate the possibility of combining Moon flatfields from around the full Moon with daily twilight or lamp flatfields. The Moon flatfields could provide information about the low frequency patterns such as a possible gradient in the flatfield, and the lamp or twilight flatfields could provide information about high frequency patterns that are more likely to change on short time-scales, such as dust and bad pixels.

The challenge with Moon flatfields is that it is necessary to know the exact location on the CCD of the Moon image. We need a very precise

routine for edge detection, or something similar. This is related to the ability to align the images - a subject I have written about in chapter 7. At the present time, Moon flatfields are not a good option, but with improved alignment techniques currently under development, they may become an important part of the flatfield routines for the telescope.

5.2 Master Flatfield

For a given Julian date we will need a master flatfield for each filter that we can use for the image reduction of all the science frames from that night. I have written an IDL program that creates one master flat for each filter for the night in question. The code for this program, masterflat.pro, is in appendix C.1.

Each flatfield for a specific night, filter and type is bias subtracted using the scaled superbias, has a surface-fit subtracted[2], and is then normalized. The flatfields are then combined to one master flatfield using the pixel-based mean-half-median method that was also used to construct the superbias (see 4.1.2).

Examples of sections of twilight master flatfields for each colour filter are displayed in figure 5.2. The full master flatfields can be seen in appendix C.2. The analysis in sections 5.2.1 and 5.2.2 is based on twilight master flatfields, but the four different types of flatfields have the described structures in common.

5.2.1 Structures in Master Flatfields

There are several noteworthy effects in the master flatfields. Common for all flatfields is the presence of dust seen as large, dark circles, and small dark specks caused by bad pixels (see figure 5.3). Another common feature is the thin horizontal and vertical lines. These are very likely due to differing pixel sizes - a result of the grid used in the production of the CCD. This pattern is static, and is therefore removed without any trouble from the science frames when flatfield correcting.

The flatfields in all five filters have the same low frequency diagonal pattern, although this pattern is hardly discernible in the VE2 filter. The most notable feature is the bright and broad diagonal lines at an angle of +45 degrees from vertical. If one takes a closer look, the same structures are visible in the VE2 filter, but this filter has an overlaying interference pattern that is roughly oppositely oriented. The bright diagonal lines are strongest in the B-filter where they have values that are about 1% higher than the mean value of 1 ADU, and weakest in the VE2-filter, where they are only 0.2% higher. The strength of the bright diagonal lines is listed for all filters in appendix table C.1 together with the standard deviation of the master flatfield.

The diagonal structures are clearly wavelength dependent, and they are strongest in the blue part of the spectrum. The most likely explanation is varying CCD thickness. Our CCD is back-side illuminated, which means

[2]It is necessary to subtract a surface fit from twilight flatfields, but it can be argued that this should not be done for lamp flatfields. See section 5.4.2.

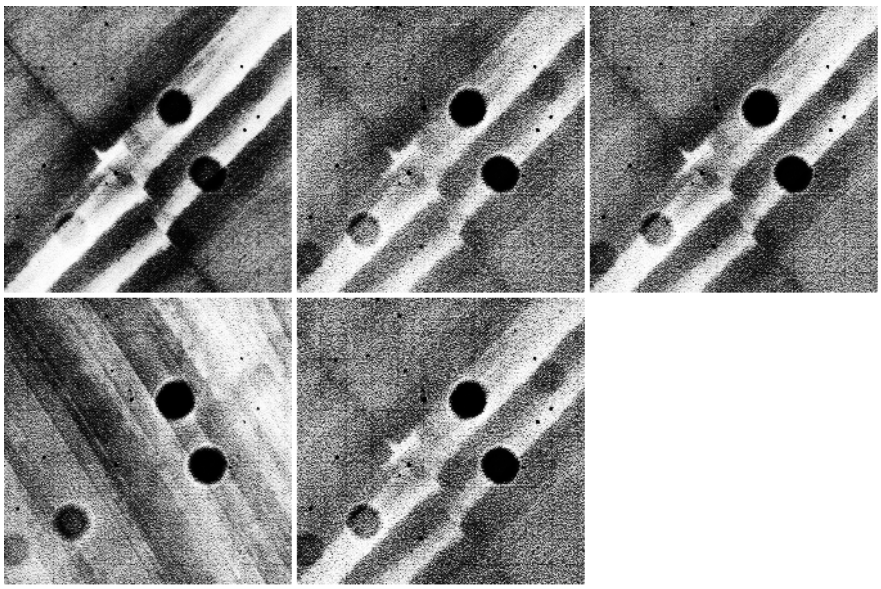

Figure 5.2: Sections of twilight master flatfields obtained in a dusk-session JD 2455827. The images here are histogram equalized and show the central 20% of the full flatfields. The full flatfields can be seen in appendix figures C.1-C.5. From top left to bottom right the filters are: B, IRCUT, VE1, VE2, V. Flatfields from all filters show a considerable amount of structure, some of which is static and can be completely removed from object images. Parts of the structure changes slightly over time and therefore introduces an error in the image-reduction.

the silicon wafer has been thinned to about $15\mu m$. The advantage of such a thinned CCD is an overall higher quantum efficiency, and especially an improved short wavelength response. A common disadvantage with back-side illuminated CCDs is that the thinning is non-uniform and this non-uniformity shows up in the flatfields [Howell, 2000]. It is very likely this effect that we see as a diagonal pattern in all the master flatfields. Flatfields are wavelength dependent because the mean free path of a photon inside the silicon is strongly dependent on wavelength (I elaborate on this in appendix C.2.1).

Structures in a flatfield are unproblematic, as long as they are constant over time for a specific filter. In that case they are removed completely from the object frame when it is flatfield corrected. This is the case for bad pixels (with a few exceptions) as well as vertical and horisontal lines due to differing pixel sizes. The diagonal pattern on the other hand may vary slightly in time due to eg. temperature variations in the CCD. Dust-specks may also shift their positions slightly. This can be a result of the dust moving, but we have also experienced a miniscule rotation of the camera with respect to the telescope, causing the whole flatfield to be rotated. The

stability of the flatfields is discussed in section 5.3.

Bad Pixels

Bad pixels are defined as those having properties significantly different from their local neighbourhood mean in the individual masterflat. Our CCD has a number of bad pixels with sensitivities much lower than average. They are a result of imperfect manufactoring, and most of them are collected in small groups. Bad pixels are fairly common in CCDs, and are generally not considered to be a problem. Their numbers and locations are stable, and almost all of them are completely removed with even a mediocre flatfield. But the most severe of the bad pixels seem to have different strength in different master flatfields, and therefore they show up in diminished form in difference images between two master flatfields (more on this in section 5.3.2). This indicates that a few of the bad pixels may not be completely removed when flatfielding an object image, and therefore they will increase the error on the earthshine or moonlight intensity in that pixel.

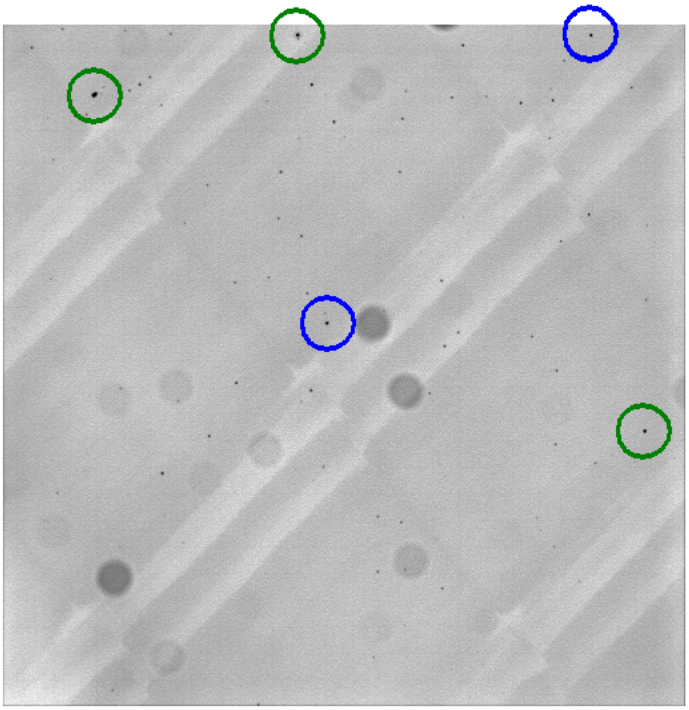

Figure 5.3: IRCUT master flatfield from session JD 2455827, shown in powerscale to emphasize the dark specks that are the bad pixels. The three most severe groups of bad pixels are circled in green, and the two second worst ones are circled in blue. We cannot completely remove the effect of the most severe bad pixels from an object image.

Figure 5.3 is the master flatfield in the IRCUT filter from twilight session JD 2455827 shown on a power-scale to emphasize the bad pixels that are seen as small dark specks. There are quite many individual and pairs of bad pixels, but it is only the more severe groups of bad pixels that we need concern ourselves with. The three primary bad pixels are circled in green, and the two secondary ones are circled in blue. These five bad pixels are the ones we may not be able to remove completely from an object image by dividing with a flatfield. Luckily, most of them are located close to the edge of the CCD, where we rarely place an object of interest. There is one semi-severe group in the central part of the CCD. In section 5.3.2, I estimate the type of uncertainty we may expect from imperfect bad pixel removal.

The ten most severe groups of bad pixels are listed in table C.2 in appendix C.1. They consist of 23 bad pixels that all have values in the IRCUT master flatfield lower than 10% of the mean. For comparison the master has a mean count of 1 ± 0.0048ADU.

Dust

The relatively large dark circles in the flatfields are out of focus dustmotes. They appear as discs rather than doughnuts because the Earthshine Telescope is a refracting unobstructed telescope rather than a reflecting telescope [Newberry, 1996]. The size of the dust shadows is a result of the distance to the dust from the surface of the CCD. The distance can be calculated as the diameter of the shadow times the focal ratio of the telescope. With pixel size $16\mu m$, $f/12.5$, and shadow discs about 30 pixels in diameter, the distance is

$$\text{Distance} = \frac{16\mu m \cdot 12.5 \cdot 30}{1000} = 6mm. \tag{5.1}$$

This tells me the dust must be located on the dewar window. The dewar window is a protective piece of glass covering the CCD. The darkness of the dust shadows is a measure of the size of the dust particle.

Dust may accumulate over time, but the Earthshine Telescope is tightly sealed, and it is not expected to be a big problem. No dust seems to have accumulated in the time since the telescope was installed on Mauna Loa in the spring 2011. Figure 5.10 displays four flatfields with the earliest being from September 2011 and the latest from March 2012. They have the exact same number of dust shadows, even if some of them are difficult to see in all the flatfields. It is possible that the telescope has dust on other surfaces than the dewar window, but if this is the case they are at a distance from the CCD so that they do not show up as distinct features in the flatfield. For example, dust located on the colour filters will have a diameter in the image plane of about 18% of the size of the CCD. The edges are too washed out to be distinct, but dust on the colour filters will still affect the flatfield.

5.2.2 Histograms

A histogram of a perfect, normalized master flatfield should produce a Gaussian distribution with its width related to the gain of the detector and

the readout noise. Since the flatfields are well-exposed, and our readout noise is low (see section 2.2.1), it is safe to assume that the readout noise is negligible compared to the Poisson noise of the photons in the flatfield (photon noise, see eq. (4.5)). The width in units of ADU is therefore

$$\sigma_{\mathrm{ADU}} = \sqrt{\frac{|F|}{\mathrm{gain}}}, \tag{5.2}$$

where $|F|$ is the mean level in the flatfield. Of course the perfect flatfield doesn't exist, and histograms of real flatfields are expected to have a tail extending to lower values. This tail is a result of dust in the optics that lowers some of the pixel values.

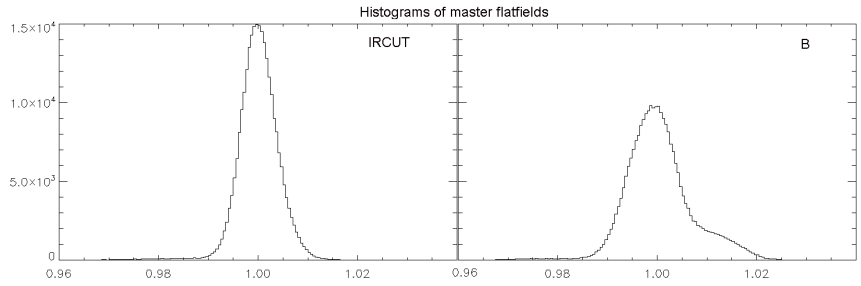

Figure 5.4: Histograms of the twilight master flatfields obtained from dusk-session JD2455827 in the IRCUT-filter **(left)** and the B-filter **(right)**. The shape of the IRCUT histogram (representative of the V-, VE1- and VE2-filter as well) is a rough Gaussian with a low-end tail due to dust. The B-filter histogram has an additional shoulder of high values.

Figure 5.4 shows two examples of histograms of dusk master flatfields from night JD2455827. The one on the left is from the master in the IRCUT-filter and the one on the right is from the B-filter. The IRCUT histogram has the expected shape of a rough Gaussian with a low-end tail. This shape was also found in the cases of the filters V, VE1 and VE2. The B-filter has the same shape, but on top of that it has a shoulder extending to higher values. This shoulder is a bit unusual, and it appears in general in histograms of the B-filter master flatfields.

In section 5.2.1 I found that the bright diagonal lines are stronger in the B-filter than for the other filters. It could be that the structure for this filter is strong enough to show up in the histogram. I have plotted the positions of the pixels responsible for the shoulder in figure 5.5 together with the full image of the B-filter master for comparison. The shoulder pixels are defined to be those with a value higher than 0.01ADU. The shoulder pixels are clearly seen to coincide with the familiar diagonal pattern in the flatfields.

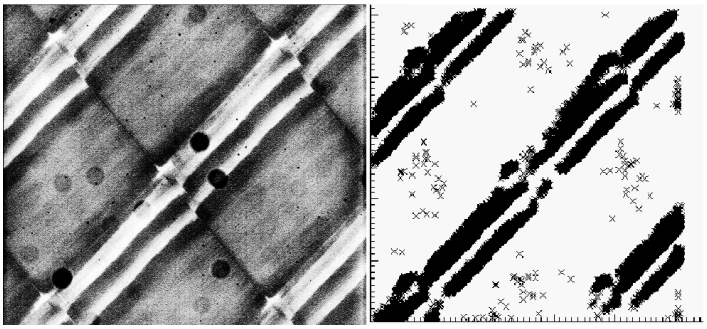

Figure 5.5: B-filter, JD2455827. In the righthand figure the positions of the shoulder pixels (in figure 5.4), defined to have values higher than 1.01ADU, have been marked. For comparison the lefthand figure shows the B-filter master flatfield. The bright diagonal pattern is responsible for the high-end shoulder seen in the B-filter histogram.

5.3 Stability of Flatfields

The flatfield of a CCD can change slightly over time. This can be due to a miniscule change in the optical setup that the observer may not notice: The filter wheel positions the filters a small fraction of a degree differently than earlier, or the CCD camera has shifted its position by a similar small amount. Also, dust accumulates over time, and dust already present may change position. There may also be changes in the pixels of the CCD: The pixel properties, such as FWC and quantum efficiency can be affected by repeatedly being subject to over-exposure, cosmic-ray hits and simply by time. All these possible causes of changes in flatfield mean it is important to flatfield correctly with a recent flatfield.

In this section I will investigate the stability of the twilight flatfields on two different time scales. It would be problematic if the flatfield exhibits large variations over short time scales, since the uncertainty in flatfield adds to the uncertainty of the science observations.

5.3.1 Flatfields From the Same Session

A typical night of observation may start with a flatfield session at dusk, and then Moon observations as soon as the Moon rises. We need to know if there are any significant changes in the flatfield during this time, that would introduce an error in image reduction. In particular I am interested to see if prominent structures, such as the diagonal bright pattern etc., have fast variations.

Examples of percent difference images between pairs of flatfields are given in figure 5.6 for session JD 2455827 and in appendix figure C.6 for session JD 2455831. One can immediately from a percent image see if the two flatfields deviate much from each other. Star trails may show up in difference images because more stars appear over time, and cosmic-ray

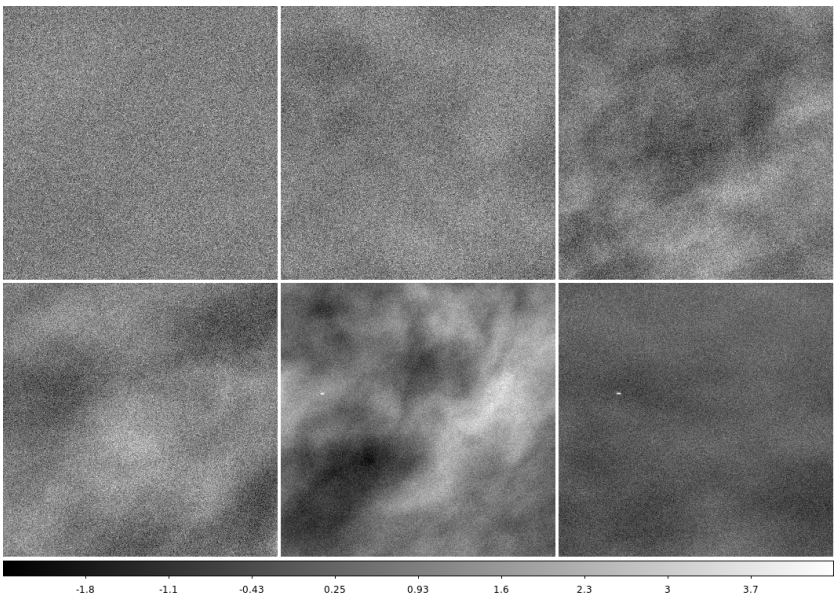

Figure 5.6: Percent difference images between flatfields from the same filter and same session (JD 2455827). **Top:** B-filter Δt 6.6min, V-filter Δt 13.7min, IRCUT-filter Δt 0.4min. **Bottom:** VE1-filter Δt 6.5min, VE2-filter Δt 15.0min, Δt VE2-filter 8.3min. None of the filters show any remnants of the structures described in section 5.2.1. It seems that for short timescales we can assume the structures to be stable. The B-filter percent image is exactly what you can hope for: Small percent differences with a random (Gaussian) distribution. The other filters also have low percent differences but with a less random distribution. The VE2-filter image with $\Delta t = 15$min is clearly worse than the others. A reason could be that the early flatfield is poorly exposed with a low average count of $11,000$ADU. The bright streak seen in both the VE2 percent images is a star-trail present in the late VE2 flatfield they have in common. **The scale:** The numbers on the scale expresses the difference between pairs of images as a percentage of the earlier image.

hits may also be seen. Both effects are unproblematic, because they are removed with the median filter in the construction of the master flatfield.

The structures that we see in individual flatfields as well as master flatfields do not show up in difference images of flatfields from the same session. In other words, the structures are stable at least for short timescales, and we can therefore expect that the structures are of no consequence in the image reduction of Moon images, as long as the flatfields are obtained close in time to the Moon images.

In general the individual flatfields that are used to construct a master flatfield are very similar. The percent difference image for a well-exposed pair of flatfields typically has a standard deviation $\leq 0.7\%$, the flatfield pairs have correlation coefficient ≥ 0.5 (see appendix tables C.5 and C.4). It is important that the flatfields are well exposed - that they have a high signal to noise ratio. Flatfield pairs where one or both of the flatfields have low counts $(10,000 - 13,000)$ADU have a tendency to correlate less strongly or not at all compared to flatfield pairs where both flatfields have higher counts (above $18,000$). Flatfields with counts less than perhaps $15,000$ADU should be discarded before constructing a master flatfield. The best flatfields are exposed to near-saturation.

5.3.2 Night-To-Night Comparison

The analysis in section 5.3.1 dealt with individual flatfields. However, it is not individual flatfields that are used in the image reduction. I will now investigate the stability of the master flatfields.

I compare two master flatfields by creating a percent difference image. I have done this for filter pairs of master flatfields obtained with a few days in between. This will give me an idea about both how they change over time and the error associated with the flatfields. It should be noted that the V-filter master flatfield from night JD 2455831 is constructed as an average of only two available flatfields, whereas the other master flatfields are mean-half-medians of typically five flatfields. The means of the percent images, as well as their standard deviations are listed in table C.6.

The master flatfields from the sessions JD 2455825, JD 2455827 and JD 2455831 are very similar, with standard deviations in the percent images below 0.25%. The exception is the V-filter, but that is to be expected, since one of the compared flatfields is not an acceptable master flatfield. Surface fits of the percent images have very small regression coefficients with the largest being of the order 10^{-7}, so I can be sure the standard deviation is not an expression of a gradient across the percent image.

The central 25% of the five percent images in this analysis of the stability of twilight master flatfields are shown in figure 5.7. The full percent images can be seen in appendix C.4.

Structure in the Percent Difference Images

The master flatfields I am comparing are indeed very similar. A visual inspection of a set of master flatfields shows the same number of dust-circles and apparently the same diagonal structure and bad pixels. But there are some differences between them that show up in the percent images. The

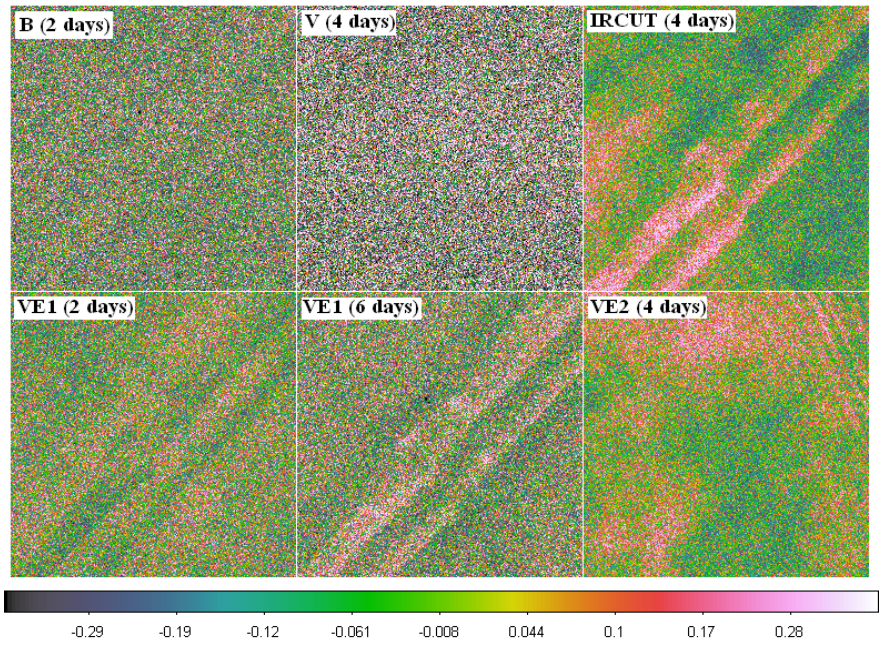

Figure 5.7: Percent difference images of filter-pairs of twilight master flatfields (central 25% histogram equalized, full images in appendix C.4). The diagonal structures have not cancelled out completely, and a few bad pixels are still visible. The dust seem to be completely gone. Any structure present in a difference image with only a few days between, cannot be expected to be removed perfectly from an object image by dividing with a recent master flatfield. **The scale:** The numbers on the scale expresses the difference between pairs of images as a percentage of the earlier image.

bright diagonal pattern can be seen in the B-filter percent image (2 days in between) as well as that of IRCUT (4 days) and both of the VE1-filter percent images (2 and 6 days in between). The VE2-filter percent image (4 days) shows the oppositely oriented diagonal pattern exclusive to that filter.

The percent difference between two master flatfields is often larger in the diagonal patterns than in the rest of the frame. The diagonal pattern (both the common one and VE2's) is up to 0.1% different in the two masters being compared. The B-filter is the only one, where the pattern is a little better behaved with a difference of only up to 0.05%. This is interesting, since the B-filter is the one with the strongest diagonal pattern to begin with.

Several of the bad pixels also show up in the percent images. It is the five groups of bad pixels that I circled in figure 5.3 that are causing trouble. The largest deviation in each bad pixel group is given in table 5.1 for each of the percent images. The worst pixels may be $6-7\%$ different from one

	(68,459)	(481,206)	(221,504)	(441,503)	(247,287)
B	-1.1%	-	-	-	-1.8%
VE1 (2)	4.4%	3.9%	2.8%	2.1%	-
VE1 (6)	-3.6%	-3.0%	-2.3%	-2.1%	-2.1%
IRCUT	-7.0%	-6.1%	-4.5%	-3.4%	-

Table 5.1: Percent differences between two master flatfields in the five most severe of the bad pixel groups (as specified in section 5.2.1 and appendix table C.2). The value given here is the largest percent difference found in the group in a given filter pair. The V and VE2 percent images do not show any signs of bad pixels.

master to the next, and therefore these pixels should be avoided. The four worst bad pixel groups are located near the edge of the CCD and should be easy to avoid, when analysing Moon images. The central bad pixel group with coordinates (247,287) might lead to an error in the flatfield in one or two pixels of $1-2\%$. Typically we will be interested in the intensity (earthshine or moonlight) of an area covering 10x10 pixels or more. It will therefore not matter too much if there is a slightly larger error in a couple of pixels.

There are no signs of the circular dust shadows in any of the percent images. It is obvious that no new dust has accumulated in the 6 days period. This is good news. We can hope that the telescope is well sealed and that new dust will only accumulate rarely. In flatfields from when the telescope was in Lund, we see much fewer dust circles than in flatfields obtained at Mauna Loa. Dust has accumulated during the journey and especially during the installation of the telescope. We can probably expect new dust whenever maintenance is performed on the telescope.

Not only is there no new dust on the dewar window, but the dust has apparently not moved within the six days period. This indicates that dust will not move between a moon-session and the corresponding flatfield session, and dust will therefore not influence the error on flatfield. It is expected that dust may move a little bit around over a longer time period, and this is one of the reasons why the master flatfield should be obtained relatively close in time to the moon-session.

In general, the more extreme pixels are simply more different from one master to the next, compared to an average well behaved pixel, and therefore they show up in the difference images. This means that certain pixels and areas of the CCD have a more uncertain flatfield than others.

5.3.3 Error on Master Flatfield in Boxes

The analysis in section 5.3.2 has given an indication of the kind of error we can expect on the master flatfield. As mentioned previously, the earthshine and moonlight intensities will often be determined as a mean of an area of perhaps size 10x10 or 30x30 pixels, and the Moon will typically be positioned in the central part of the CCD. I am therefore interested in how the mean flatfield value changes in smaller central areas from one master

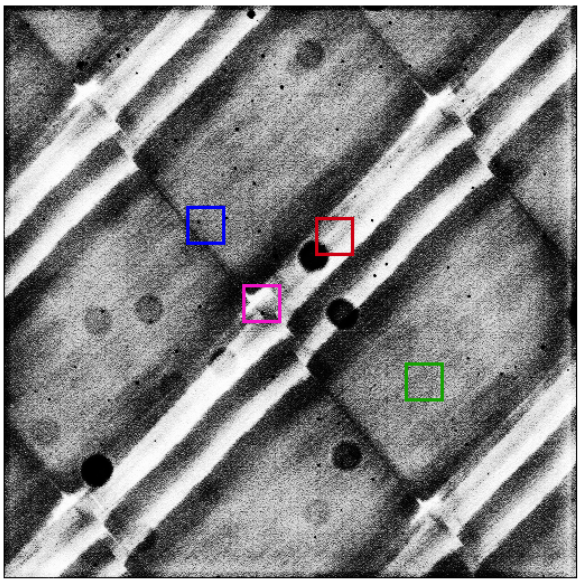

Figure 5.8: The selected 30x30 pixel areas under investigation. The background image is the B-filter master flatfield from JD 2455827.

	blue	red	pink	green
B	0.042	0.038	0.048	0.130
V	0.045	0.043	0.030	0.089
VE1	0.066	0.034	0.041	0.198
VE2	0.061	0.083	0.090	0.363
IRCUT	0.125	0.050	0.120	0.136

Table 5.2: The largest percent change in mean flatfield value of four central 30x30 pixel areas, determined from minimum three different master flatfields per filter.

flatfield to another. This will be an estimate of the error the flatfielding introduces in such areas.

I have compared four central 30x30 pixel areas in twilight master flatfields. A minimum of three masters were available in each filter[3]. The selected regions are shown in figure 5.8 on top of the B-master for session JD2455827. For each filter and region, I have checked the difference between the largest and smallest mean value, expressed as a percentage of the smaller value. These (worst case) changes lie in the range $0.03 - 0.36\%$. It seems we can count on the error in a master flatfield to be very low.

The best master flatfields seem to be the B and V filter with only a single case of a change above 0.1%. The worst region of the four is the green region. This is true for all filters.

[3]This includes the JD 2455831 V master with only two flatfields and session JD 2455856 that was cloudy for at least part of the session.

5.4 Comparison of different types of flatfields

In sections 5.1.1-5.1.4 I introduced four different methods for obtaining flatfields. I have compared the four kinds of flatfields both so that I can recommend a flatfield procedure for the Earthshine Telescope, but also because it allows me to put some constraints on a possible intrinsic gradient in the flatfield.

5.4.1 Example Moon Flatfield

Calculated Moon flatfields are as previously mentioned not an option at the moment, because the method relies on accurate positioning of the Moon image on the CCD. Figure 5.9 shows a section of the flatfield as calculated from 63 Moon images. The lunar edges are clearly visible in the flatfield, making it difficult to see the structures in the true flatfield. A couple of dust shadows and the diagonal pattern can be recognized (compare with eg. figure 5.8).

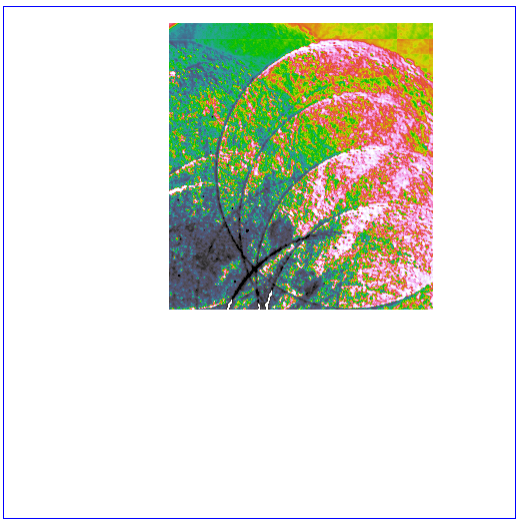

Figure 5.9: A section of the flatfield calculated with Chae's method from 63 Moon images. The outline of the CCD is indicated with the blue line. Familiar structures such as dust and the diagonal pattern are visible, but the image is scarred by the edge of the Moon in several places. (credit: Peter Thejll).

5.4.2 Gradients in Lamp, Dome & Dusk Flatfields

Examples of individual flatfields of the three remaining kinds (lamp, dome and dusk) are given in figure 5.10. I have bias subtracted and normalized the flatfields and they are shown on the same histogram equalized scale. The high frequency structures, such as bad pixels, dust and the diagonal pattern are common for all types of flatfields. The big difference between the types is the low-frequency pattern - the gradient across the surface of

the CCD. It is obvious even at a glance that the lamp flatfield is much more flat than the dusk and especially the dome flatfield.

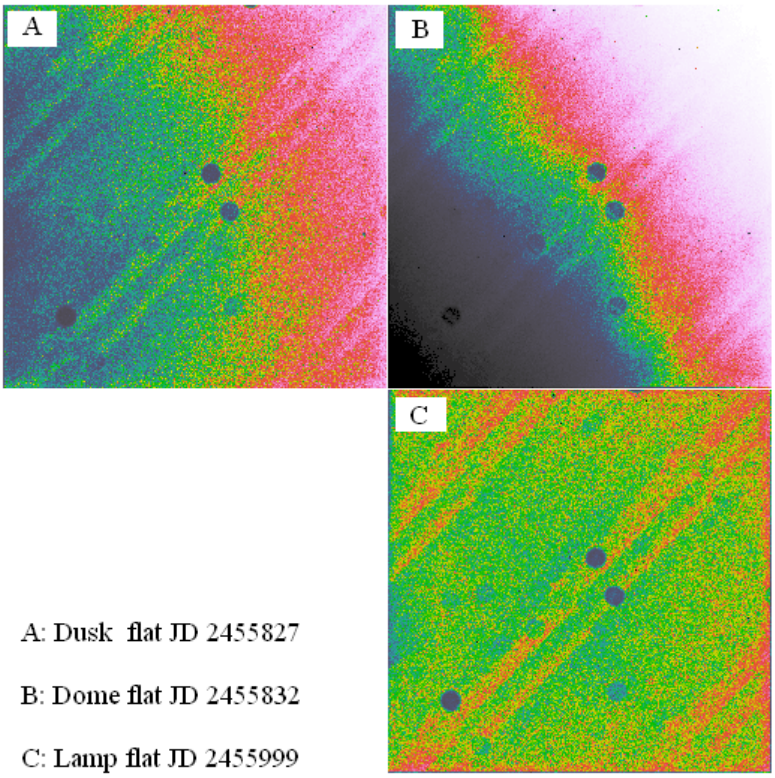

Figure 5.10: Comparison of single flatfields of different types. The familiar structures from the master flatfields are present in all types of flatfields with similar strengths, but the flatfields have different gradients.

A gradient in a single flatfield can be caused by a number of things. It is of course possible that the gradient is intrinsic to the true flatfield of the camera. If this is the case, the gradient should be left intact in the master flatfield. Alternatively, the gradient can be intrinsic to the flatfield method, eg. a result of the light source not being uniform. A third possibility is shutter dragging.

I have investigated the gradients in bias subtracted and normalized flatfields, by making a linear surface fit of the flatfields. From the coefficients of the fit I calculated, for each of the dimensions, the intensity increase across the CCD as a percentage of the mean value of the flatfield. This test has been performed on all well-exposed flatfields in the V-filter for two different lamp sessions (JD 2455924 and JD 2455999), one dusk session (JD 2455827) and one dome session (JD 2455832).

In all the tested flatfields, the largest gradient is along the x-dimension as seen in figure 5.10, the gradient along the y-dimension is a factor 5-10 smaller (with the exception of the dome flatfields) and the cross-term is

negligible. The average gradients along the x-dimension for the different sessions are given in table 5.3

Type	Session	# frames	Mean x gradient
lamp	JD 2455999	140	$0.301 \pm 0.004\%$
lamp	JD 2455924	9	$0.31 \pm 0.04\%$
dusk	JD 2455827	17	$3.3 \pm 0.9\%$
dome	JD 2455832	34	$12.88 \pm 0.04\%$

Table 5.3: The average gradient across the CCD in the x-direction for different types of flatfields. The gradient is here defined as the intensity increase across the CCD as a percentage of the mean flatfield value. The gradients are calculated from the largest coefficients (x-direction in all cases) of linear surface fits to the bias subtracted flatfields.

Several points can be made from table 5.3. The different types of flatfields have different gradients. Although the tested flatfields have the dimension with the largest gradient in common, the magnitudes of the gradients deviate from each other. The lamp flatfields have gradients that are a factor 10 smaller than those of the dusk flatfields and a factor 40 smaller than those of the dome flatfields.

It is remarkable that the gradients found in both the lamp sessions are so similar. 75 days passed between the two sessions, so the mount has been recalibrated several times, and it is unlikely that the telescope points to the exact same location inside the hohlraum sphere in both sessions. However, with the current data it is impossible to determine if the gradient seen in lamp flatfields is a result of the method, or if it is intrinsic to the flatfield. With an average intensity increase across the CCD of only 0.3% of the mean of the flatfield, the lamp flatfields set the upper limit for a possible intrinsic gradient in the true flatfield. It can therefore be argued that lamp flatfields should not have a surface fit subtracted, when they are mean-half-median combined to a master flatfield.

Within a session, the standard deviation of the gradients is small. This rules out shutter dragging as the cause of the gradient. The dusk flatfields are the exception with $\sigma = 0.9\%$, but this has another explanation. The gradients in the dusk flatfields are the gradients of the dusk sky, and although twilight skies are potentially very flat, this is only true for a few minutes [Tyson and Gal, 1993]. The 17 flatfields were observed within 14 minutes, and it is therefore not unexpected that the gradient changes. This is the reason I subtract a surface fit from each of the flatfields before mean-half-median combining them to a twilight master flatfield.

The dome flatfields have the largest gradients, with a 12% increase in the x-direction and a 10% increase in the y-direction. Dome flatfields were tested before the hohlraum lamp was in operation, so that there was an alternative to twilight flatfields, when it was cloudy at dusk and dawn. They are not being used for scientific purposes.

5.4.3 ΔF in Lamp & Dusk Master Flatfields

Master flatfields from two lamp flatfield sessions are shown in the left part of figure 5.11 together with the master flatfields from two twilight sessions. The examples in the figure are in the B-filter, and the lamp flatfields have the strongest diagonal pattern in this colour filter, exactly as for the twilight flatfields. The right part of the figure is the percent difference images from the twilight and lamp sets respectively.

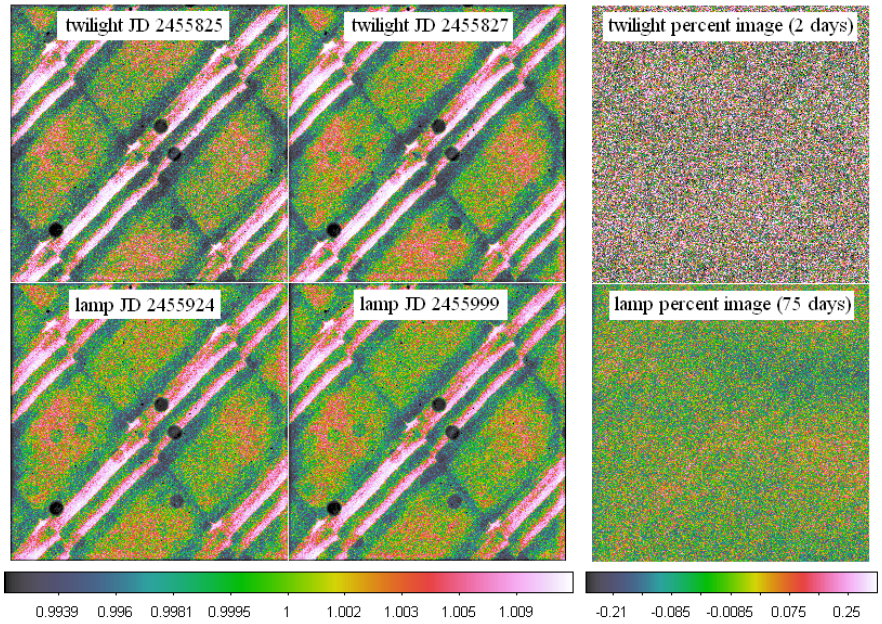

Figure 5.11: **Left:** B master flatfields from two twilight sessions and two lamp session. A surface fit has been subtracted from each flatfield of both types, so that it is only the high frequency structures that are compared. **Right:** The percent difference images of the two twilight master flatfields (top) and the two lamp master flatfields (bottom). **The scales:** The left scale is the histogram equalized and normalized ADU scale and the numbers on the right scale expresses the difference between pairs of images as a percentage of the earlier image.

The percent difference images in the right part of figure 5.11 show that the lamp master flatfields are more alike than the dusk master flatfields. The standard deviation in the twilight percent image is $\sigma = 0.24\%$ and it is $\sigma = 0.10\%$ in the lamp percent image. The two twilight masters were obtained from sessions with only 2 days in between, whereas the lamp masters have 75 days in between. The flatfield method proves more important than the time interval, and the true flatfield is stable on timescales of 75 days.

A difference image between two master flatfields contains no fixed pat-

tern, only noise. The diagonal pattern is still discernible, but this represents that the pixels here are more uncertain than in the rest of the frame. Since the variance doubles in the subtraction, the standard deviation of the difference image is a factor $\sqrt{2}$ larger than the standard deviation of a single frame without its fixed pattern. I can therefore estimate the uncertainty in a single pixel in a single master flatfield from the difference image:

$$\Delta F_{\text{master}} = \frac{\sigma_{\text{difference image}}}{\sqrt{2}} \tag{5.3}$$

$$\Delta F_{\text{dusk}} = \frac{0.24\%}{\sqrt{2}} = 0.17\% \tag{5.4}$$

$$\Delta F_{\text{lamp}} = \frac{0.10\%}{\sqrt{2}} = 0.071\%, \tag{5.5}$$

where the numbers are from the example B-filter master flatfields in this section.

5.5 Summary

Of the original four suggested types of flatfields, it is the twilight and lamp flatfields that are viable options for the Earthshine Telescope. The flatfields show structures, the most prominent of which are the diagonal pattern (a result of the thinning process in the manufacturing of the CCD), the bad pixels with low sensitivity, and shadows from dust present on the dewar window protecting the CCD. Both the diagonal pattern and the bad pixels are related to the quantum efficiency of individual pixels that may vary in time, and these structures sometime show up in difference images between a pair of master flatfields from different sessions. A few of the bad pixel groups (near the edge of the CCD) should be avoided, as they have been seen to differ with up to 7% from one master flatfield to the next.

On the basis of my analysis of the lamp and twilight flatfields I will recommend the use of lamp flatfields in the future. The lamp flatfields are easier to obtain as they can be taken at anytime in all kinds of weather, and they are more stable than the twilight flatfields. I have estimated the random component of the error on flatfield from difference images between two master flatfields. In the twilight flatfield example I found $\Delta F_{\text{dusk}} = 0.17\%$, and in the lamp example I found $\Delta F_{\text{lamp}} = 0.071\%$.

The lamp flatfields also have the smallest gradient, with a difference between the high and low end intensities of 0.3% of the flatfield mean. The gradient in lamp flatfields was determined for a total of 149 flatfields from two sessions with 75 days in between. The same gradient was found in both sessions. On the basis of this it is not possible to say if the gradient is intrinsic to the flatfield or the hohlraum sphere. We thus have an unknown intrinsic gradient no larger than 0.3% from one end of the flatfield to the other.

Chapter 6

Scattered Light

The halo of the Moon is the cumulative image of photons originating on the bright side of the Moon that are scattered in the atmosphere and in the telescope. Scattering of light has the effect to remove photons from bright areas and spread them over nearby regions. In the image of the bright side of the Moon the effect is negligible, although the scattering causes blurring. Neighbouring bright side pixels have similar intensities, and therefore they receive and lose similar numbers of photons as a result of the scattering. Dark side pixels have much lower intensities, and they are therefore contaminated with the scattered light. As mentioned in section 2.1.2, the Earthshine Telescope has been designed to minimize stray light, and removing the effects of the remaining light is one of the major challenges in measuring earthshine intensities.

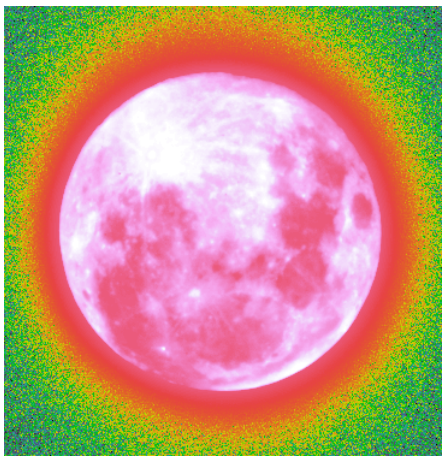

Figure 6.1: The full Moon and its halo observed with the Earthshine Telescope. The halo is due to both scattered light in the atmosphere and stray light inside the telescope.

In this thesis I have focused on one method for removing scattered light - the empirical forward modelling (EFM) that has been developed by Thejll

et al. [2012, submitted to A&A]. It is this method that I will investigate in 6.1, and the error budget in chapter 8 is based on data reduction using the scattered light estimates from the EFM method. I present an alternative method for removing scattered light in section 6.2, and a third option is the full forward modelling presented in section 1.3.1, where it is the albedo directly rather than the earthshine intensity that is derived.

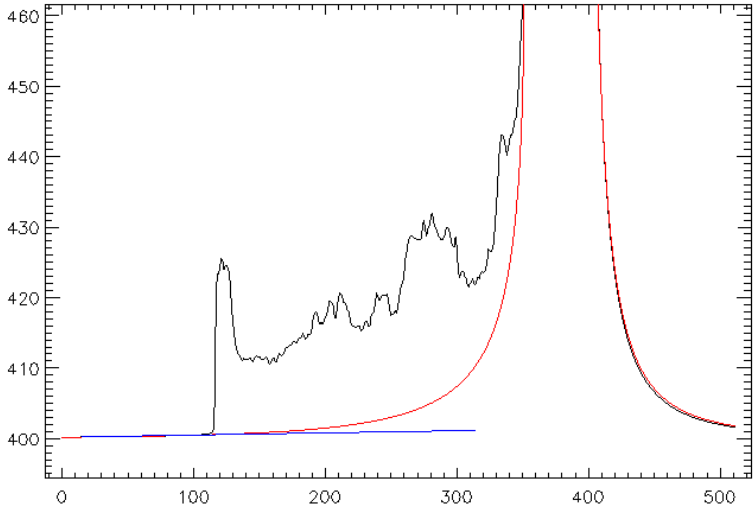

Figure 6.2: The EFM method illustrated: The y-axis is pixel counts in ADU, and the x-axis is the pixel number in a single row of the CCD. The black line is a cross section of an observed Moon image, with the leftmost part being the sky-background, then it is the dark side followed by the bright side, and the rightmost part is sky-background again. The red line is a fitted EFM model that is constrained by flux-conservation and forced to fit the sky off the dark side limb in the observed image. The blue line is the BBSO linear method where the linear fit from the sky is extrapolated into the dark side (see section 6.2).

6.1 Empirical Forward Model

One approach to removing the scattered light is to model the halo, and subtract this from the observed image. A combined atmospheric and instrumental halo profile has been determined empirically from observations of bright stars (to determine the point spread function (PSF)) and the Moon itself. The details of this procedure are given in Thejll et al. [2012]. The Moon is of course an extended object, and the halo profile can be described with a power law of the PSF profile (which is in itself a power law [King, 1971]),

$$\text{Halo profile} \propto (PSF(r))^{\alpha}. \tag{6.1}$$

The slope of the power law α can vary from night to night as a result of changing sky conditions. α is kept as a free parameter in the model and is fitted to every lunar frame as part of the earthshine intensity measurements.

The EFM method works as follows: The sun-lit part of the Moon in the observed image is used as a source that is convolved with a trial halo profile. The sky part of this model is compared to the sky part of the observed image and the model parameters are iteratively adjusted (under the constraint of flux conservation) until there is a good fit between model sky and observed sky. The resulting image (the best fitting model) is called the EFM-image, and it contains both the observed bright side of the Moon and a fitted halo. Taking the difference between the original observed image and the EFM-image leaves the dark side cleaned from scattered light. The measured earthshine intensities in individual pixels or in larger pixel areas can be read directly from this image.

Thejll et al. [2012] have tested the EFM method with synthetic Moon images (the synthetic Moon images are described in section 1.3.1). The idea is to simulate realistic observational data, where the earthshine intensities are known, remove the scattered light and compare the derived earthshine intensities with the known values. Thejll et al. find that the dark side intensity can be determined to better than 1% with the EFM method for lunar phases in the range $\pm 90^\circ - 150^\circ$.

6.1.1 Quantities for the Error Budget

The framework for the error budget that I set up in section 3.3 is appropriate for the EFM method for removing scattered light, because an actual image is subtracted from the Moon observations. The EFM image contains both the observed bright side and the fitted halo, but ignoring the bright side pixels (where the scattered light is negligible), the EFM image is the S-image in the error equation (3.14). The typical stray light level that adds to the dark side intensity can be determined eg. from the mean of a box in the EFM image, located where the dark side is in the Moon image. The level of stray light depends strongly on lunar phase and decreases with distance from the bright side.

I have determined the uncertainty in the scattered light, ΔS, with bootstrapping of the EFM method. In place of an observed image I used a synthetic Moon image that was convolved with a halo profile with an exponent α appropriate for clear sky conditions. I generated 100 simulated "observed" images from this by adding random noise, and then the scattered light was estimated with the EFM method. The result was 100 EFM images with the same bright side but different estimates of the scattered light. The average image is shown in the left part of figure 6.3, where the bright side pixels have been replaced by zeros. The right part of figure 6.3 shows the relative error $\Delta S/S$ in percent, where ΔS is estimated as the standard deviation image of the 100 EFM images. The scatter in the EFM estimates is very small, typically a few tenths of a percent of the level of scattered light.

The scattered light term in the error equation (3.14) is the uncertainty

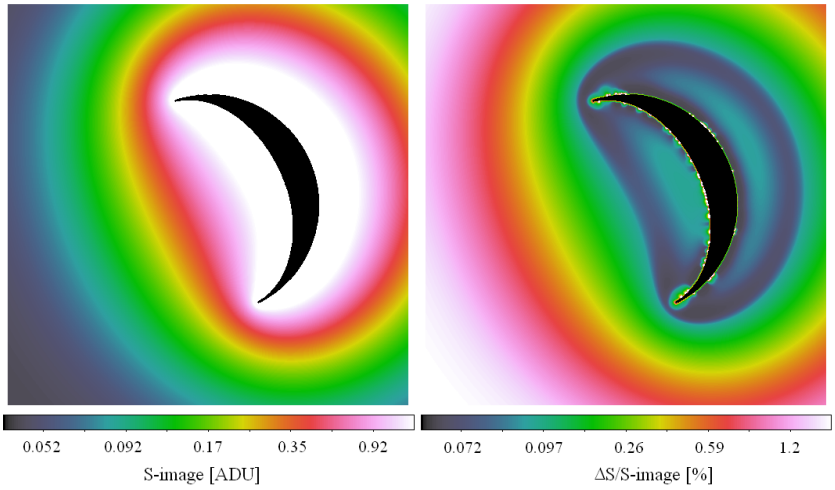

Figure 6.3: **Left:** The average stray light image (S) from 100 EFM estimates. The "observed" image is a synthetic Moon image convolved with a halo profile and with random noise. The scattered light has counts around 0.2ADU in the dark side pixels. **Right:** $\Delta S/S$ percent image, where ΔS is estimated as the standard deviation image of the 100 EFM estimates. The relative uncertainty increases with distance from the bright side as a result of the scattered light intensity decrease. The bright side of the Moon has been masked in both images.

in the scattered light relative to the signal:

$$S\text{-term} = \frac{\Delta S}{O - S - B} \tag{6.2}$$

It is possible to make an image representing this term. An example of such an image is given in figure 6.4. O is a co-added image of 11 observed Moon images from JD 2455923 (good photometric night), and B is the proper scaled superbias. S and ΔS are the images described above and in figure 6.3, and the synthetic image that was used instead of the observed images in the EFM code was constructed to simulate the real observations from this particular night. The arithmetic operations are as usual performed pixel by pixel, so that location effects can be seen in figure 6.4. The bright side pixels in S and ΔS are masked with the value zero, and the bright side is therefore unaffected by the operations.

From figure 6.4 we can see that the uncertainty in the value of the scattered light that is subtracted from the observation is less than 0.02% of the earthshine signal ($O - S - B$). The low relative uncertainty is a result of a low level of straylight at phases close to the New Moon, and a small scatter in the S-values estimated with the EFM method. The figure also reveals some trouble areas. Close to the lunar limb, especially around the horns, the model halos are not a good fit to observed halos. The sky off the bright side of the Moon is obviously not well fitted either. This indicates that earthshine intensities should be extracted close to the edge

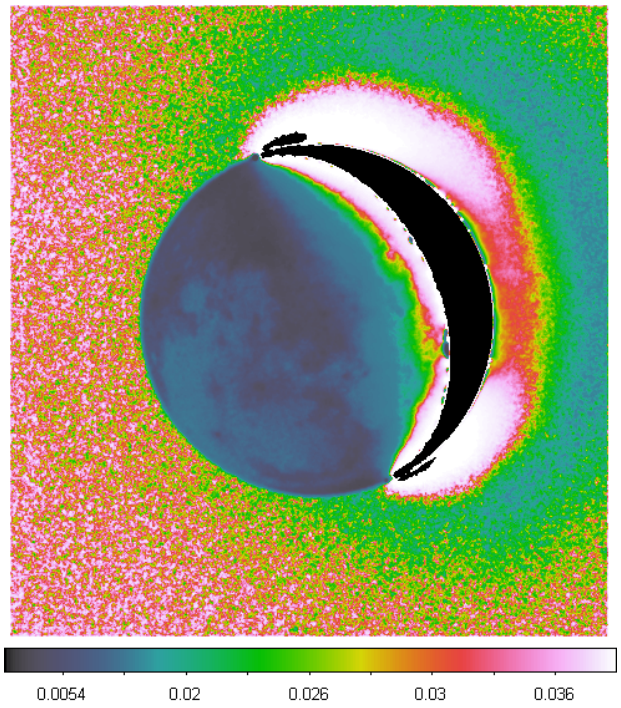

Figure 6.4: $\Delta S/(O-S-B)$ in percent. The O-image is a co-added image from real Moon observations, but the S- and ΔS-images are the EFM estimates from a simulated "observation". The uncertainty in the scattered light removal on the dark side of the Moon is a very small percentage of the earthshine signal (O-S-B).

of the Moon near the lunar equator - as far away from the bright side as possible. We saw in the right part of figure 6.3 that the relative uncertainty $\Delta S/S$ increases with distance to the bright side, but there is hardly any scattered light to remove there to begin with on good photometric nights.

6.1.2 Bias in the EFM Method

The advantage of working with synthetic images as opposed to real observations, is that I can retrieve "true" scattered light images (S_{true}) and compare them to the EFM estimates (S_{EFM}). This allows me to investigate not only the scatter in the EFM estimates, but also if there is a systematic error in the method. As in the above example I generate 100 EFM estimates of the scattered light in 100 identical (except for random noise) synthetic Moon images that simulate real observations. For each of the 100 runs I save the true scattered light image along with the estimate, and I make an average image of both S_{true} and S_{EFM}. I can now compare the true level of scattered light with the estimate in a box on the dark side of the Moon.

The level of scattered light depends strongly on both the phase of the Moon and the distance from the bright side. I have taken the changing

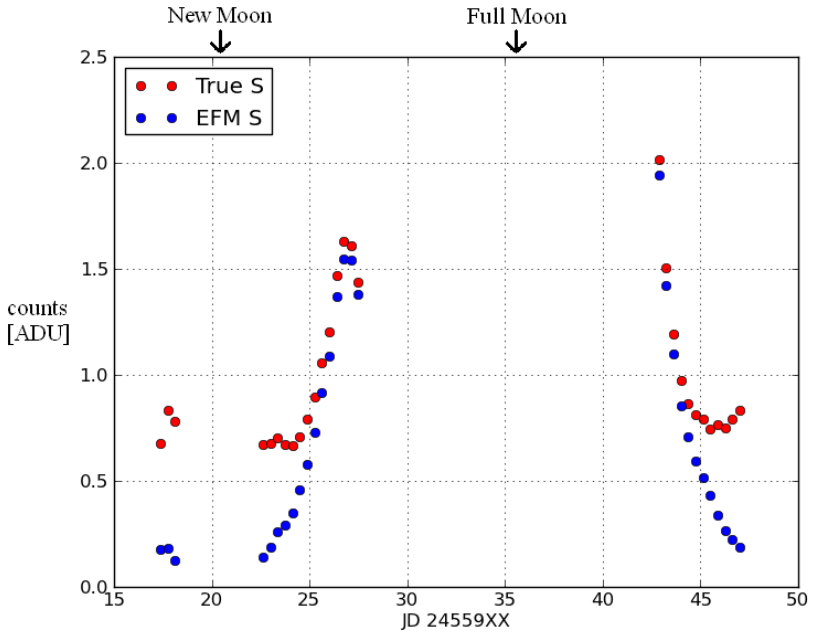

Figure 6.5: Investigating bias in the EFM method: With the use of synthetic images I can extract the true scattered light image along with the estimated EFM scattered light image, and compare them in a box on the dark side of the Moon. Each of the blue points is the box average scattered light count from 100 EFM estimates (the errorbars from the standard deviations are smaller than the size of the points). The corresponding red point is the box average count in the true scattered light images. The Julian dates cover a month, and the synthetic images that are represented here, are the ones with a phase relevant for Co-add mode. There is a phase-dependent bias, which is largest close to New Moon.

phases into account, by repeating the above procedure for many different phases. I had access to a month's worth of realistic, synthetic images, generated at 9 hour intervals, and I have performed the analysis for a total of 29 images from the phases that are relevant to Co-add mode. For each of the 29 synthetic images I have determined S_{true} and S_{EFM} in a dark side box covering about 50x100 pixels, a few pixels away from the dark limb. The box is necessarily not the same for all phases.

The results are shown in figure 6.5 and 6.6. Figure 6.5 gives the dark side scattered light estimate in ADU along with the known true value, whereas figure 6.6 gives the relative systematic uncertainty in scattered light $(S_{\text{true}} - S_{\text{EFM}})/S_{\text{true}}$ in percent. Both plots have an x-axis with the Julian date that the synthetic Moon images simulate, so that it is possible to see how the systematic error changes with the phases.

At Half Moon, when the scattered light on the dark side reaches counts

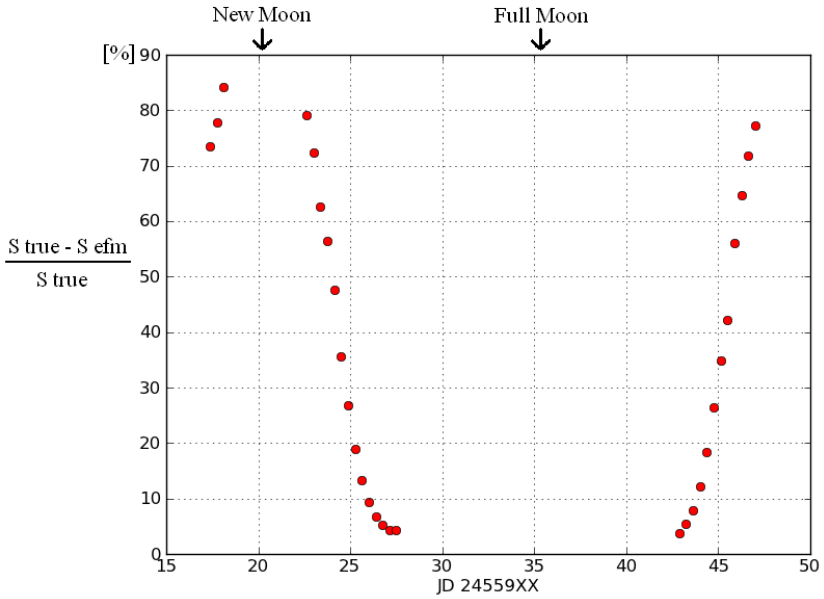

Figure 6.6: The relative systematic uncertainty in scattered light for the 29 different phases in figure 6.5. $\Delta S_{\text{sys}}/S$ increases dramatically towards New Moon.

of 1.5ADU, the EFM estimate is only about 5% wrong. However, close to the New Moon, when the stray light is as low as 0.7ADU corresponding to a couple of photons, the EFM estimate is about 80% wrong. There is a strong phase-dependent systematic error in the scattered light estimates, and it is more difficult to estimate the scattered light, when there is less scattered light to begin with.

It is interesting that S_{true} is consistently larger than S_{EFM}, for all the tested phases. It appears we are underestimating the amount of scattered light, with the consequence that we do not succeed in removing all the scattered light. If this holds true with further tests, and the bias can be proven to be constant for a given phase, then it will be possible to empirically correct for it. However, I suggest that more tests are carried out. We need to know if the large systematic uncertainty is a result of the fitting routine, the modelled halo or the synthetic images. It would also be interesting to carry out the same analysis as I have done here, but for smaller boxes at different distances from the bright part of the Moon.

6.2 BBSO Linear Extrapolation

Another method for removing scattered light from the dark side of the Moon is the BBSO linear extrapolation method, adopted from the BBSO group [Qiu et al., 2003]. The Lund-DMI group has worked with this method so that we may better compare our earthshine-to-moonlight intensities with the BBSO results, and so that we can compare the different

methods for removing scattered light.

The BBSO method uses a linear least squares fit to all pixels in five degree cones on the sky off the dark side disc. The dark side intensity is background corrected by extrapolating the linear fit onto the the lunar disc. The BBSO group has found that the sky background is well fitted by a linear fit (see right part of figure 6.7) as long as you are sufficiently far away from the bright part of the Moon, and they consider the dark side near lunar "equator" close to the limb to be sufficiently far.

Thejll et al. [2012] have tested the linear extrapolation method on synthetic images in the same manner as for the EFM method: The synthetic images have known earthshine intensities that can be compared to the derived intensities after the scattered light has been removed. They find that the dark side intensity can be determined to better than 10% with the linear extrapolation method for lunar phases in the range $\pm 120^\circ - 150^\circ$.

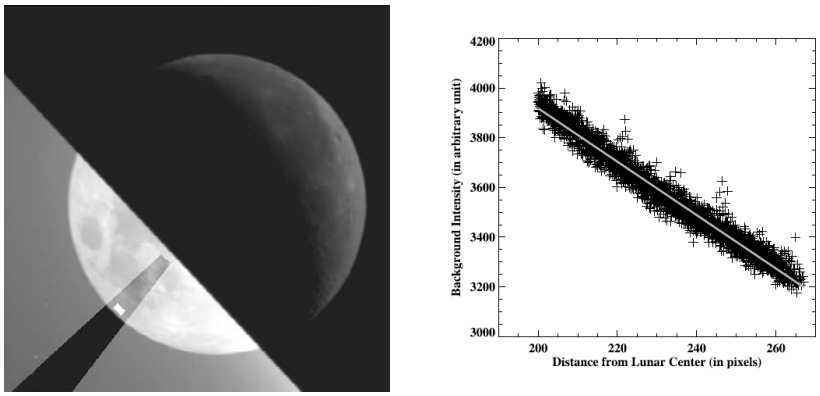

Figure 6.7: **Left:** Illustration of the BBSO linear extrapolation method for scattered light removal. The intensity of the sky background within a five degree cone is fitted as a linear function of distance from the lunar center. Extrapolating the linear fit to points inside the lunar disc, the sky background is subtracted from the earthshine intensities inside the cone. It is the intensity of the small bright patch near the limb that is of interest. **Right**: The BBSO group has measured the sky background as a function of the distance from the lunar center. The overlaying white line is the linear fit. (credit: Qiu et al. [2003]).

Chapter 7

Aligning Moon Images

Each observing night we obtain large numbers of images of the Moon in each of the five colour filters. The images from any given filter can then be averaged to construct a single co-added image with increased S/N compared to a single image of the Moon. Before the images can be averaged it is important to ensure that the Moon is positioned in the exact same location on the CCD frame in all images. If the images are not carefully aligned then a pixel in the averaged image may contain contributions from both the bright highland and the dark maria, increasing the noise rather than the signal.

High precision subpixel alignment is especially important in Co-add mode which depends on stacking many images to increase the S/N, but even in the other modes it is necessary to align and average several images. We are also dependent on a good alignment procedure for the forward modelling methods, since the observed images must be aligned with the synthetic images. Related to alignment is the ability to define the exact location of the Moon in an image. This is neccesary if we wish to calculate flatfields from dither images of the Moon (Moon flatfields are described in sections 5.1.4 and 5.4.1).

There are two steps to any subpixel alignment method. First one must calculate the offset coordinates that will place the Moon at the desired location in the frame. Next the image is translated with the specified offset, and for subpixel precision it is necessary to use interpolation. I have worked with two different alignment procedures that differ from each other in both steps. They are described in the next two sections 7.1 and 7.2. The two methods are compared in section 7.3. A method based on subpixel edge-detection is introduced in section 7.4. This last method shows promise, but it has not been implemented yet.

7.1 Chae's method

This alignment method is written by Jongchul Chae (Big Bear Solar Observatory) and consists of two IDL routines, *alignoffset* and *shift_sub* [Chae, website]. *alignoffset* determines the offset of an image with respect to a

reference image. This is done by using a FFT method to maximize the cross-correlation between the reference image and the observed image. For the reference image, I have used a well-centered image (if available) amongst the ones from the observing session in question.

shift_sub shifts the image with subpixel accuracies using the built-in IDL routine *interpolate*. This is a bilinear interpolation, which means a linear interpolation is first performed in one direction and then in the other.

7.2 Center of mass method

This alignment method has been developed by Karl Åström (Lund University) in matlab. I have implemented it in Python and customized it to my needs. The two central functions are *CenterMass* and *MoveImage*.

CenterMass calculates the center of mass of the bright side of the Moon. The bright side has been defined a bit roughly as pixels with values greater than or equal to 1000. This has proven accurate for the images I have worked with so far. An alternative is using the pixels with values above 1/75 of the maximum intensity [Thejll et al., 2012, submitted to Astronomy & Astrophysics]. The offset is determined with respect to a reference position. The reference position is near the center of the 512x512 frame with the appropriate position varying slightly with the phase of the Moon.

MoveImage first translates the image in whole pixels and then in subpixels. The subpixel move consists of exponential interpolation followed by subpixel translation and resampling. In practice this is implemented as a 2D convolution of the image (already shifted in whole pixels) and a filter matrix of exponential functions [Åström and Heyden, 1999, Castleman, 1996].

7.3 Comparison of alignment methods

7.3.1 The test images

The Moon images used in this analysis were obtained JD 2455864 by Peter Thejll. Sky conditions were clear and the Moon was setting. All colour filters were used, but I have only selected images observed in the V-filter. Images with obvious shutter failure or over-exposed bright limb were rejected, leaving me with 7 groups of 11 images, where a group of images were obtained within 0.7 minutes. In this analysis I have aligned and co-added each group separately. Since the images in a group are obtained within a short time, I can be sure that intensity variations are not due to increasing airmass as the Moon sets. All the images have the same requested exposure time of 0.1174s.

7.3.2 Results

Chae's method

For each group of 11 images I chose the first image as the reference image. This meant the shifts were entirely subpixel. There were no visible differ-

ences between images before and after alignment. Particularly there was no discernible blurring of the lunar features.

CM method

A reference position was chosen so that the Moon was well centered after alignment. This meant that the images were shifted with quite a few whole pixels, and that they will need to be cropped accordingly, prior to any scientific use. There was significant blurring of the lunar features for all images tested with this method.

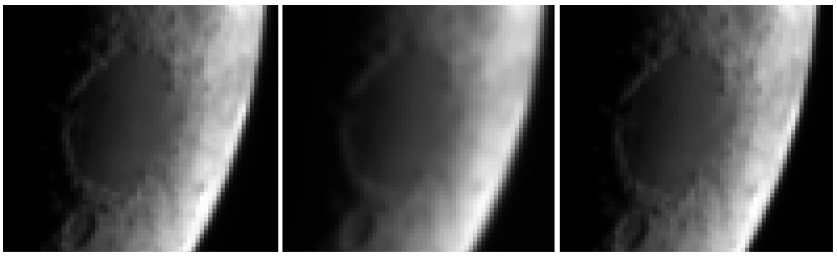

Figure 7.1: Alignment of a single Moon image from session JD 2455864. Zoom on the Crisium crater. **Left:** Raw image before alignment. **Middle:** After alignment with center-of-mass method. There is visible blurring of lunar features. **Right:** After alignment with Chae's method. There is no visible blurring of lunar features.

Standard deviation

One way to evaluate the performance of the alignment methods is to compare the standard deviation in the individual pixels after alignment with each of the two methods. The standard deviation in a pixel is partly due to uncertainties related to the observation itself (photon noise) and partly due to imperfect alignment.

I have aligned a stack of images with each of the two alignment methods and determined the standard deviation for each pixel. This image represents the ΔO in the error equations (see section 3.3). In figure 7.2 I give an example of a $\Delta O/O$ percent image from the test-night, where O is the co-added image of the stack. The left images are aligned with Chae's method, and the right images are aligned with the center of mass method. The only difference between top and bottom images is the intensity scaling. The top images are shown on a square root scale that emphasizes the bright side of the Moon, whereas the bottom images are shown on a histogram equalized scale that emphasizes the dark side of the Moon.

It is clear from figure 7.2 that alignment with the center of mass (CM) method results in lower standard deviations than alignment with Chae's method. On the bright side of the Moon, the CM method has typical standard deviations of about 0.1-2%, and Chae's method has standard deviations around 0.4-3.5%. Both methods have problems with the bright

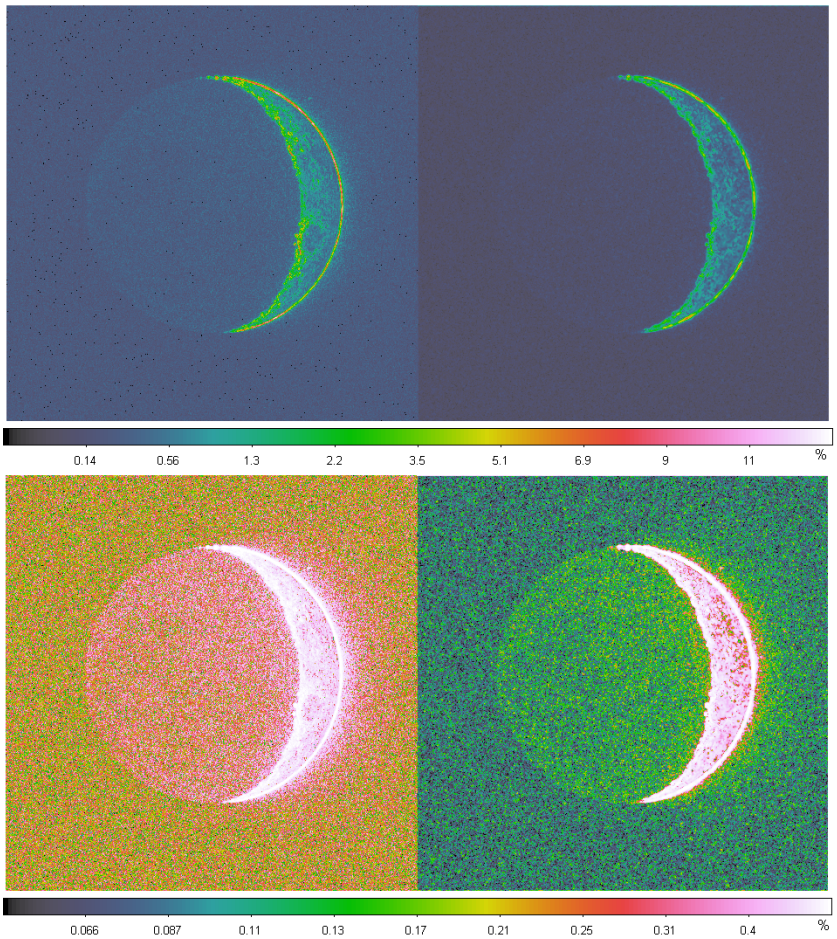

Figure 7.2: $\Delta O/O$ percent image from a stack of 11 aligned Moon images from session JD 2455864. Top and bottom images are the same except for the intensity scaling. Top images are shown on a square root scale to emphasize the bright side, and the bottom images are shown on a histogram equalized scale to emphasize the dark side. **Left:** Images are aligned with Chae's method. **Right:** The same images aligned with the center of mass method. The standard deviations are generally lower in images aligned with the center of mass method compared to images aligned with Chae's method. The lower standard deviations of the center of mass method is a consequence of the stronger blurring with this method.

limb where even a slight mis-alignment will result in large standard deviations. The worst case pixels have standard deviations of upto 7% in the case of the CM method and upto 12% for Chae's method. The difference in performance of the two alignment methods is more pronounced for the earthshine. Typical CM dark side standard deviations are around 0.07-0.2%, whereas Chae dark side standard deviations are about 0.2-0.4%. The results in this example are representative for all stacks of images from the same night. I have aligned a few random samples from other observation nights with different lunar phases as well, and the results have been similar.

Mixing the routines

I mentioned in the beginning of the chapter that alignment of images consists of two steps. The first is calculating an offset, and the second is the translation of the image. To better compare the two methods, I have tried mixing up the alignment routines for one of the test image groups. The two new combinations are:

A Offset is calculated with the CM routine *CenterMass*
Image is translated with the Chae routine *shift_sub*
B Offset is calculated with the Chae routine *alignoffset*
Image is translated with the CM routine *MoveImage*

The 11 test images were aligned with first the routines in case A, then the routines in case B. For each case the images were co-added after alignment, and as before I have created a $\Delta O/O$ percent image. The results are shown in figure 7.3 together with the results from alignment with purely the CM method or the Chae method.

7.3.3 Discussion

From figure 7.3 we can see that the biggest difference is not which routine was used to calculate the offset but rather which translation routine was used. Translation with the CM method results in the lowest standard deviations in the aligned stack of images regardless of the method used to calculate the offset. It is in other words the interpolation technique that makes the difference. This signifies that the lower standard deviations arising from the CM alignment method are not a result of the CM method aligning images more precisely than Chae's method. Instead the explanation can be found in the middle image in figure 7.1. The CM method causes significant blurring, which is the visible outcome of a strong averaging effect in the interpolation. The CM translation routine has some free parameters that can be adjusted if you want a less pronounced smoothing.

So which alignment method is best for aligning images? For the images that were translated with Chae's method, the lowest standard deviations are found in the image stack that had their offset calculated with the CM method (case A, top left image in figure 7.3), rather than the case of the pure Chae method (bottom left). In practice, which routine calculates the offset more precisely will depend on the phase of the Moon, the location

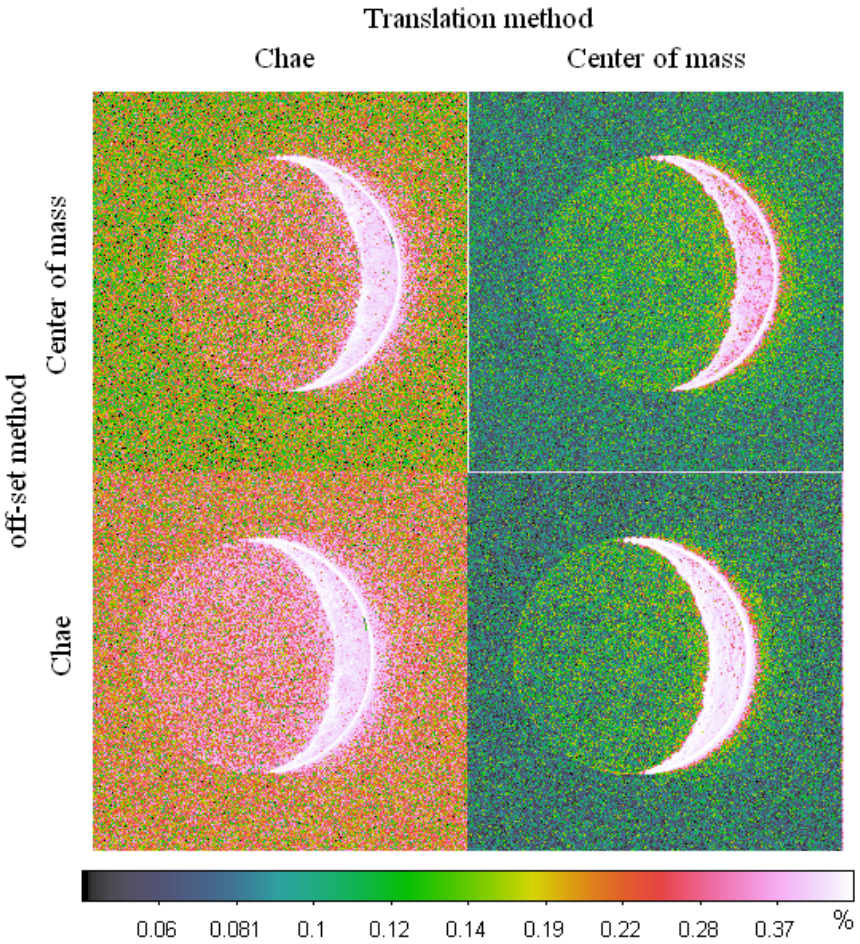

Figure 7.3: $\Delta O/O$ percent images. A group of 11 images has been aligned with the four possible combinations of calculating the offset and translating the image. Translation with the CM method results in the lowest standard deviations regardless of which method was used to calculate the offset, and for the two cases where the translation was done with Chae's method, the standard deviations were lowest when the offset was calculated with the CM method. The pure Chae alignment routine resulted in the highest standard deviations for this particular stack of images. Differences in standard deviations arising from the translation method tell you something about the interpolation (and by extension the smoothing), whereas differences arising from the calculation of the offset tell you something about the precision of the alignment.

of the Moon on the CCD and the diversity of the lunar images that are to be aligned.

Both the Chae and the CM alignment methods result in standard deviations that are higher than the theoretical values from photon noise and readout noise (see eq. 8.1 and section 8.1.5). The imprecise alignment procedures add noise to the pixels. One could argue that the averaging in the center of mass method compensates somewhat for this.

7.4 Edge detection

A third alignment method relies on subpixel detection of the lunar edge. First a rough center of mass calculation or something similar is performed to shift the image in whole pixels. Then the subpixel edge detection [Åström and Heyden, 1999] is performed on both the bright and the dark side of the Moon, allowing for a precise estimate of the equation of an ellipse describing the lunar shape. Finally the subpixel shift is performed with one interpolation technique or the other, moving the images so that the center of the ellipse coincides with the center of the CCD frame.

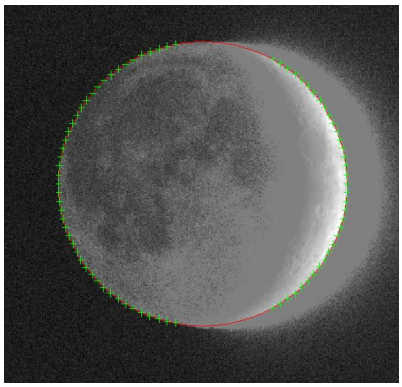

Figure 7.4: Preliminary analysis indicates that we can expect subpixel edge detection with a BS precision of 0.05 pixels and DS precision of 0.2 pixels. We can expect image alignment to a precision better than 0.05 pixels. Credit: Kalle Åström.

The preliminary results from this method is promising (see figure 7.4), with expected alignment precisions better than 0.05 pixels. However, the method has yet to be implemented properly to work for all phases and initial locations on the CCD. It will be worthwhile pursuing a better alignment procedure, especially because we hope to be able to produce high quality Moon flatfields.

Chapter 8

Error Budget, Co-add Mode

8.1 Precision

8.1.1 Error From Object Frame

I need typical pixel values for the raw object image O and its associated uncertainty ΔO. O can be determined directly from the Moon images, and in principle ΔO can be determined as the standard deviation for a single pixel in many perfectly aligned Moon images. However, in chapter 7 I found that the current alignment methods are less than perfect. Imperfect alignment will introduce additional noise and possibly also blurring (which is in effect an averaging of the pixels). ΔO determined from the standard deviation in a pixel through a stack of aligned Moon images will be the combined uncertainty from the signal, readout noise and the alignment process.

In order to clarify the picture I will here ignore alignment, and use the theoretical equation for noise in output signal from a CCD. This noise is a combination of the intrinsic photon noise (described by the Poisson distribution) and readout noise, and it was given in equation (4.6). The signal is $O - S - B$, and the uncertainty in the object frame is therefore

$$\Delta O = \sqrt{\frac{O - S - B}{g} + \frac{RON}{g}}, \tag{8.1}$$

with g being the gain.

8.1.2 Error Budget, Dark Side

In Co-add mode we observe at phases where the earthshine is relatively bright, but even so the moonlight intensity is typically about $4,000$ times as bright as the earthshine. A typical count in a dark side pixel in Co-add mode is 405ADU, and keeping in mind the bias level is $\sim$ 395ADU that corresponds to about 38 photons, where one of them might be scattered light originating on the bright side. Typical dark side values for all the quantities in the error equation (3.14) are listed in table 8.1 in units of ADU.

O	ΔO	B	ΔB	F'	$\Delta F'$	S	ΔS
405	3.79	394.975	0.088	1	0.0007	0.2	0.0005

Table 8.1: Typical values in ADU for the error budget on the dark side of the Moon. The numbers are relevant for a lunar phase angle of about 140°. The uncertainties are for a single pixel in a single frame. ΔO is from equation (8.1), ΔB is the SEM of the superbias from equation (4.3), $\Delta F'$ is the uncertainty in a lamp master flatfield from equation (5.5) and ΔS is from figure 6.3.

Working with such a small signal, it is expected that the dominating term in the error equation (3.14) is the O-term. This is indeed the case. I have inserted the typical dark side values from table 8.1 in equation (3.14) to find the the relative error on intensity for a single dark side pixel in a single Moon image. By averaging over multiple frames, the error on O is reduced by $\sqrt{\#\text{ frames}}$, and by averaging over multiple pixels, the error on O, B, F' and S is reduced by $\sqrt{\#\text{ pixels}}$. Table 8.2 lists the relative error on the dark side intensity for a few different choices of frame numbers and pixel numbers. The relative contributions to the error on intensity from the four different error terms are also given in table 8.2.

# frames	1	100	100	100
# pixels	1	1	10x10	40x40
$\Delta I/I$	38.61%	3.96%	0.40%	0.10%
O-term	99.95%	94.86%	94.86%	94.86%
B-term	0.05%	5.11%	5.11%	5.11%
F'-term	$3.3 \cdot 10^{-4}$%	0.03%	0.03%	0.03%
S-term	$1.7 \cdot 10^{-6}$	$1.6 \cdot 10^{-4}$%	$1.6 \cdot 10^{-4}$%	$1.6 \cdot 10^{-4}$%

Table 8.2: Error budget for the dark side of the Moon. The first row gives the number of frames that are co-added and the second row the number of pixels that are averaged. The third row is the relative error on intensity, seen to improve dramatically with the number of frames and pixels. The four bottom rows are the relative contributions to $\Delta I/I$ from each of the four terms in equation (3.14).

It is seen from table 8.2 that we can achieve a precision of 0.1% if we co-add 100 frames and determine the average dark side intensity from 40x40 pixels. The O-term, stemming from photon noise and readout noise, is the dominating source of the intensity error, as expected. The error in the bias frame contributes with a significant $\sim 5\%$, and the errors in flatfield and the scattered light are negligible.

8.1.3 Error Budget, Bright Side

Scattered light is negligible on the bright side of the Moon (see chapter 6, page 67), and therefore I have left the S-term out of the bright side error

budget. The error equation (3.14) reduces to

$$\left(\frac{\Delta I}{I}\right)^2 = \left(\frac{\Delta O}{O-B}\right)^2 + \left(\frac{\Delta B}{O-B}\right)^2 + \left(\frac{\Delta F'}{F'}\right)^2. \tag{8.2}$$

The typical bright side values for the error budget are listed in table 8.3 in units of ADU. The B and F' values are of course the same as on the dark side.

O	ΔO	B	ΔB	F'	$\Delta F'$
40,000	104.3	394.975	0.088	1	0.0007

Table 8.3: Typical values in ADU for the error budget on the bright side of the Moon. The uncertainties are for a single pixel in a single frame. ΔO is again determined from equation (8.1), only leaving out S.

The Poisson distribution of photon noise has the special property that

$$\frac{\Delta O_{\text{photons}}}{O_{\text{photons}}} = \frac{\sqrt{N}}{N} = \frac{1}{\sqrt{N}} \tag{8.3}$$

where N is the number of photons. With typical bright side pixel counts of 40,000ADU, corresponding to about 152,000 photons, the O-term has a small absolute value even for a single pixel. Equivalent to the treatment of the dark side, I have inserted the typical bright side values from table 8.3 in equation 8.2, and the results are given in table 8.4.

# frames	1	100	100	100
# pixels	1	1	10x10	40x40
$\Delta I/I$	0.27%	0.07%	$7.5 \cdot 10^{-3}$%	$1.9 \cdot 10^{-3}$%
O-term	93.40%	12.39%	12.39%	12.39%
B-term	$6.7 \cdot 10^{-5}$%	$8.8 \cdot 10^{-4}$%	$8.8 \cdot 10^{-4}$%	$8.8 \cdot 10^{-4}$%
F'-term	6.60%	87.61%	87.61%	87.61%

Table 8.4: Error budget for the bright side of the Moon. The error on the intensity is improved by averaging over multiple frames and pixels. The four bottom rows are the relative contributions to $\Delta I/I$ from each of the four terms in equation (8.2).

In the case of a single pixel in a single frame, the O-term is still the dominant source of error on intensity. But with 100 co-added frames, the O-contribution is down to 12%, and it is the error on flatfield that dominates. The flatfield error term has the same absolute size as in the dark side case, but the bias error term has O in the denominator, and has therefore become negligible. A precision of 0.1% is reached already for one pixel and 100 frames.

8.1.4 Uncertainty in the Intensity Ratio

The quantity we are interested in is the ratio of earthshine to moonlight intensities, $I_{\text{dark side}}/I_{\text{bright side}}$ and its uncertainty that can be determined from

$$\left(\frac{\Delta I_{\text{ratio}}}{I_{\text{ratio}}}\right)^2 = \left(\frac{\Delta I_{\text{dark side}}}{I_{\text{dark side}}}\right)^2 + \left(\frac{\Delta I_{\text{bright side}}}{I_{\text{bright side}}}\right)^2. \tag{8.4}$$

I can now insert the estimates from sections 8.1.2 and 8.1.3. Assuming I have 100 co-added frames and make use of dark side and bright side intensities from areas covering 40x40 pixels, I find the uncertainty in the intensity ratio to be

$$\frac{\Delta I_{\text{ratio}}}{I_{\text{ratio}}} = \sqrt{\left(\frac{0.1}{100}\right)^2 + \left(\frac{1.9 \cdot 10^{-3}}{100}\right)^2} \cdot 100 \approx 0.1\%. \tag{8.5}$$

8.1.5 Signal to Noise Image

The signal-to-noise ratio of the dark and bright side intensities can easily be determined from the squared relative error

$$\frac{S}{N} = \frac{1}{\sqrt{(\Delta I/I)^2}}. \tag{8.6}$$

By calculating $(\Delta I/I)^2$, pixel by pixel from equation (3.14) and then using equation (8.6) pixel by pixel, it is possible to create a S/N image.

Figure 8.1 is an examle of such a S/N image. It was calculated from a group of 11 Moon images obtained within a minute on JD 2455923 in the V-filter. The observation log states there was little scattered light [Thejll, 2011a]. I have aligned the images with the center of mass method and co-added them with the mean-half-median method. Thus I have obtained a co-added object image O, and a standard deviation image, ΔO.

A quick test of average values in a 60x100 pixels box on the dark side yields $O = 405$ADU and $\Delta O = 0.4$ADU. The theoretical value for ΔO is $3.79/\sqrt{11} = 0.28$ADU. The discrepancy is most likely a combination of errors arising from the alignment procedure and an uncertain exposure time.

For B and ΔB I have used the superbias and the corresponding standard deviation image (the "temporal standard deviation" in section 4.2.1). For the F'-image I have used the closest available master flatfield in the same colour filter, and for $\Delta F'$ a difference image between two master flatfields. S and ΔS were made as an average- and standard deviation image respectively of 100 models of the scattered light, using a synthetic Moon image as the source of the scattered light. The synthetic image was made to have the same phase, libration, distance etc. as the real images, and the halo was modelled to resemble clear conditions. Both of the images S and ΔS had the value zero on the bright side of the Moon, where we do not correct for scattered light. S and $\Delta S/S$ are displayed in figure 6.3.

Not surprisingly, the S/N values in figure 8.1 are much smaller on the dark side of the Moon than on the bright side. Typical dark side S/N

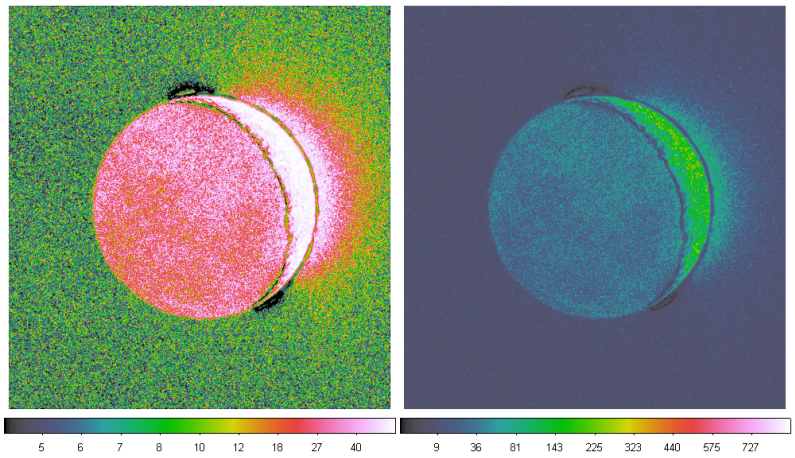

Figure 8.1: S/N image calculated pixel by pixel from 11 co-added images obtained on JD 2455923. **Left:** Hist.eq. scale to emphsize the dark side values. The dark side S/N-value per pixel is 22 ± 10. **Right:** Sq.root scale to emphasize the bright side values. The bright side S/N-value per pixel is 147 ± 78. The S/N values stated here are determined from the boxes that can be seen in appendix figure D.1.

values lie in the range $12 - 32$, and bright side S/N values lie in the range $69 - 225$. A S/N for the dark side above 12 for only 11 co-added images is promising. A thing worth mentioning in figure 8.1 is the arc-like features of low S/N near the horns of the Moon, where the model halo fits poorly with the real halo.

8.2 Accuracy

Thus far, the focus has been on random uncertainties, which we assume are independent. Systematic uncertainties are usually harder to evaluate and even to detect, because it requires knowledge of the true value of the measured quantity. It is important to identify possible systematic errors and reduce them until they are smaller than the required precision. My investigations in chapters 4-6 allow me to identify some possible sources of systematic errors in the data reduction and estimate their relative systematic uncertainties.

When it comes to systematic errors, we cannot assume the errors are independent, and I therefore use the general expression

$$\Delta I_{\text{sys}} \leq \left|\frac{\partial I}{\partial O}\right| \Delta O_{\text{sys}} + \left|\frac{\partial I}{\partial S}\right| \Delta S_{\text{sys}} + \left|\frac{\partial I}{\partial B}\right| \Delta B_{\text{sys}} + \left|\frac{\partial I}{\partial F}\right| \Delta F_{\text{sys}}, \tag{8.7}$$

which gives an upper bound on the uncertainty in intensity (the equivalent expression for independent errors is eq. (3.7)). The term for the exposure time is again left out, because this is the error budget for Co-add mode. The partial derivatives (eq. (3.8)-(3.11)) are of course unchanged, and the

relative error is

$$\frac{\Delta I_{\text{sys}}}{I} \leq \left|\frac{\Delta O_{\text{sys}}}{O-S-B}\right| + \left|\frac{\Delta S_{\text{sys}}}{O-S-B}\right| + \left|\frac{\Delta B_{\text{sys}}}{O-S-B}\right| + \left|\frac{\Delta F_{\text{sys}}}{F}\right|. \quad (8.8)$$

8.2.1 Systematic Uncertainty in S

In section 6.1.2 I discovered a bias in the scattered light estimated with the EFM method. For the tested synthetic images representing a month's worth of Co-add mode observations, the EFM method consistently underestimated the scattered light level. The bias is phase-dependent and results in relative systematic uncertainties in S in the range

$$5\% \leq \frac{\Delta S_{\text{sys}}}{S_{true}} \leq 80\% \quad (8.9)$$

where the largest relative errors are found for phases close to the New Moon. This large systematic error also means that I have underestimated the scattered light level when I listed typical precision error budget values in table 8.1. The scatter in the estimated scattered light remains small though, and changing S to a more realistic value of perhaps 0.7ADU in the dark side precision error budget, will not change any of the previous conclusions. The accuracy error budget is a different matter. With large relative systematic uncertainties I no longer expect the scattered light to be negligible.

8.2.2 Systematic Uncertainty in B

The periodic behaviour of the bias level is a source of a potential systematic error. I have described the periodic bias level in details in section 4.3. To prevent a systematic error we scale the superbias with the average bias level from two bias frames obtained just before and after the observation. If the time interval between the two bias frames is sufficiently short, the systematic uncertainty in bias is negligible. I found in equation (4.4) that the maximal error that can be introduced if the time interval is less than a minute is

$$\frac{\Delta B_{\text{sys}}}{B} \leq 0.006\% \quad (8.10)$$

8.2.3 Systematic Uncertainty in F

Flatfield correction of the observed images may introduce a systematic error, if the true flatfield has a different gradient than the master flatfield used in the data reduction. I investigated gradients in individual flatfields in section 5.4.2 for both lamp, twilight and dome flatfields. The lamp flatfields show the smallest gradient, with an intensity increase across the x-dimension of the CCD of 0.3% of the flatfield mean, and this is an upper limit on a possible intrinsic gradient.

We can choose to either keep the gradient in the lamp master flatfields or to subtract a surface fit, but in both cases we risk introducing a systematic error. In the worst case scenario, one end of the flatfield has 0.15% lower values than the true flatfield and the other end has 0.15% higher

values. I can therefore place an upper limit on the systematic uncertainty in the flatfield:

$$\frac{\Delta F_{\text{sys}}}{F} \leq 0.15\%. \tag{8.11}$$

The intercomparison of different types of flatfields has constrained the possible gradient in the true flatfield. If we manage to make good Moon flatfields (see section 5.1.4), we may be able to constrain the intrinsic gradient even further, thus lowering the systematic uncertainty in flatfield.

8.2.4 Systematic Uncertainty in O

The O-image is the raw observation frame, and it therefore contains information about the bias level, scattered light level and the flatfield. There are few possible systematic errors that cannot be said to originate from any of these components, but if such errors exist, they must be attributed to the O-image itself.

One such error source could be the presence of thin clouds across the field of view, covering the bright side and the dark side differently through an entire observation session. This is not a very likely scenario, since the clouds drift with the wind, and the Moon moves in its orbit, and the two movements are independent. Furthermore, the situation can be avoided if you only make use of observations from good photometric nights.

The relative photometry in Co-add mode ensures that time-like changes in extinction are not problematic. However, the Earthshine Telescope has an extended field of view of about 0.9°, so extinction may vary spatially across an image. Extinction depends on the air-mass and is therefore a function of zenith distance - meaning in principle, the extintion is lower in the upper end of the field of view and vice versa. Differential extinction is negligible for small zenith distances, but for air-masses above 2 it becomes necessary to correct for the differential extinction. An air-mass of 2 corresponds to a zenith distance of 60°, so to avoid this issue we should not observe the Moon when it is closer to the horizon than 30°. Since observations require the Sun to be below the horizon, the usable lunar phases are limited to those where the Moon is at least 30° away from the Sun - lunar phases below $|150^\circ|$.

In the following, I will assume the systematic uncertainty in O to be negligible.

8.2.5 Accuracy Error Budget, Dark Side

We have seen that the systematic uncertainty in scattered light is sensitive to lunar phase. This dependence will affect the error budget. In table 8.5, I have listed some typical dark side error budget values for two lunar phase angles separated with 40°, but both within the range appropriate for Co-add mode.

For smaller phase angles (ie. closer to Full Moon) the level of scattered light is higher, but the relative uncertainty in S is lower. At the same time the typical O-counts are lower, whereas the bias level and flatfield remain unchanged.

θ	O	S	ΔS_{sys}	B	ΔB_{sys}	F'	$\Delta F'_{\text{sys}}$
-140°	405	0.7	0.4	394.975	0.024	1	$1.5 \cdot 10^{-3}$
-100°	400	1.5	0.075				

Table 8.5: Typical dark side values for the systematic error budget in ADU, for the two lunar phase angles given in the first column. ΔS is from figures 6.5 and 6.6. ΔB is from eq. (4.4). ΔF is from table 5.3 and is relevant for a lamp master flatfield.

I have inserted the typical dark side values from table 8.5 in the error equation (8.8) to determine an upper bound on the relative uncertainty in intensity. The results for each of the phase angles are given in equations 8.12 and 8.13. Note that the accuracy error budgets takes a slightly different form than the precision error budgets (tables 8.2 and 8.4), this time giving the absolute contributions from the different terms (as opposed to the relative contributions).

$$\begin{aligned} \frac{\Delta I_{\text{sys}}}{I} &\leq \left|\frac{\Delta S_{\text{sys}}}{O-S-B}\right| + \left|\frac{\Delta B_{\text{sys}}}{O-S-B}\right| + \left|\frac{\Delta F_{\text{sys}}}{F}\right| \\ 4.69\% &\leq 4.290\% + 0.254\% + 0.15\% \quad , \quad \theta = -140^\circ \qquad (8.12) \\ 2.95\% &\leq 2.128\% + 0.672\% + 0.15\% \quad , \quad \theta = -100^\circ \qquad (8.13) \end{aligned}$$

The dark side systematic relative uncertainty in intensity is of the order of several percent with the scattered light being the main culprit. The science objective of the Earthshine Telescope is a *precision* of 0.1% in long-term albedo measurements. Unfortunately this is not a free-pass to the accuracy requirements, in fact the accuracy must be of the same order of magnitude as the precision requirements or preferably lower.

There are a few exceptions to the above rule. As mentioned in section 3.1, a systematic error in the form of a constant bias is of little concern in the context of measuring relative albedo changes. There is also the possibility that systematic errors from different sources but with opposite signs, cancel each other. Alternatively, if the sign of a systematic error from a specific source is random, then the systematic effect will cancel over many observations. For example the systematic errors arising from the periodic bias level are expected to have alternating signs. The largest error that can be introduced is when the temperature of the CCD is at an extremum at the time of the observation, and we as a result either underestimate or overestimate the bias level in single exposures.

The systematic error related to the scattered light does not fit the above exceptions, but as mentioned in section 6.1.2 there may be a way around the problem: If we can show that the systematic error from the scattered light always has the same sign (as it appears to have) and the same magnitude at a given phase, then we can adjust the amount of scattered light that we remove from the science frames.

The error budgets in equations 8.12 and 8.13 show that scattered light removal is an important task and a difficult challenge when measuring earthshine intensities. More work is needed on the fitting routine in the

EFM method, as this can possibly solve the problem. Alternatively, we can work on improving the halo model. The signal-to-noise image in figure 8.1 clearly shows the existence of problematic areas where the halo model is a poor fit to the halo in real observations.

It is worth noting in equations 8.12 and 8.13 that all the terms are above 0.1%. Even though scattered light removal is the major task ahead for the Lund-DMI group, the other terms should not be forgotten. They will become increasingly important as the methods for removing scattered light are improved.

The second most important source of systematic error on the dark side is the periodic bias level. With many observations the systematic effect is expected to cancel, but the bias-term can also be reduced with a smaller time interval between the two bias frames used to scale the superbias. Keeping all values intact from equation 8.12 except for the systematic uncertainty in B, I can set a new upper limit for the time interval

$$\frac{\Delta B_{\text{sys}}}{O-S-B} \leq 0.08\% \quad \Rightarrow \quad \frac{\Delta B_{\text{sys}}}{B} \leq 0.002\% \tag{8.14}$$

$$\Rightarrow \quad t_{\max} \leq 19 \text{ seconds.} \tag{8.15}$$

With a combination of many observations and smaller time intervals between bias frames, it is not impossible to reduce ΔB_{sys} below the precision requirement.

8.2.6 Accuracy Error Budget, Bright Side

Typical values for the error budget for the moonlight intensities are listed in table 8.6. Again the B and F' values are the same as for the dark side, and scattered light is negligible. The O counts are not phase dependent since the exposure times are adjusted so the bright side is always well-exposed with the highest pixel values being close to saturation.

O	B	ΔB_{sys}	F'	$\Delta F'_{\text{sys}}$
40000	394.975	$6 \cdot 10^{-5}$	1	$1.5 \cdot 10^{-3}$

Table 8.6: Typical bright side values for the systematic error budget in ADU.

I have inserted the typical bright side values from table 8.6 in the error equation (8.8) to determine an upper bound on the relative uncertainty in intensity. The result is

$$0.15\% \leq 6 \cdot 10^{-5}\% + 0.15\%. \tag{8.16}$$

On the bright side of the Moon the major contributor to the systematic uncertainty in intensity is the low-frequency pattern in the flatfield. The flatfield term in the error equation (8.8) only depends on the flatfield itself, and is therefore not reduced with increasing signal. If the other sources of systematic errors are reduced below the 0.1% level, then the flatfield will become the dominant systematic error on both the bright side of the Moon and on the dark.

There is no easy fix for systematic error in flatfield. Systematic errors cannot be reduced by averaging as is the case for random errors, and a wrong gradient in the flatfield does not fall into any of the exceptions. An intrinsic gradient in the flatfield is of course constant, but the effect of a wrong gradient on the intensity ratio is not. The effect of the gradient is to artificially increase or decrease the intensity ratio. But depending on the lunar phase, the bright and dark sides of the Moon covers different and even opposite parts of the CCD.

If the ultimate goal is a precision of 0.1% in the ratio of earthshine to moonlight, then the gradient of the true flatfield will need to be better constrained.

Chapter 9

Conclusion

The Lund-DMI Earthshine Telescope is designed to study the ratio of earthshine to moonlight intensities, a quantity that is proportional to the terrestrial albedo. The aim of this master thesis has been to photometrically characterize the new telescope system. I have focused my efforts on setting up an error budget for the earthshine and moonlight intensities that is relevant for the operational mode of the telescope which is currently in use - the Co-add mode.

The aim of the Earthshine Telescope project is to acquire long-term albedo data with a precision of about 0.1%. In order to achieve this goal the precision of the intensity ratio must be of the same order of magnitude or less. Preferably the accuracy should be reduced to similar values.

I have shown that we can reach the required level of precision in the intensity ratio of 0.1%. On the dark side of the Moon the main contributor to the error is photon noise, and on the bright side the uncertainty in flatfield becomes dominant, when we average over several pixels.

Furthermore I have shown that the systematic uncertainty in intensity is up to a few percent. It should be noted that this is an upper limit. It is the imperfect removal of scattered light that is responsible, and more work is needed in this area. On the bright side the flatfield is the dominant source of systematic uncertainty.

Appendix A

Earthbased Albedo Determination

A.1 Lunar Phase-function

Reference	Type	Project	λ	Phase range
Hapke [1963, 1966]	T	-	-	$5^\circ < \theta < 90^\circ$
Qiu et al. [2003]	G	BBSO	VIS	$5^\circ < \theta < 150^\circ$
Kieffer and Stone [2005]	G	ROLO	VIS-NIR	$5^\circ < \theta < 90^\circ$
Buratti et al. [2008]	G	ROLO	VIS-IR	$5^\circ < \theta < 90^\circ$
Holsclaw et al. [2010]	S	SOLSTICE	UV	$5^\circ < \theta < 170^\circ$
Hapke et al. [2012]	S	LRO	UV-VIS	$\theta < 120^\circ$

Table A.1: Important references for the lunar disc equivalent albedo (phase-function of the Moon). The list is not exhaustive. The letters in the column Type stands for, T: Theoretical model, G: Ground-based observations, S: Satellite observations. The latest satellite observations extend to the smallest angles. This is good news for earthshine measurements, since earthshine is always observed at $\theta < 1^\circ$. The Hapke models from the sixties also extend to zero phase angle, but at the time there didn't exist any observations to compare with for the smallest angles, and the models should not be trusted below 5°.

Appendix B

Bias

B.1 My Program: superbias.pro

```
1  ; superbias.pro: Creates a superbias with the mean half median
2  ; method and an array with the temporal standard deviations.
3  ;
4  ;-------------------------------------------------------------------
5  ; Necessary program input:
6  ; The file list_fitsfiles.txt and the previous best
7  ; superbias.fits must be present in the same folder as
8  ; this program.
9  ;
10 ; list_fitsfiles.txt is a list of filepaths to the bias
11 ; frames.
12 ;
13 ; Program output: superbias.fits and
14 ; sigma_array_w_halfmedianfilter.fits
15 ;-------------------------------------------------------------------
16
17
18 ; Create pixel-index array (because of memory issues)
19 pixel_1 = [[0,127,0,127],$
20           [0,127,128,255],$
21           [0,127,256,383],$
22           [0,127,384,511]]
23 pixel_2 = [[128,255,0,127],$
24           [128,255,128,255],$
25           [128,255,256,383],$
26           [128,255,384,511]]
27 pixel_3 = [[256,383,0,127],$
28           [256,383,128,255],$
29           [256,383,256,383],$
30           [256,383,384,511]]
31 pixel_4 = [[384,511,0,127],$
```

```
32            [384,511,128,255],$
33            [384,511,256,383],$
34            [384,511,384,511]]
35 pixel = [[pixel_1],$
36          [pixel_2],$
37          [pixel_3],$
38          [pixel_4]]
39
40 ; Create empty 512x512 superbias and sigma array
41 superbias = FLTARR(512,512)
42 sigma_array = FLTARR(512,512)
43
44 ; Fetch previous best bias
45 bestbias = DOUBLE(READFITS('superbias.fits'))
46
47 ; Divide image-array/cube into smaller cubes and create 1/16
48 ; mean half median bias
49 for k = 0,15,1 do begin
50
51   ; Create integer for counting rejected frames
52   r = 0
53
54   ; Open text-file with list of bias-fits-files and create
55   ; string
56   OPENR, 1, 'list_fitsfiles.txt'
57   files = '␣'
58
59   ; Read first fits-file to string and create image-array/cube
60   READF, 1, files
61   im = DOUBLE(READFITS(files))
62
63   ; Choose correct pixel index
64   a = pixel(0,k)
65   b = pixel(1,k)
66   c = pixel(2,k)
67   d = pixel(3,k)
68
69   ; Choose 1/16 of image-array/cube
70   im_small = im(a:b,c:d,*)
71
72   ; Loop to go through all bias frames until end-of-file is
73   ; encountered.
74   while ~ EOF(1) do begin
75
76     ; Read fits-file to string and create data-cube
77     READF, 1, files
78     im = DOUBLE(READFITS(files))
79
80     ; Investigate if bias frame is too far from best bias
81     ; If not, add to im_small cube.
```

```
82    ; Loop, because some fits-files are cubes.
83    dimim = SIZE(im)
84    if dimim(0) EQ 2 then begin          ; Only 1 frame
85    nim = 1
86    endif
87    if dimim(0) EQ 3 then begin          ; More than 1 frame
88    dimim_b = SIZE(im, /DIM)
89    nim = dimim_b(2)
90    endif
91    for m = 0, nim-1, 1 do begin
92      diff = im(*,*,m)-bestbias
93      mean_diff = AVG(diff)
94      if mean_diff LT 10 AND mean_diff GT -10 then begin
95        im_small = [[[im_small]],[[ im(a:b,c:d,m) ]]]
96      endif else begin
97        print, 'biasframe rejected'
98        r = r + 1
99      endelse
100   endfor
101
102 endwhile
103
104 ; Investigate number of frames
105 ndimim = SIZE(im_small, /DIM)
106 nframes = ndimim(2)
107
108 ; Create empty 128x128 small superbias array and stdev array
109 superbias_small = FLTARR(128,128)
110 sigma_small = FLTARR(128,128)
111
112 for i = 0, 127, 1 do begin
113   for j = 0, 127, 1 do begin
114
115     ; Create nframes vector for each pixel in order to sort
116     x = im_small(i,j,0:nframes-1)
117
118     ; Sort values in pixel-vector x
119     y = x(sort(x))
120
121     ; Select the half median values
122     y = y(nframes*0.25:nframes*0.75)
123
124     ; Find the mean pixel value and standard error
125     z = mean(y)
126     sd = stddev(y)
127
128     ; Allocate the mean pixel value to the small superbias
129     superbias_small(i,j) = z
130     sigma_small(i,j) = sd
131
```

```
132     endfor
133   endfor
134
135   ; Allocate the small superbias to correct position
136   superbias(a:b,c:d) = superbias_small
137   sigma_array(a:b,c:d) = sigma_small
138
139   ; Close file, to start reading from top
140   CLOSE, 1
141
142 endfor
143
144 print, r, ' biasframes were rejected.'
145
146 fits_write, 'superbias.fits', superbias
147 fits_write, 'sigma_array_w_halfmedianfilter.fits', sigma_array
148
149 END
```

Appendix C

Flatfields

C.1 My Program: masterflat.pro

```
1  ; masterflat.pro: Creates a master flatfield for each of the five colour
2  ; filters from a flatfield session.
3  ;
4  ;-------------------------------------------------------------------------
5  ; Necessary program input:
6  ; The files good_mean_flats_*.txt and darks_*.txt must be present
7  ; in the folder of the night XXX.
8  ; Replace * with the filter names.
9  ;
10 ; good_mean_flats_*.txt is a list of filepaths to the flatfields in filter *
11 ; from night XXX that have undergone a quality test: well-exposed and no
12 ; shutter failure etc.
13 ;
14 ; darks_*.txt is a list of filepaths to the dark frames or bias frames that
15 ; have been obtained close in time to the flatfields of filter *. They will
16 ; be used to scale the flatfields. Note that the limits in line 85-95 need
17 ; to be adjusted depending on the type of flatfield, conditions of the night
18 ; etc. This should be automated at some point. The limits are used to select
19 ; the darks that ar closest in time to a given flatfield.
20 ;
21 ; Program output: XXX/master_*.fits
22 ;
23 ; Box of dialog, where the user manually types the last three digits XXX in
24 ; the Julian date of the night in question.
25 nat = DIALOG(/STRING, VALUE='XXX', 'Which night?')
26 ;-------------------------------------------------------------------------
27
28 ; Access the superbias
29 superbias = DOUBLE(READFITS('../BIAS/superbias/superbias.fits'))
30
31 ; Create correct filepaths as string-arrays.
```

```
filsti_flat = [nat + '/good_mean_flats_B.txt', $
  nat + '/good_mean_flats_V.txt', $
  nat + '/good_mean_flats_VE1.txt', $
  nat + '/good_mean_flats_VE2.txt', $
  nat + '/good_mean_flats_IRCUT.txt']
filsti_dark = [nat + '/darks_B.txt', $
  nat + '/darks_V.txt', $
  nat + '/darks_VE1.txt', $
  nat + '/darks_VE2.txt', $
  nat + '/darks_IRCUT.txt']
filsti_master = [nat + '/master_B.fits', $
  nat + '/master_V.fits', $
  nat + '/master_VE1.fits', $
  nat + '/master_VE2.fits', $
  nat + '/master_IRCUT.fits']

; Loop to go through each filter
for filter = 0,4,1 do begin

  OPENR, 1, filsti_flat[filter]

  ; Create empty strings
  flat_filepath = ''
  dark_filepath = ''

  ; Create integer counters and reset for each filter
  n_flats = 0
  n_darks = 0

  ; Loop to go through all flatfields until end-of-file is encountered.
  while ~ EOF(1) do begin
    n_flats = n_flats + 1                ; Count

    ; Access a flatfield
    READF, 1, flat_filepath
    flat = DOUBLE(READFITS(flat_filepath))
    ; Read Julian Date and Time 1.XXXXXXX from filename into a number
    jd = DOUBLE(STRMID(flat_filepath,44,52))
    print, jd

    ; Read darks_X.txt from top for each good_mean_flat_X
    OPENR, 2, filsti_dark[filter]
    ; Create empty 2D-array
    dark = FLTARR(512,512)
    ; Reset integer counter for each flatfield
    n_darks = 0
    ; Loop to go through all darkframes until end-of-file is encountered.
    while ~ EOF(2) do begin

      READF, 2, dark_filepath
```

```
82        ; Read Julian Date and Time 1.XXXXXXX from filename into a number
83        jd_dark = DOUBLE(STRMID(dark_filepath,44,52))
84
85        ; Find appropriate darks
86        if filter EQ 0 then begin
87          limit = 2e-3
88        endif else begin
89          limit = 5e-4
90        endelse
91        limit = 1e-4       ; Normal limit for skyflats
92        if ABS(jd_dark - jd) LT limit then begin
93          dark = [[[dark]],[[DOUBLE(READFITS(dark_filepath))]]]
94          n_darks = n_darks + 1    ; Count
95        endif
96
97      ; End of dark loop
98      endwhile
99      CLOSE, 2
100
101     ; Check number of darks
102     if n_darks EQ 0 then begin
103       print, 'There are no appropriate darks for flatfield at time ', jd
104       n_flats = n_flats - 1
105     endif else begin
106       ; Remove empty top 2D-array from the stack dark
107       dark = dark[*,*,1:*]
108       ; Scale superbias using the appropriate darks
109       scaled_superbias = superbias * (AVG(dark)/AVG(superbias))
110
111       ; Subtract scaled superbias from flatfield
112       flat = flat - scaled_superbias
113
114       ; Determine gradient to be removed
115       fit_flat = SFIT(flat,2)
116
117       ; Normalize bias-subtracted flatfield
118       flat_norm = (flat - fit_flat + AVG(fit_flat)) / $
119                   AVG(flat - fit_flat + AVG(fit_flat))
120       ; Display surface plot of the individual normalized flatfields
121       SURFACE, flat_norm, CHARSIZE = 2
122
123       ; Read normalized bias-subtracted flatfield to datacube.
124       if n_flats EQ 1 then begin
125         flat_norm_cube = flat_norm
126       endif else begin
127         flat_norm_cube = [[[flat_norm_cube]],[[flat_norm]]]
128       endelse
129
130     endelse
131   ; End of flatfield loop
```

```
132   endwhile
133
134   CLOSE, 1
135
136   ;-------------------------------------------------------------------------
137   ;----------------Create masterflat from flat_norm_cube--------------------
138   ;-------------------------------------------------------------------------
139
140   ; Check if there are any flatfields or darkframes for the filter
141   if n_flats EQ 0 then begin
142     print, 'There are either no flatfields or dark-frames for filter', filter
143     print, 'No masterflat created for filter'
144   endif else begin
145
146     ; Create empty array for the masterflat
147     master_flat = FLTARR(512,512)
148     sigma = FLTARR(512,512)
149
150     for i = 0, 511, 1 do begin
151       for j = 0, 511, 1 do begin
152
153         ; Create nframes vector for each pixel in order to sort
154         x = flat_norm_cube(i,j,0:n_flats-1)
155
156         ; Sort values in pixel-vector x
157         y = x(SORT(x))
158
159         ; Select the half median values
160         y = y(n_flats*0.25:n_flats*0.75)
161
162         ; Find the mean pixel value and standard error
163         z = AVG(y)
164         sd = STDDEV(y)
165
166         ; Allocate the mean pixel value to the masterflat
167         master_flat(i,j) = z
168         sigma(i,j) = sd
169
170       endfor
171     endfor
172
173     ; Write master flatfield for filter * to file XXX/master_*.fits
174     fits_write, filsti_master[filter], master_flat
175
176   endelse
177 ; End of filter loop
178 endfor
179
180 END
```

C.2 Master Flatfields

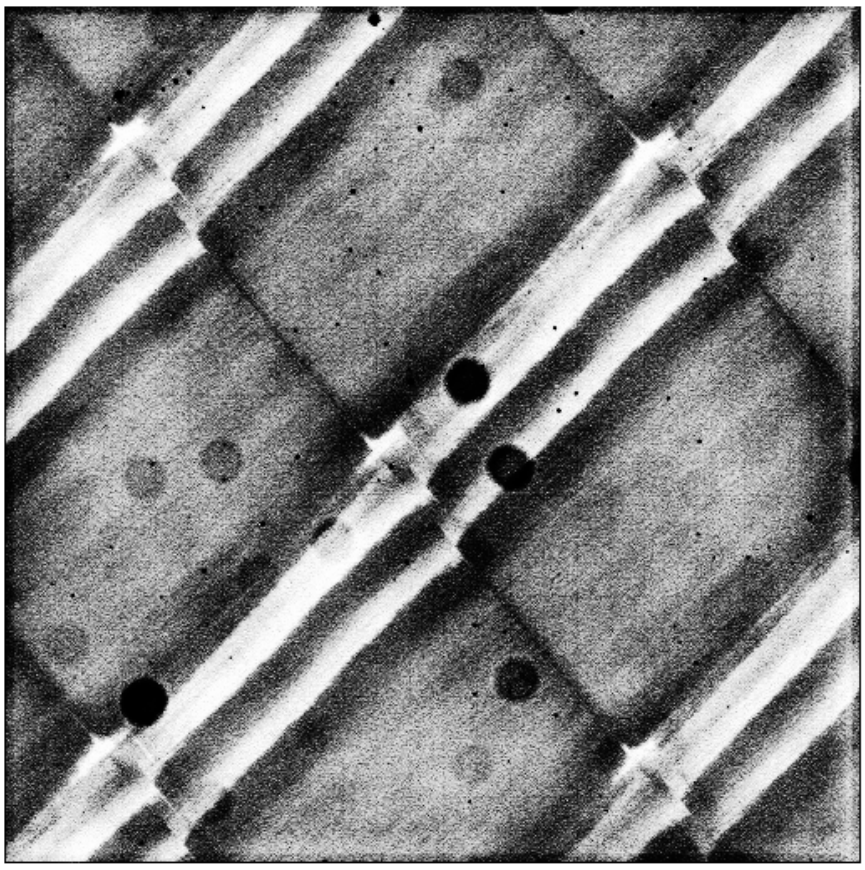

Figure C.1: B-filter twilight master flatfield, dusk-session night JD2455827.

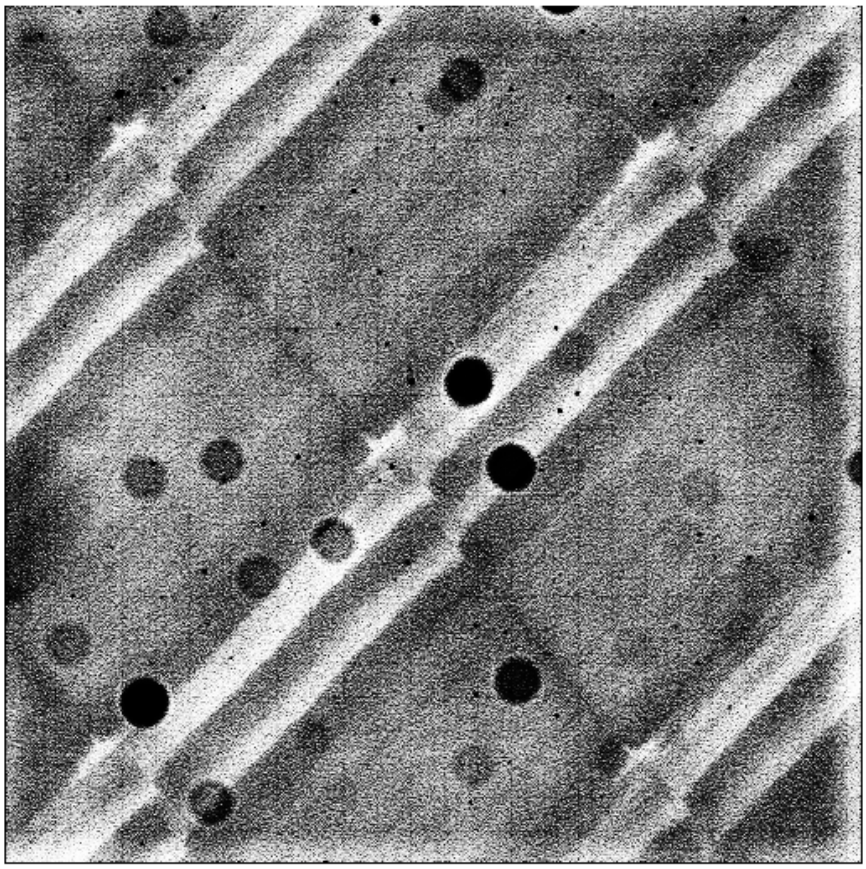

Figure C.2: V-filter twilight master flatfield, dusk-session night JD2455827.

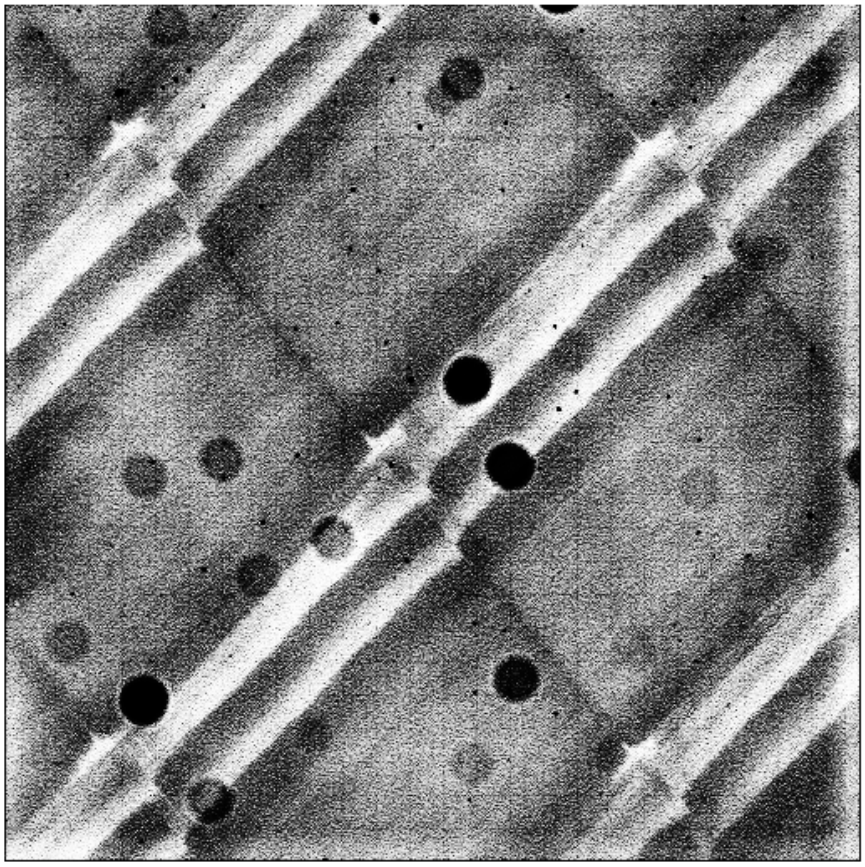

Figure C.3: VE1-filter twilight master flatfield, dusk-session night JD2455827.

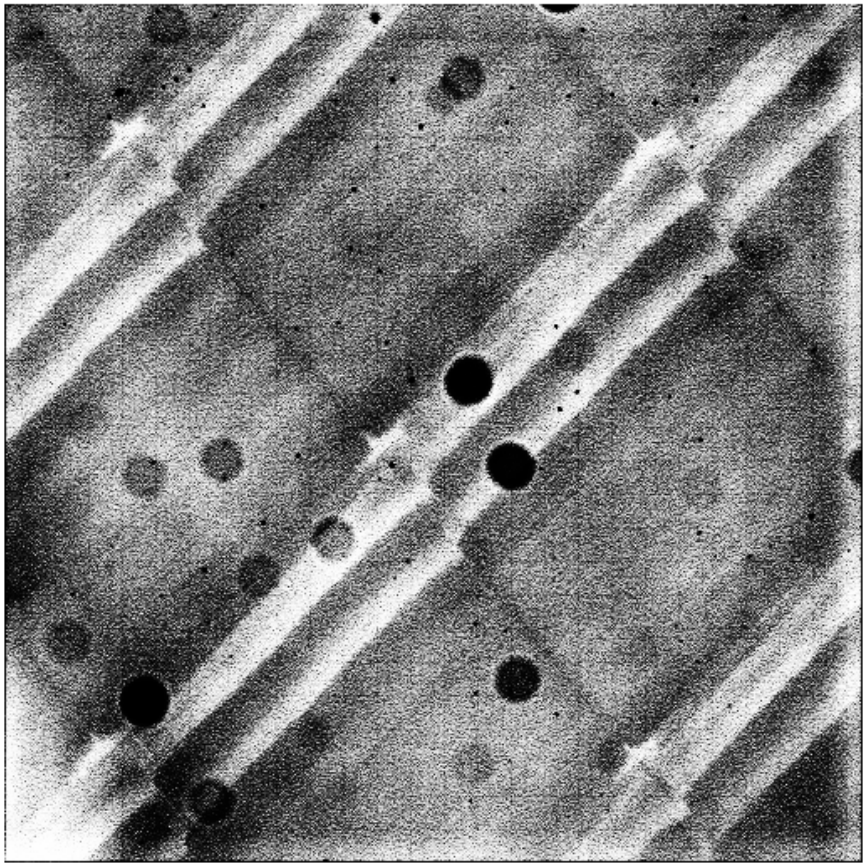

Figure C.4: IRCUT-filter twilight master flatfield, dusk-session night JD2455827.

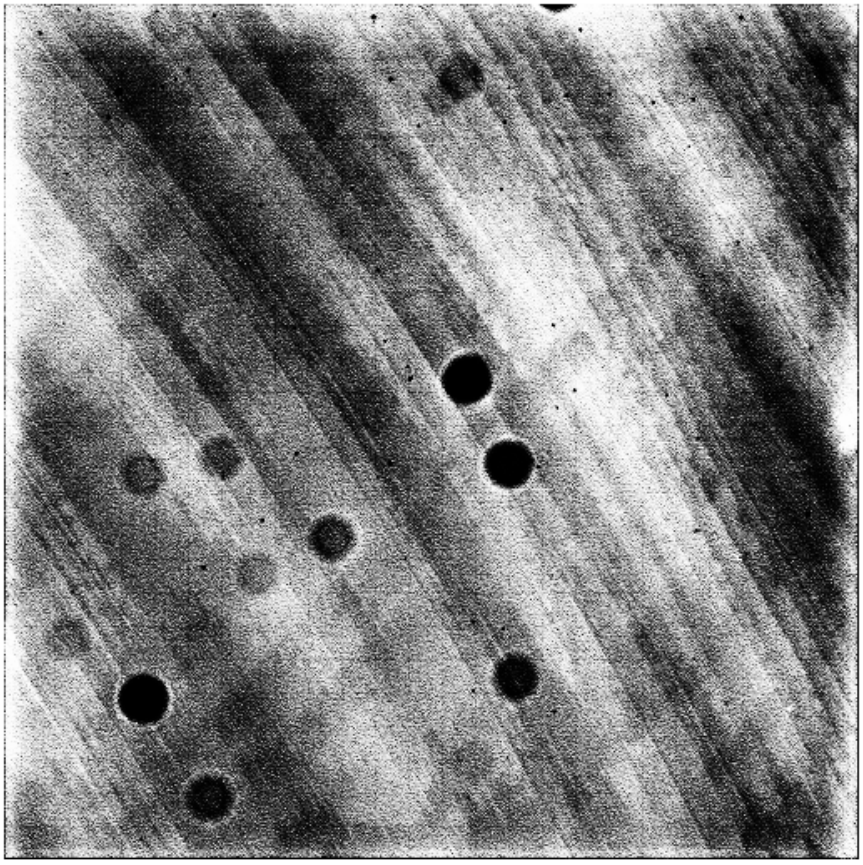

Figure C.5: VE2-filter twilight master flatfield, dusk-session night JD2455827.

Filter	Bright Diagonal Feature	σ [ADU]
B	$1-2\%$ of mean	0.0075
V	0.5% of mean	0.0047
IRCUT	0.6% of mean	0.0048
VE1	0.6% of mean	0.0047
VE2	0.2% of mean	0.0047

Table C.1: Twilight master flatfields dusk-session JD 2455827. The strength of the bright diagonal features for the different filters and the standard deviation of the master flatfields. The mean value of all master flatfields is 1, since they have been normalized. The diagonal pattern is clearly wavelength dependent, being strongest in blue wavelengths and weakest in near-infrared wavelengths. Because flatfields are wavelength dependent, it is necessary in the image reduction to use a flatfield with the same filter as the object image.

Position	# of pixels	Count
(68,459)	8	0.54
(481,206)	3	0.65
(221,504)	3	0.72
(441,503)	2	0.8
(242,287)	2	0.89
(231,466)	1	0.85
(119,174)	1	0.86
(439,369)	1	0.87
(412,455)	1	0.89
(345,496)	1	0.89

Table C.2: Positions and values of the most severe bad pixels and groups of bad pixels in the IRCUT master flatfield from JD 2455827. The selection criteria is pixels with values lower than 0.9 (10% lower than the mean of the master). There are 10 groups with a total of 23 pixels. The positions are zero-indexed (column,row) with starting point in the lower left corner of figure 5.3. Column 3 gives the lowest count in a group of bad pixels.

C.2.1 Wavelength Dependence

Table C.3 displays the depth at which 90% of incident photons of a given wavelength are absorbed by a typical CCD.

$\lambda\ [nm]$	400	450	500	600	700	800	900	1000	1100
depth$[\mu m]$	0.19	1.0	2.3	5.0	8.5	23	62	470	7600

Table C.3: Photon absorption depth in silicon for 90% of incident photons. Because the photon absorption depth is wavelength dependent, variations in CCD thickness will influence the pixel sensitivity differently for different wavelengths. The wavelength dependent part of the flatfield structure may thus be a result of non-uniform CCD thickness.

The relatively narrow B-filter has a central wavelength of 435.3nm, and a 50% bandwidth of 90.90nm [Darudi and Badínez, 2011] (see figure 2.5 for filter transmission curves). The photons transmitted through this filter have a short mean free path compared to the 15μm thickness of the CCD. The blue photons are therefore converted to electrons immediately after entering the backside of the CCD. Even though the CCD has been thinned, the path for the photoelectrons is still long to the possible detection at the front-side. Even small variations in the CCD thickness influence the amount of the photoelectrons that are detected. This is why we see a stronger pattern in the B-filter master flatfield. The slightly thinner areas of the CCD will be brighter than the rest because more photoelectrons are detected.

The other filters are less sensitive to variations in thickness. The V-filter is, like the B-filter, quite narrow with a 50% bandwidth of 85.41nm, but with a central wavelength of 533.67nm coinciding with the peak in quantum efficiency for the CCD (see figure 2.6 of the QE), this filter is much less sensitive to the variations. The remaining three filters are much broader, with IRCUT and VE1 covering the wavelength region from about 380nm to 750nm and VE2 the region from 750nm and longer, effectively being limited by the quantum efficiency of the CCD at around 1000nm. The IRCUT-filter and the VE1-filter include both blue thickness-sensitive photons and red photons. The result is a total sensitivity less pronounced than for the B-filter.

The VE2-filter, on the other hand, only transmits near-infrared photons. One might expect that these longwave photons would be less likely to be detected in the slightly thinner areas of the CCD, so that the bright diagonal lines seen in the B master would be dark in the VE2 master. However, this is not the case. The same areas are still brighter than their surroundings even if the pattern is hardly discernible in this filter.

C.3 Individual Flatfield Comparison

Two flatfields in the same filter and from the same twilight session are compared with a percent difference image. Each flatfield is bias subtracted with the proper scaled superbias, then has a fitted surface subtracted to remove any gradient and is finally normalized.

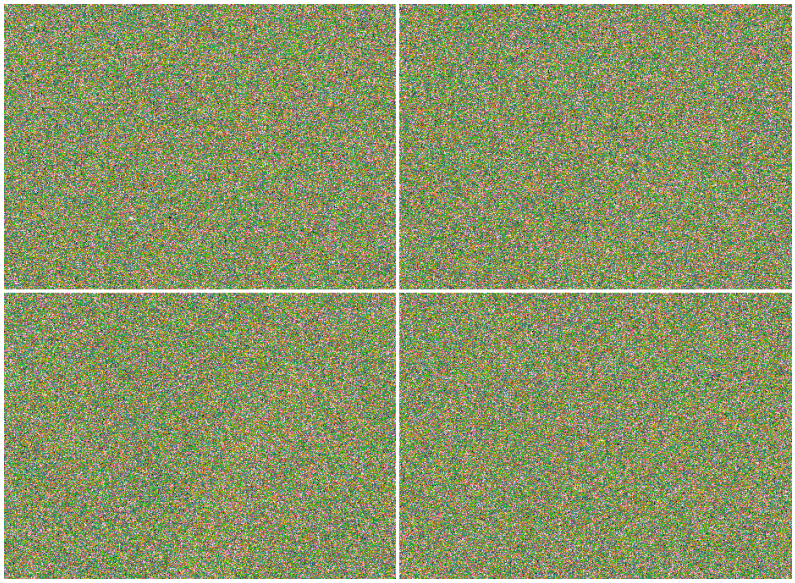

Figure C.6: Percent difference images from flatfield session JD 2455831. **Left to right:** IRCUT Δt 13.6min, VE1 Δt 6.5min, VE2 Δt 5.4min, V Δt 0.7. The images have been histogram equalized and coloured to emphasize that there is no discernible structure.

filter	Δt [min]	mean [%]	stddev [%]	Corr coeff
V	0.7	0.003	0.7	0.42
IRCUT	13.6	0.0009	0.6	0.58
VE1	6.5	0.002	0.7	0.42
VE2	5.4	0.001	0.5	0.63

Table C.4: Comparison between pairs of flatfields from the same session (JD 2455831) and with the same filter (given in the first column). The second column gives the time period in between the two flatfields, the third and fourth columns are the mean and the standard deviation of a percent image, and the fifth column is the correlation coefficient of the two flatfields. There were no well-exposed B flatfields for this particular session. The filter pairs with lowest correlation (V and VE1) have flatfields with low average counts in the range $10,000 - 13,000$, whereas the VE2 flatfields have average counts in the range $18,000 - 22,000$, and the IRCUT flatfields have average counts in the range $23,000 - 35,000$. This indicates that as long as flatfields are well-exposed, the individual flatfields that are used to construct a master flatfield are very similar.

filter	Δt [min]	mean [%]	stddev [%]	Corr coeff
B	5.7	0.002	0.6	0.76
B	6.6	0.002	0.6	0.76
V	13.7	0.003	0.6	0.50
IRCUT	0.4	0.001	0.4	0.70
VE1	14.1	0.004	0.7	0.55
VE1	6.5	0.004	0.7	0.50
VE2	15.0	0.02	1.4	0.18
VE2	8.3	0.001	0.5	0.67

Table C.5: Same as table C.4, but for flatfield session JD 2455827. Flatfields observed in the B-filter correlate strongly with each other, and all flatfield pairs (except for the one involving a low S/N flatfield in VE2) correlate well with each other.

C.4 Master Flatfield Comparison

Percent difference images between pairs of twilight master flatfields. Here the full percent images are shown in linear grey-scale.

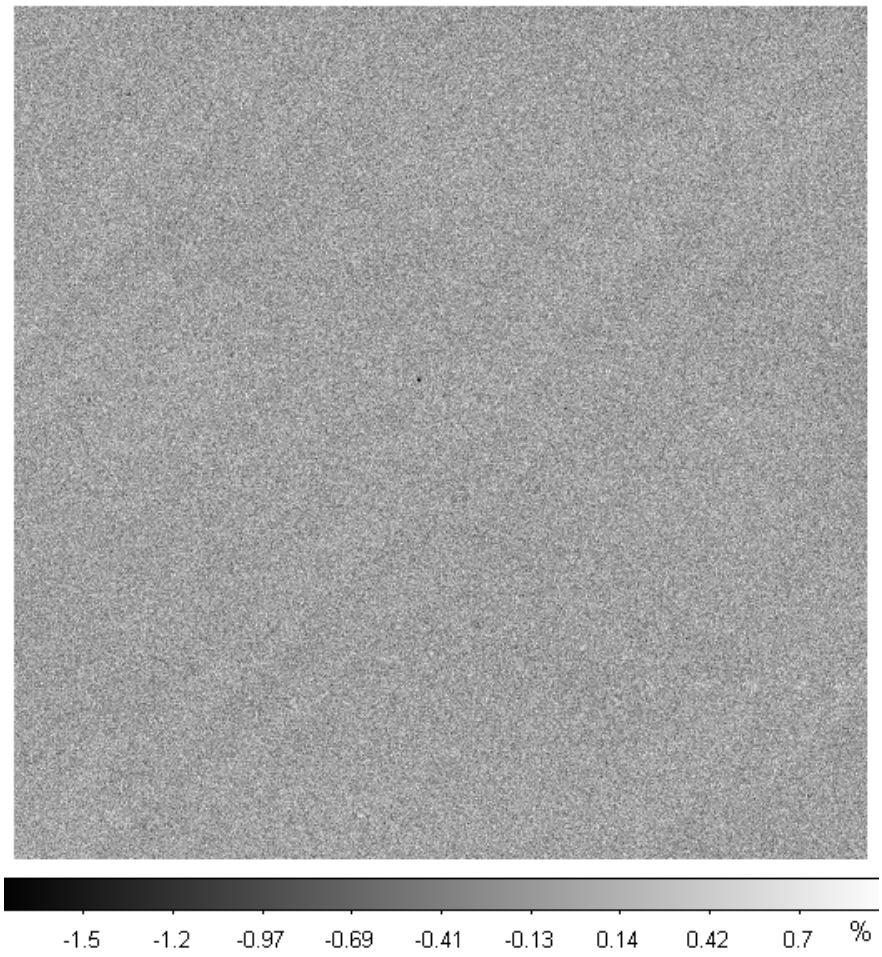

Figure C.7: Percent difference image in the B-filter between twilight master flatfields from JD 2455825 and JD 2455827. There is an obvious bad pixel remnant roughly in the center.

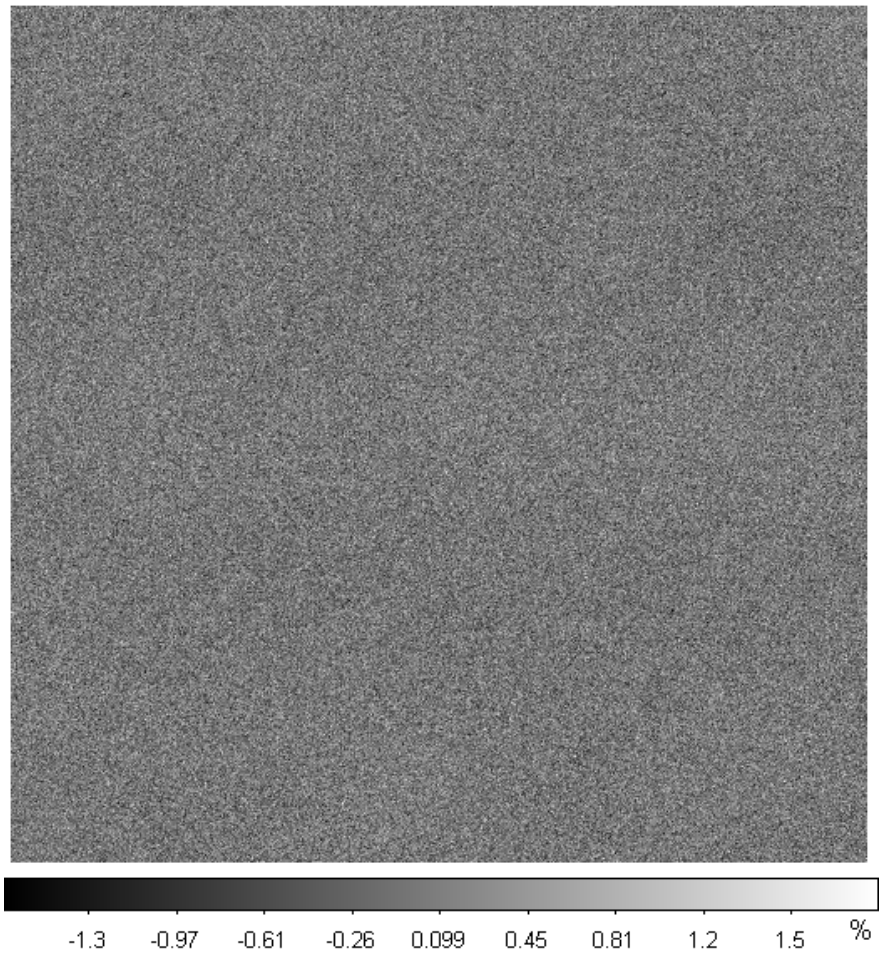

Figure C.8: Percent difference image in the V-filter between twilight master flatfields from JD 2455827 and JD 2455831. There were only two flatfields in the V-filter from night JD 2455831, and this doesn't represent a master flatfield well. This is probably the reason why the percent differences are higher for this filter than the others.

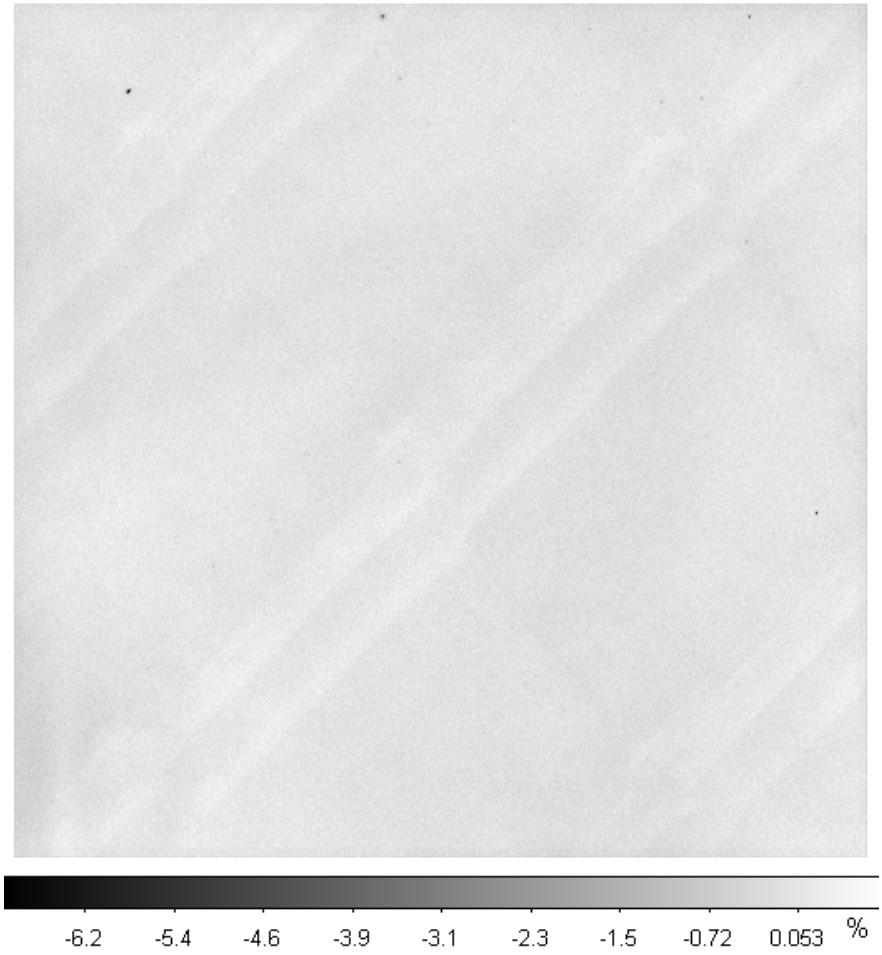

Figure C.9: Percent difference image in the IRCUT-filter between twilight master flatfields from JD 2455827 and JD 2455831. Some of the bad pixels close to the edge of the frame can still be seen.

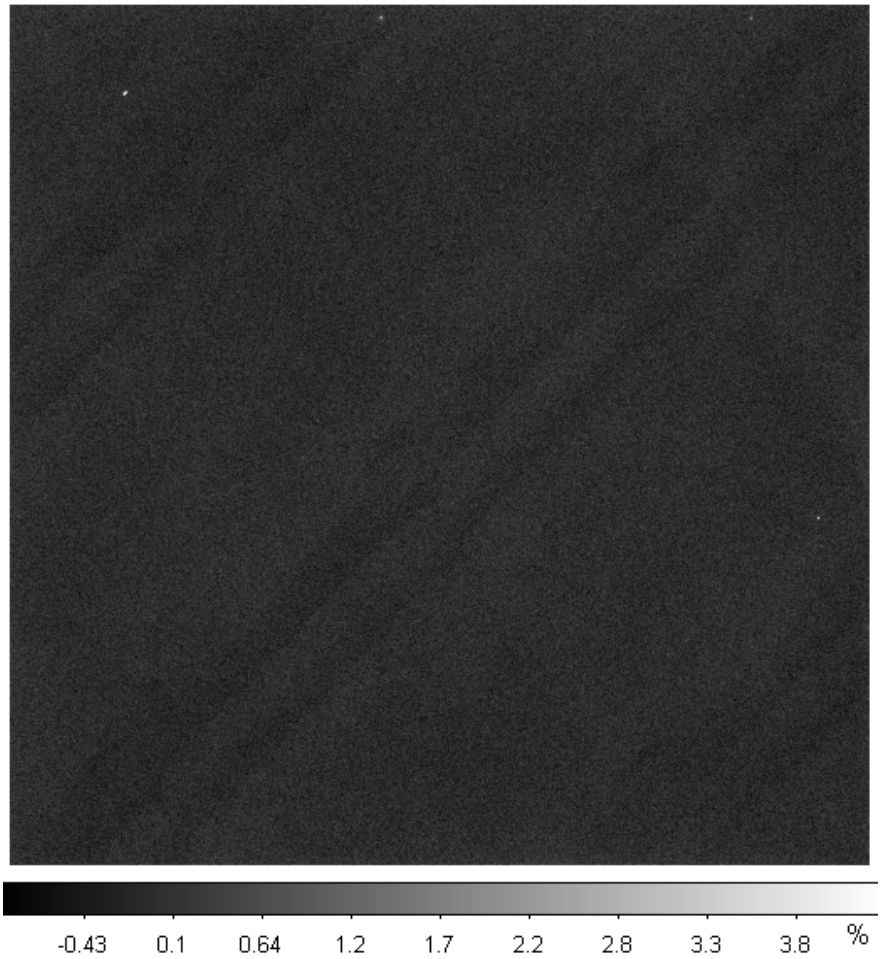

Figure C.10: Percent difference image in the VE1-filter between twilight master flatfields from JD 2455825 and JD 2455827. Some of the bad pixels close to the edge of the frame can still be seen.

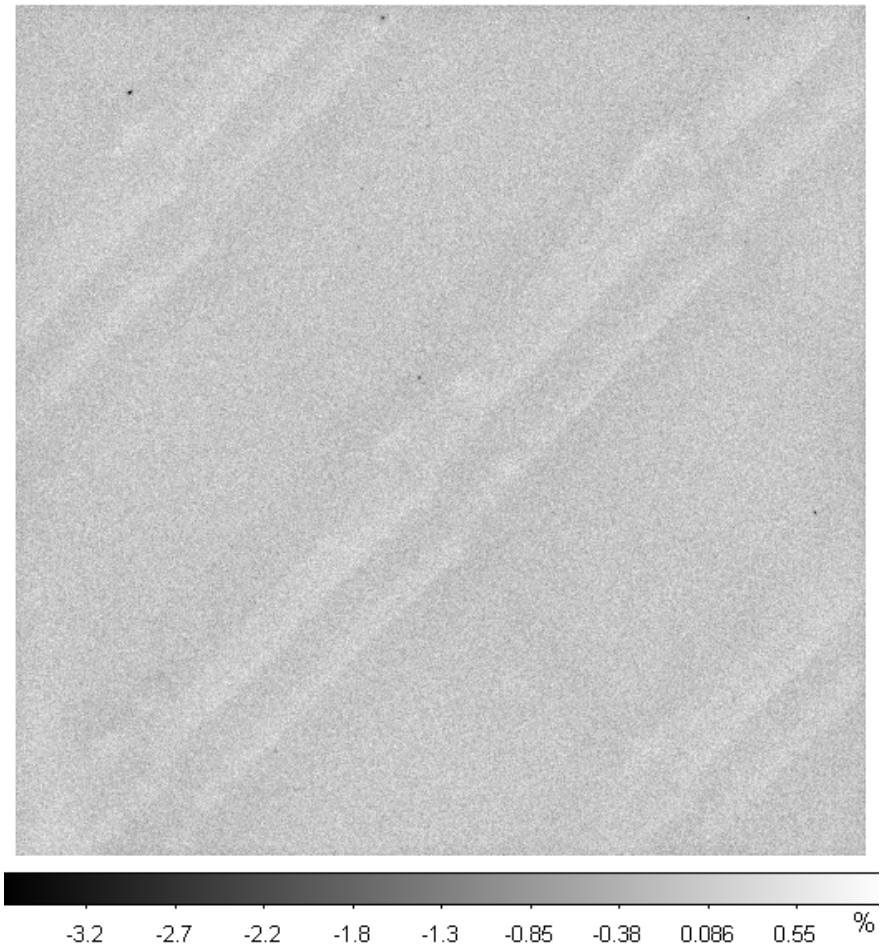

Figure C.11: Percent difference image in the VE1-filter between twilight master flatfields from JD 2455825 and JD2455831. Some of the bad pixels close to the edge of the frame and the central one can still be seen.

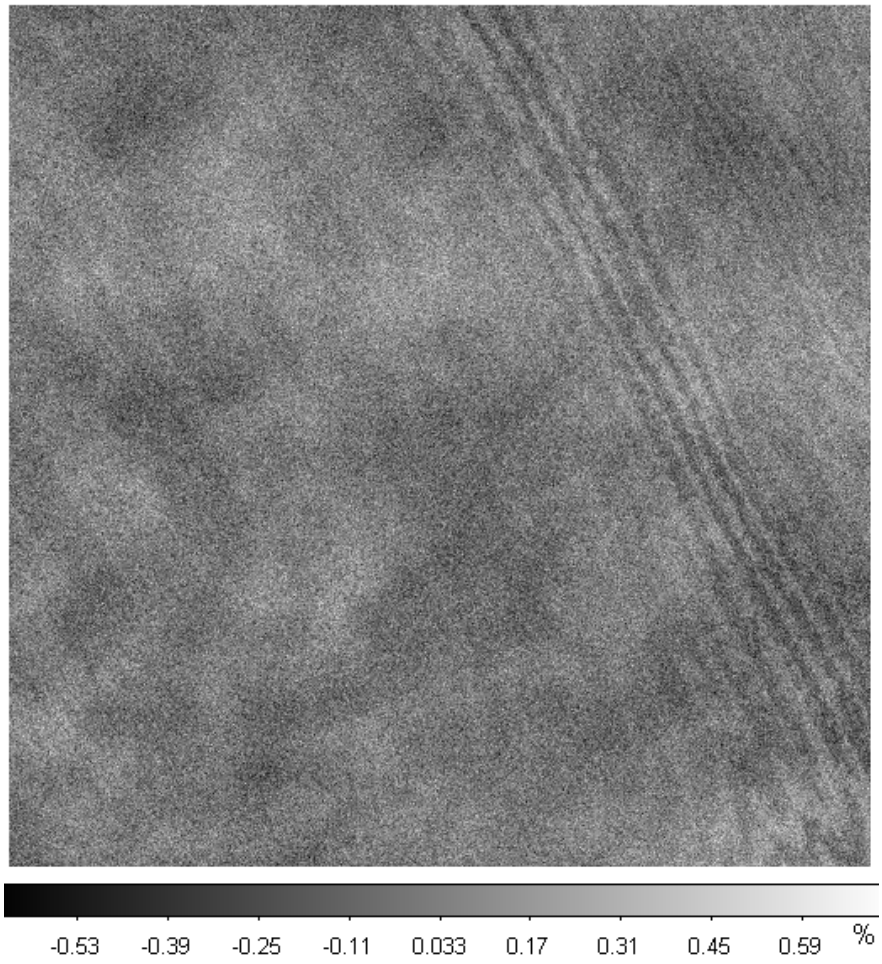

Figure C.12: Percent difference image in the VE2-filter between twilight master flatfields from JD 2455827 and JD 2455831.

Filter	JD 2455XXX	JD 2455XXX	Mean	σ
B	825	827	-0.036	0.24
V	827	831	-0.0003	0.39
VE1	825	827	-0.021	0.19
VE1	825	831	-0.0006	0.23
VE2	827	831	0.003	0.15
IRCUT	827	831	0.0001	0.18

Table C.6: Comparison of two twilight master flatfields in the same filter obtained on different nights. The time intervals range between two days and six days. The mean and the standard deviation of the percent difference image is given. The master flats for a given filter are generally very similar, so that the standard deviations of the percent images are below 0.25%.

Appendix D

Error Budget

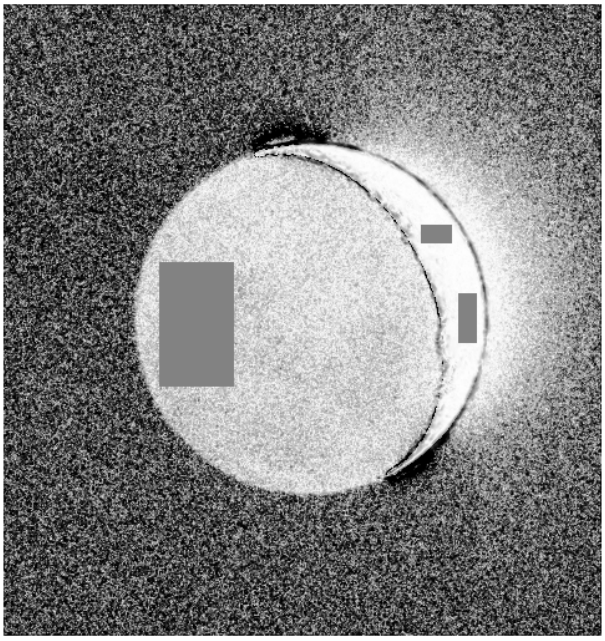

Figure D.1: The boxes that are used in section 8.1.5 to determine typical S/N values per pixel for both the dark side and the bright side. The dark side box covers 60x100 pixels, and the bright side boxes cover 25x15 and 15x40 pixels.

Bibliography

ANDOR website. ixon 897 camera. website. http://www.andor.com/scientific_cameras/ixon_emccd_camera/897_single-photon/.

L. Arnold. Earthshine observations of vegetation and implications for life detection on other planets. *Space Science Reviews*, 135:323, 2008.

J. Ashbrook. *The Astronomical Scrapbook, Skywatchers, Pioneers and Seekers in Astronomy*. Cambridge University Press, 1984.

K. Åström and A. Heyden. Stochastic Analysis of Image Acquisition, Interpolation and Scale-space Smoothing. *Advances of Applied Probability*, 1999.

R. Badínez. Photometric Evaluation and Calibration of the Earthshine Telescope. Master's thesis, Lund University, 2010.

G. A. Bakos. Measures of the earthshine. *SAO Special Report*, 162, 1964.

B. R. Barkstrom. The Earth Radiation Budget Experiment (ERBE). *BAMS*, 65:1170, 1984.

D. Briot. Earthshine observations and the detection of vegetation on extrasolar planets. In *Highlight of Astronomy, Volume 15*, page 699. International Astronomical Union, 2010.

B. J. Buratti, M. Staid, C. M. Pieters, M. D. Hicks, and T. S. Stone. A wavelength dependent visible and infrared spectrophotometric model for the Moon based on ROLO data. In *39th Lunar and Planetary Science Conference*, 2008.

K. R. Castleman. *Digital Image Processing*. Prentice Hall International, 1996. ISBN 0-13-398058-8.

J. Chae. IDL programs. website. http://www.bbso.njit.edu/\~chae/IDL/idl.html.

J. Chae. Flat-Fielding of Solar Hα Observations Using Relatively Shifted Images. *Solar Physics*, 221:1, 2004.

T. S. Chen and G. Ohring. On the relationship between clear-sky planetary and surface albedos: A parameterization for simple energy balance models. *AdSpR*, 5(6):141, 1985.

F. R. Chromey. *To Measure the Sky*. Cambridge University Press, 2010. ISBN 978-0-521-74768-4.

L. da Vinci. Codex leicester. website, ca. 1510. http://www.7oon.eu/leonardo/.

A. Danjon. Albedo, color, and polarization of the earth. In Kuiper, editor, *The earth as a planet*. University of Chicago Press, 1954. ISBN 978-9998357327.

A. Darudi and Badínez. Spectral analysis of the lund/dmi earthshine telescope and filters. Technical report, Lund University, 2011.

A. Darudi, M. Owner-Petersen, P. Thejll, H. Gleisner, D. Taylor, M. Ale-Ebrahem, and T. Andersen. The robotic earthshine telescope. In *Ground-based and Airborne Telescopes III*, volume 7733, page 88. SPIE, 2010.

J. Dubois. Sur l'albedo de la terre. *Bull. Astron.*, 13:193, 1947.

A. T. Evan, A. K. Heidinger, and D. J. Vimont. Arguments against a physical long-term trend in global isccp cloud amounts. *GeoRL*, 34(4):701, 2007.

S. Flatte, S. Koonin, and G. MacDonald. Global change and the dark of the moon. Final Report Mitre Corp, 1992. http://www.dtic.mil/dtic/tr/fulltext/u2/a255181.pdf.

F. A. Franklin. Two-color photometry of the earthshine. *J.Geophys.Res.*, 72: 2963, 1967.

Free Online Private Pilot Ground School. website. http://www.free-online-private-pilot-ground-school.com/Aviation-Weather-Principles.html.

P. R. Goode and E. Pallé. Shortwave forcing of the earth's climate: Modern and historical variations in the sun's irradiance and the earth's reflectance. *JASTP*, 69:1556, 2007.

P. R. Goode, J. Qiu, V. Yurchyshyn, and J. Hickey. Eartshine observations of the earth's reflectance. *GeoRL*, 28:1671, 2001.

P. R. Goode, S. Shoumko, E. Pallé, and P. Montañés-Rodríguez. Automated Observations of the Earthshine. *Advances in Astronomy*, 2010. article id. 963650.

B. Hapke. Theoretical Photometric Function of the Lunar Surface. *Astronomical Journal*, 68:279, 1963.

B. Hapke. An Improved Theoretical Lunar Photometric Function. *Astronomical Journal*, 71:333, 1966.

B. Hapke, B. Denevi, H. Sato, S. Braden, and M. Robinson. The wavelength dependence of the lunar phase curve as seen by the Lunar Reconnaissance Orbiter wide-angle camera. *JGRE*, 117:15, 2012.

J. Harries, J. E. Russell, J. A. Hanafin, H. Brindley, et al. The Geostationary Earth Radiation Budget Project. *BAMS*, 86(7):945, 2005.

G. Holsclaw, M. Snow, A. Hendrix, and W. McClintock. The LASP Lunar Albedo Measurement and Analysis from SOLSTIC (LLAMAS). In *41st Lunar and Planetary Science Conference*, 2010.

S. B. Howell. *Handbook of CCD Astronomy*. Cambridge University Press, 2000.

D. R. Huffman, C. Weidman, and S. Twomey. Repetition of danjon earthshine measurements for determination of long term trends in the earth's albedo. In *Journées 1990: Systemes de référence spatio-temporels. Colloque André Danjon*, page 111. Paris Observatory, 1990.

A. v. Humboldt. Cosmos, a sketch of a physical description of the universe, volume 4, 1852.

J. R. Kennedy. Master's thesis, Fresno State College, 1969.

H. H. Kieffer and T. C. Stone. The spectral irradiance of the Moon. *Astrnomical Journal*, 129:2887, 2005.

I. R. King. The Profile of a Star Image. *PASP*, 83:199, 1971.

M. D. King, C. L. Parkinson, K. C. Partington, and R. G. Williams, editors. *Our Changing Planet: The View from Space*. Cambridge University Press, first edition, 2007. ISBN 0-521-82870-3.

G. Kopp and J. L. Lean. A new, lower value of total solar irradiance: Evidence and climate significance. *GeoRL*, 38:L01706, 2011.

J. R. Kuhn, H. Lin, and D. Loranz. Gain calibrating nonuniform image-array data using only the image data. *PASP*, 103:1097, 1991.

Mauna Kea Weather Center. website. `http://mkwc.ifa.hawaii.edu/`.

K. McGuffie and A. Henderson-Sellers. *A Climate Modelling Primer*. Wiley, second edition, 1997. ISBN 0-471-95558-2.

P. McVarnock. Andor ixon perfomance sheet. Technical report, ANDOR Technology, 2010.

P. Montañés-Rodríguez and E. Pallé. The earthshine project: Applications to the search of exoearths. In *Pathways Towards Habitable Planets*, page 505. Astronomical Society of the Pacific, 2010.

R. Mossavati, J. E. Harries, S. Kellock, R. T. Wrigley, J. Mueller, and N. P. Fox. Radiometric calibration of the GERB instrument. *Metrologia*, 35:603, 1998.

M. V. Newberry. Pursuing the ideal flat field. *CCD Astronomy*, 3, No. 1:18, 1996.

C. Newhall, J. W. Hendley II, and P. H. Stauffer. U.s. geological survey fact sheet 113-97. website, 1997. `http://pubs.usgs.gov/fs/1997/fs113-97/`.

E. Öpik. Photometric measures on the moon and the earth-shine. *Publications de l'Observatoire Astronomique de l'Universite de Tartu*, 26, No.1, 1924.

E. Pallé, P. R. Goode, P. Montañés-Rodríguez, and S. E. Koonin. Changes in Earth's Reflectance over the Past Two Decades. *Science*, 304:1299, 2004.

E. Pallé, P. R. Goode, and P. Montañés-Rodríguez. Interannaul variations in earth's reflectance 1999-2007. *JGRD*, 114(9):D03, 2009.

F. Paulot, J. D. Crounse, K. A. Kjaergaard, H. G., J. M. St. Clair, J. H. Seinfeld, and P. O. Wennberg. Unexpected epoxide formation in the gas-phase photooxidation of isoprene. *Science*, 325:730, 2009.

J. Qiu, P. R. Goode, E. Pallé, V. Yurchyshyn, J. Hickey, and P. Montañés-Rodríguez. Earthshine and the earth's albedo i. *JGRD*, 108:4709, 2003.

H. N. Russell. On the albedo of the planets and their satellites. *ApJ*, 43, 1916.

G. L. Smith, B. A. Wielicki, B. R. Barkstrom, R. B. Lee, et al. Clouds and Earth radiant energy system: an overview. *AdSpR*, 33(7):1125, 2004.

C. W. Stubbs, P. Doherty, and A. H. Diercks. Method for extending the dynamic range of ccd instruments. In *Solid State Sensor Arrays: Development and Applications II*, volume 3301, page 75. SPIE, 1998.

P. Thejll. 04-18: An automatic earthshine telescope. Technical report, Danish Meteorological Institute, 2004.

P. Thejll. Jd2455923. Earthshine blog, 2011a. `http://earthshine.thejll.com/\#post114`.

P. Thejll. Sunglint map. Earthshine blog, 2011b. `http://earthshine.thejll.com/\#post66`.

P. Thejll and H. Gleisner. Kan jordens klima ses på månen? *KVANT*, 18:3, 2007.

P. Thejll, C. Flynn, H. Gleisner, and A. Mattingly. Earthshine: not just for romantics. *AG*, 49:3.15, 2008.

P. Thejll, H. Gleisner, T. Andersen, A. Darudi, M. Owner-Petersen, H. Schwarz, and J. W. Poulsen. Comparing methods to remove scattered light in earthshine data: New telescope New methods. Submitted to Astronomy & Astrophysics, 2012.

N. D. Tyson and R. R. Gal. An exposure guide for taking twilight flatfields with large format CCDs. *Astronomical Journal*, 105:1206, 1993.

F. W. Very. The earth's albedo. *Astronomische Nachrichten*, 196:269, 1913.

F. W. Very. The photographic spetrography of the earth-shine. *Astronomische Nachrichten*, 201:353, 1915.

B. A. Wielicki, T. Wong, N. Loeb, K. Minnis, P. Priestley, and R. Kandel. Changes in Earth's Albedo Measured by Satellite. *Science*, 308:825, 2005.

Y. Zhang, W. B. Rossow, A. A. Lacis, V. Oinas, and M. I. Mishchenco. Calculation of radiative fluxes from the surface top of atmosphere based on ISCCP and other global data sets. *JGRD*, 109(D19):105, 2004.